Assessment of atomistic data for predicting the phase diagram and defect thermodynamics in UO_2

Serge Maillard, David Andersson, Fabien Bruneval

Assessment of atomistic data for predicting the phase diagram and defect thermodynamics in UO_2

Serge Maillard*, David Andersson†, Michel Freyss*, Fabien Bruneval‡

September 22, 2021

This paper develops a unified presentation of the thermodynamic parameters of eleven point-defect models in UO_2 (defect formation energies and entropies); four of them are fitted to experimental data, while the remaining seven are obtained through atomistic simulations. This allows us to compare all the models on the same basis both among themselves and with a large set of experimental data of various physical quantities. Combining the assessed defect thermodynamics and the TAF-ID functions for U and U_4O_9 phases makes it possible to compute the $U-O$ phase diagram in the vicinity of stoichiometric UO_2. The defect formation energies and entropies are very different from one model to another. Concerning the ability to reproduce experimental data, the fitted models usually correctly reproduce the data sets according to which they were fitted. For one atomistic-based model, the measurements of the oxygen potential as a function of the temperature and the O/M ratio are reproduced in a satisfactory manner while the phase diagram is more approximate. No model, either fitted or atomistic-based, reproduces simultaneously the measured conductivity and the oxygen concentration as functions of the oxygen potential. The difficulties of the atomistic-based models in predicting the O/M ratio as a function of the oxygen potential are thought to partly arise from an erroneous calculation of the oxygen molecule energy derived from *ab initio* techniques and probably also from a poor evaluation of the electron-hole Gibbs energy of formation; more generally improving the technique for calculating reliable defect entropies of formation appears of great importance. The difficulty of obtaining reliable experimental data close to the stoichiometry might also contribute to the limited agreement between calculations and measurements, which is reason enough to reassess the behavior of the material in this stoichiometry region comprehensively, using all the possible characterization techniques on each material sample. In particular, since several independent studies predict an unexpected crucial role of the uranium vacancies on the evolution of O/M, experimental assessments of this feature should be sought.

*CEA, DEN, DEC, Cadarache, 13108 Saint-Paul-lez-Durance, France
†Materials Science and Technology Division, Los Alamos National Laboratory P.O. Box 1663, Los Alamos, NM 87545, USA
‡Université Paris-Saclay, CEA, Service de Recherches de Métallurgie Physique, 91191 Gif-sur-Yvette, France

Contents

List of Tables

List of Figures

1 Introduction

Providing a model of fuel materials grounded on reliable thermodynamic functions has long been undertaken, namely in view of predicting the thermal behavior of these materials during in-pile irradiation and assessing various related safety limits. For example, recent developments based on the Calphad method fitting a large thermodynamic database yielded a set of Gibbs energy functions (the TAF-ID [39]) allowing us to compute most of the important thermodynamic functions and features (melting temperature, oxygen potential, stoichiometry, etc.) for the main fuel materials such as UO_2, $(U,Pu)\,O_2$, $(U,Pu)\,C$... and the corresponding phase diagrams ($U-O, U-Pu-O, U-C-O, U-Pu-C$...) [24, 25]. In a similar way to what has been done to understand the in-pile behavior of metallic materials composing nuclear reactors, attempts have been made to describe the main features of the fuel behavior (fission gas release, swelling, restructuring) in terms of micro-structural evolution. Various kinetic models were built for this purpose, some on the grounds of thermodynamic and diffusion parameters defined at an atomic level [22, 48]. The first-generation models for defect thermodynamics, i.e. the fitted models, were obtained through fitting the defect formation Gibbs energies by comparing simulation and measurement of the stoichiometry as a function of the oxygen chemical potential [37, 41] or electric conductivity [21]. Atomistic calculation of defect formation energies/entropies progressively became possible so that these techniques produced sufficient results to support a second generation of defect thermodynamic models [3, 51, 52, 12, 14, 49], i.e. the atomistic-based models. Surprisingly, few if any attempts have been made to assess the validity of these thermodynamic parameters by simulating physical properties known to be sensitive to them and comparing the results with experiments. The purpose of this paper is to review and compare several defect models, both fitted and atomistic-based, both among themselves and with such observations. After this introduction, the second, theoretical, part, will present various thermodynamic models (all equivalent) for the defect concentrations in a unified manner. In the third part, the thermodynamic parameters of these models will be gathered and discussed. We will propose a set of conventions in which all the analyzed parameters will be expressed and compared. In the fourth part the model simulation results will be compared to corresponding experimental situations; the first generation of defect models will also be reviewed to enrich the comparison.

2 Modeling

2.1 Statistical physics modeling

The statistical physics approach presented here seems to implicitly underline several atomistic approaches such as [53, 55, 52]. The model will be presented in detail as will the thermal behavior of its thermodynamic parameters in order to clarify its relationships with atomistic simulations.

2.1.1 General equations

Following [26], we use the thermodynamic framework of Fähnle *et al.* [35, 36] for evaluating the defect concentrations. As the latter work was devoted to a compound presenting vacancies and anti-site defects, we decided to slightly adapt the model to the context of UO_2 which does not present anti-site defects, but the creation of vacancies/interstitials and the exchange of O and U atoms with the environment. We study a system comprising a UO_{2+x} solid sample at a given temperature and pressure; this system is closed so that its composition remains fixed and comprises N_O oxygen O, N_U uranium U, N_e electrons e (corresponding to the total defect charges). Its composition is noted $\mathbf{N} = (N_U, N_O, N_e)$. A perfect sample comprising N_s UO_2 patterns will thus be written $\mathbf{\Lambda} = N_s\boldsymbol{\lambda} = N_s\,(1,2,0)$, while $\mathbf{N} = N_s\boldsymbol{\lambda} + \boldsymbol{\nu}$ (with $\boldsymbol{\nu} = (\nu_U, \nu_O, \nu_e)$) represents a sample with one defect of composition $\boldsymbol{\nu}$ representing the deviation from the perfect material. For instance a double negatively charged di-vacancy $V_{UO}^{2'}$, comprising a uranium vacancy bound to an oxygen vacancy, is represented as $\boldsymbol{\nu} = (-1,-1,2)$. We also introduce ϕ_ν as the number of equivalent configurations of the defect $\boldsymbol{\nu}$ inside a given UO_2 pattern (i.e. $\phi_{-1,-1,2} = 4$ since there are 4 equivalent positions for the O vacancy for each U vacancy). For convenience we define the "null" defect to be an ordinary site, corresponding to $\boldsymbol{\nu} = \mathbf{0} = (0,0,0)$. $\mathbb{D}$ is then the total set of generalized defect types (including $\mathbf{0}$), while $\mathbb{D}^* = \mathbb{D} \setminus \{0\}$ is the set of true defect types. According to this convention we have

$$\sum_{\nu\in\mathbb{D}} N_\nu = N_0 + \sum_{\nu\in\mathbb{D}^*} N_\nu = N_s. \tag{1}$$

In a supercell approach we assume the defect concentrations are low enough so that the interactions between defects can be neglected. $G_{N_c\boldsymbol{\lambda}+\boldsymbol{\nu}}$ is the Gibbs energy of a supercell comprising N_c UO_2 patterns and one defect of type $\boldsymbol{\nu}$. In the infinite dilution limit, $N_c \to \infty$, we define $\delta g_\nu = \lim_{N_c\to\infty} \left(G_{N_c\boldsymbol{\lambda}+\boldsymbol{\nu}} - G_{N_c\boldsymbol{\lambda}}\right)$, which will be named "differential" Gibbs energy, and choose N_c large enough so that $G_{N_c\boldsymbol{\lambda}+\boldsymbol{\nu}} \sim G_{N_0\boldsymbol{\lambda}} + \delta g_\nu = N_c G_\lambda + \delta g_\nu$, $G_{\boldsymbol{\lambda}} = G_{UO_2}$ corresponding to the Gibbs energy for one UO_2 pattern of perfect crystal. The whole UO_2 system comprising N_ν defects of each type $\boldsymbol{\nu}$ is made up of all the supercells of size N_c, each comprising one defect of type $\boldsymbol{\nu}$. Its composition, which also expresses the U, O and e conservation laws, can be written:

$$\mathbf{N} = \sum_{\nu\in\mathbb{D}} N_\nu \left(N_c\boldsymbol{\lambda} + \boldsymbol{\nu}\right) = N_s\boldsymbol{\lambda} + \sum_\nu N_\nu\boldsymbol{\nu} = N_s\left(\boldsymbol{\lambda} + \sum_\nu C_\nu\boldsymbol{\nu}\right) \tag{2}$$

$N_s = N_c\sum N_\nu$ is thus the total number of UO_2 patterns, and $C_\nu = \frac{N_\nu}{N_s}$ is the site fraction of defect $\boldsymbol{\nu}$, which we also call "concentration" in the following. The Gibbs energy of the whole system is the sum of the contributions of the various defects, plus the contribution of the configuration entropy:

$$G = \sum_\nu N_\nu G_{N_c\boldsymbol{\lambda}+\boldsymbol{\nu}} - T.S_{conf} \sim \sum_\nu N_\nu\left(N_c G_\lambda + \delta g_\nu\right) - T.S_{conf}$$

with

$$G_{N_c\boldsymbol{\lambda}} = N_c G_\lambda$$

As the concentrations are low, S_{conf} can be written and approximated this way:

$$\begin{aligned} S_{conf} &\sim k_B \ln\left(\prod_\nu \phi_\nu^{N_\nu}\frac{\left(\sum_\nu N_\nu\right)!}{\prod_\nu N_\nu!}\right) \sim -k_B\sum_\nu N_\nu \ln\left(\frac{N_\nu}{\phi_\nu}\right) \\ &\sim -N_s\, k_B\sum_\nu C_\nu \ln\left(\frac{C_\nu}{\phi_\nu}\right) \end{aligned}$$

The Gibbs energy is finally written:

$$G \sim N_s g$$

with

$$g = G_{\boldsymbol{\lambda}} + \sum_\nu C_\nu\delta g_\nu + k_B T C_\nu \ln\left(\frac{C_\nu}{\phi_\nu}\right) \tag{3}$$

where g is the Gibbs energy per UO_2 pattern of the material with defects.

To obtain the equilibrium concentrations C_ν we have to minimize at given T and P and composition $(N_U, N_O, N_e = 0)$ the Gibbs energy of the whole system under the corresponding constraints (2) and (1):

$$\min_{N_s, N_{\nu,\nu\in\mathbb{D}}} G\left(N_s, N_{\nu,\nu\in\mathbb{D}}, T, P\right)$$

with

$$\begin{aligned} N_s\boldsymbol{\lambda} + \sum_\nu N_\nu\boldsymbol{\nu} - \mathbf{N} &= 0 \\ \sum_\nu N_\nu - N_s &= 0 \end{aligned}$$

Introducing the Lagrange multipliers $\boldsymbol{\mu}$ and χ, the Lagrangian J of this optimization problem (P and T being fixed) is written:

$$J\left(N_s, N_{\nu,\nu\in\mathbb{D}}, \boldsymbol{\mu}, \chi\right) = G\left(N_s, N_{\nu,\nu\in\mathbb{D}}, T, P\right) - \boldsymbol{\mu}.\left(N_s\boldsymbol{\lambda} + \sum_\nu N_\nu\boldsymbol{\nu} - \mathbf{N}\right) - \chi\left(\sum_\nu N_\nu - N_s\right)$$

Introducing the deviation from perfect composition $\boldsymbol{\Delta\lambda}$ as a function of N_s according to

$$\frac{\mathbf{N}}{N_s} = \boldsymbol{\lambda} + \boldsymbol{\Delta\lambda}, \tag{4}$$

we can write the equilibrium concentrations given through the following optimality conditions:

$$\partial_{N_s} J = 0 = g - \sum_\nu C_\nu \partial_{C_\nu} g - \boldsymbol{\mu}.\boldsymbol{\lambda} + \chi \tag{5a}$$

$$\partial_{N_\nu} J = 0 = \partial_{C_\nu} g - \boldsymbol{\mu}.\boldsymbol{\nu} - \chi \tag{5b}$$

$$\frac{\partial_{\boldsymbol{\mu}} J}{N_s} = 0 = \sum_\nu C_\nu \boldsymbol{\nu} - \boldsymbol{\Delta\lambda} \tag{5c}$$

$$\frac{\partial_{\boldsymbol{\mu}} J}{N_s} = 0 = \sum_\nu C_\nu - 1 \tag{5d}$$

Evaluating $\partial_{C_\nu} g$ from Eq. (3), χ to $k_B T\left(\ln\left(C_0\right)+1\right)$ from Eq. (5b) applied to the case $\nu = \mathbf{0}$, and combining the above equations yields:

$$G_\lambda - \boldsymbol{\mu}.\boldsymbol{\lambda} + k_B T \ln\left(C_0\right) = 0 \tag{6a}$$

$$\delta g_\nu - \boldsymbol{\mu}.\boldsymbol{\nu} \; + k_B T \ln\left(\frac{C_\nu}{\phi_\nu C_0}\right) = 0 \tag{6b}$$

$$\boldsymbol{\Delta\lambda} - \sum_{\nu \in \mathbb{D}^*} C_\nu \boldsymbol{\nu} = 0 \tag{6c}$$

$$C_0 + \sum_{\nu \in \mathbb{D}^*} C_\nu - 1 = 0 \tag{6d}$$

Eq. (6c) being equivalent to:

$$\sum_\nu \nu_U C_\nu = \Delta\lambda_U \tag{6e}$$

$$\sum_\nu \nu_O C_\nu = \Delta\lambda_O \tag{6f}$$

$$\sum_\nu \nu_e C_\nu = 0 \tag{6g}$$

These equations are related to x, the deviation from stoichiometry, according to the relation:

$$x = \frac{\Delta\lambda_O - 2\Delta\lambda_U}{1 + \Delta\lambda_U} \sim \Delta\lambda_O - 2\Delta\lambda_U$$

Let us notice that in Eq. (6c), the sum can be calculated indifferently on the set $\mathbb{D}$ or $\mathbb{D}^*$since $C_{(0,0,0)} = C_0$ has no contribution anyway.

Equations (6a) to (6d) define the canonical ensemble of the material (in which N_U, N_O and N_e are fixed). Solving these equations, we obtain all the concentrations C_ν, the number N_s (via Eq. (4)) of sites of the material (equivalent to its volume if thermal expansion is neglected) and the Lagrange multipliers $\boldsymbol{\mu}$ of U, O and e, as functions of the composition (N_U, N_O) (or (λ_U, λ_O)). At equilibrium, $J = \boldsymbol{\mu}.\boldsymbol{N}$ and $\boldsymbol{\mu}$ represents the chemical potentials of U, O and e. The same set of equations also holds for the grand canonical ensemble (in which the chemical potentials are fixed) that allows us to describe the equilibrium in which the exchange of U and O with the environment occurs (even of e, if the sample is connected to an electric device, which is outside the scope of of this article). Mixing constraints on the quantities and on the chemical potentials allows us to solve problems closer to real experimental conditions, e.g. where both μ_O and λ_U are fixed (uranium vaporization is supposed negligible), in addition to N_e which is fixed to 0 as we know. In other experiments where the phase diagram is studied, both chemical potentials are fixed because of the simultaneous existence of two solids at a given temperature, such as UO_2 and metallic U or U_4O_9 as will be seen below.

While the various absolute energetic quantities such as G_λ, δg_ν or $\boldsymbol{\mu}$ have no physical meaning, only their differences appear in the above equations ($\delta g_\nu - \mu.\nu$, $G_\lambda - \boldsymbol{\lambda}.\boldsymbol{\mu}$). For example, $\delta g_\nu - \boldsymbol{\mu}.\boldsymbol{\nu}$ is the defect, temperature-dependent, formation Gibbs energy as defined in [53, 52]. Nevertheless, these differences depend on the chemical potential vector $\boldsymbol{\mu}$ which is a characteristic of the material's environment (notably the oxygen pressure), so that a conventional reference state in terms of chemical potentials is necessary to tabulate these parameters in a way they can be understood unambiguously (and used). For each temperature, the chosen thermodynamic reference is (when relevant) the standard state at this temperature $\boldsymbol{\mu}^0\left(T\right) = \boldsymbol{\mu}\left(P^0, T\right)$, and we define the corresponding relative chemical potentials as:

$$\Delta\boldsymbol{\mu} = \boldsymbol{\mu} - \boldsymbol{\mu}^{\mathbf{0}}\left(T\right)$$

Noticing that $\delta g_\nu - \boldsymbol{\nu}.\boldsymbol{\mu} = \delta g_\nu - \boldsymbol{\nu}.\boldsymbol{\mu^0} - \boldsymbol{\nu}.\Delta\boldsymbol{\mu}$, we now unambiguously define the standard Gibbs formation energy of defect $\boldsymbol{\nu}$ as a function of the temperature:

$$g_\nu(T) = \delta g_\nu(T) - \boldsymbol{\nu}.\boldsymbol{\mu^0}(T) \tag{7}$$

A more rigorous notation such as Δg^0_ν (instead of g_ν) would clearly underline that a formation energy in this sense is actually a *difference* of standard energies, but for simplicity we will keep the above notation $g_\nu(T)$ or even g_ν.
For example, the Gibbs formation energy of the oxygen interstitial $\boldsymbol{\nu} = O_i^{2'} = (0,1,2)$ is written:

$$g_{O_i^{2'}}(T) = \delta g_{O_i^{2'}}(T) - \mu^0_O(T) - 2\mu^0_e(T) \tag{8}$$

and, provided the relative chemical potentials $\Delta\mu_j$ are known (e.g. through the conservation equations) and $k_B T \ll g_{O_i^{2'}}$, the concentration is approximately given by:

$$C_{O_i^{2'}} \sim \exp\left(-\frac{g_{O_i^{2'}}(T) - \Delta\mu_O - 2\Delta\mu_e}{k_B T}\right)$$

The same notation idea holds if we transform Eq. (6a) to $G_\lambda(T) - \boldsymbol{\nu}.\boldsymbol{\mu^0}(T) - \boldsymbol{\nu}.\boldsymbol{\Delta\mu}$, which similarly defines the ordinary site standard Gibbs formation energy as $\Delta g^0_{UO_2}(T) = G_\lambda(T) - \boldsymbol{\nu}.\boldsymbol{\mu^0}(T)$ which could also be noted as $\Delta g^0_{UO_2} = g_0$ in the same line as g_ν (as in Eq. (15a)).

2.1.2 Reference states for U, O and e

The reference states always correspond to the atmospheric pressure $P^0 = 1\,\text{bar}$. For U and O, we apply the usual convention:

- One atom of metallic uranium U at T and P^0 for the U reference
- "Half a molecule" of gaseous oxygen O_2 at T and P^0. In the relevant pressure and temperature range, the expression of the relative chemical potential of a O_2 molecule considered as a perfect gas at pressure P_{O_2} applies:

$$\Delta\mu_O = \frac{1}{2}k_B T \ln(p) \text{ with } p = \frac{P_{O_2}}{P^0} \tag{9}$$

The standard chemical potentials for U and O, $\mu^0_U(T)$ and $\mu^0_O(T)$, are taken from the TAF-ID while the values at 0 K are from [16]; all this data is reported in the appendix, Table 5.
The commonly claimed reference state for the electrons is the Fermi level in the perfect material (or $\mu_e^{VBM} = 0$, noted as "VBM"), which is not a standard thermodynamic convention but has a physical significance when there is exchange of electrons with the environment. We will see below that a more practical convention is to define the reference state of the electrons so that the hole formation Gibbs energy at the current temperature T is zero, i. e. $g_h(T) = 0$, noted as "h".

2.1.3 Temperature dependence of the formation Gibbs energies

An atomistic calculation produces results at a given reference temperature T_r. The temperature dependence of these quantities is written:

$$h_\nu(T) = h_\nu(T_r) + \left[\delta h_\nu - \boldsymbol{\nu}.\boldsymbol{h^0}\right]_{T_r}^{T} = h_\nu(T_r) + \int_{T_r}^{T} c_\nu(\Theta)\,d\Theta \tag{10a}$$

$$s_\nu(T) = s_\nu(T_r) + \left[\delta s_\nu - \boldsymbol{\nu}.s^0\right]_{T_r}^{T} = s_\nu(T_r) + \int_{T_r}^{T} \frac{c_\nu(\Theta)}{\Theta}d\Theta \tag{10b}$$

The last member of each line allows us to define various heat capacities. $c_\nu = \delta c_\nu - \boldsymbol{\nu}.\boldsymbol{c^0}$ is thus the standard formation heat capacity of the defect ν, $\boldsymbol{c^0}$ being the vector of the thermal capacities of the components U, O, e in the reference state. δc_ν represents the difference in thermal capacity at constant pressure and is defined in the same way as δg_ν or δh_ν as the difference of c between a faulted supercell and a perfect one. The notation $[f]_{T_r}^{T}$ stands for the variation of any function f between the temperatures T_r and T. As will be seen later, all calculated defect Gibbs energies δg_ν correctly accommodate a quasi constant heat capacity

j	$h_j^0(0\,\mathrm{K})$ (eV)	$h_j^0(298\,\mathrm{K})$ (eV)	$h_j^0(T^r)$ (eV)	$s_j^0(T^r)$ (k_B)	c_j^0 (k_B)
U	−0.066	0	0.223	10.550	5.822
O	−0.045	0	0.098	14.401	2.200
UO_2	−11.362	−11.241	−10.776	19.172	11.053

Table 1: Thermodynamic parameters for the components and UO_2 at $T_r = 900\,\mathrm{K}$ obtained from CODATA (at 0 K) and by fitting of the TAF-ID data (Table 5) on the range 650-2700 K

c_ν on a certain temperature range $[T_m, T_M]$ (typically $[400\,\mathrm{K}, 1900\,\mathrm{K}]$). This means the tables concerning energies, entropies or Gibbs energies of [14, 12, 49] can easily be summarized in the following equation:

$$\delta g_\nu \sim \delta h_\nu\left(T_r\right) - T\left(\delta s_\nu\left(T_r\right) + \delta c_\nu \ln\left(\frac{T}{T_r}\right)\right) \tag{11}$$

This will be used to propose a practical and general framework for the various atomistic evaluations of the defect thermodynamic parameters. In this case, the following thermodynamic information has to be provided for each defect:

- T_m, T_M, T_r: the minimum and maximum temperature limits of the model, and the reference temperature for the starting point of the interpolation model (11)
- $h_\nu\left(T_r\right) = \delta h_\nu\left(0\right) - \boldsymbol{\nu}.\boldsymbol{h}^0\left(0\right) + \left[\delta h_\nu\right]_0^{T_r}$: the defect formation enthalpy (or energy considering the very low pressure) at T_r (usually combining results of *ab initio* and empirical potential techniques)
- $\left[\delta s_\nu\right]_0^{T_r} = \delta s_\nu\left(T_r\right)$: the corresponding entropy term (which is zero at 0 K)
- δc_ν: the differential heat capacity of the defect (supposed to be constant in the range $[T_m, T_M]$).

To simplify the comparison of different *ab initio* approaches, it is also useful to provide the formation enthalpy at 0 K as well, $h_\nu\left(0\right) = \delta h_\nu\left(0\right) - \boldsymbol{\nu}.\boldsymbol{h}^0\left(0\right)$.

We additionally consider that the Gibbs energy of the components (U, O, e) also fit to an equation of type (11), with a constant thermal capacity on the temperature interval $[T_m, T_M]$, as defined in Table 1. The equations (10a)-(10b) can thus be rewritten:

$$h_\nu\left(T\right) = \left(\delta h_\nu\left(0\right) - \boldsymbol{\nu}.\boldsymbol{h}^0\left(0\right)\right) + \left(\left[\delta h_\nu\right]_0^{T_r} + \delta c_\nu\left(T - T_r\right)\right) - \boldsymbol{\nu}.\left(\left[\boldsymbol{h}^0\right]_0^{T_r} + \boldsymbol{c}^0\left(T - T_r\right)\right) \tag{12a}$$

$$s_\nu\left(T\right) = 0 + \left(\left[\delta s_\nu\right]_0^{T_r} + \delta c_\nu \ln\left(\frac{T}{T_r}\right)\right) - \boldsymbol{\nu}.\left(\left[\boldsymbol{s}^0\right]_0^{T_r} + \boldsymbol{c}^0 \ln\left(\frac{T}{T_r}\right)\right) \tag{12b}$$

or equivalently

$$h_\nu\left(T\right) = h_\nu\left(T_r\right) + c_\nu\left(T - T_r\right) \tag{13a}$$

$$s_\nu\left(T\right) = s_\nu\left(T_r\right) + c_\nu \ln\left(\frac{T}{T_r}\right) \tag{13b}$$

On the one hand, presenting the atomistic results according to the first set of equations (12a)-(12b) for δg_ν (i.e. [14]) is particularly interesting since the part of the atomistic results in the formation quantities is clearly identified and separated from the part related to the component thermodynamics. The first term is usually calculated with *ab initio* techniques, while the second is calculated with empirical potential techniques, and the third is taken from thermodynamic databases. On the other hand, although the second presentation (Eqs. (13a)-(13b), i.e. [3]) is simpler, giving directly g_ν, it does not highlight this distinction easily.

For better clarification, a short explanation on h_e^0 and s_e^0 is necessary, which will be illustrated using the case of the oxygen interstitial formation enthalpy. This quantity can be evaluated through the following equation:

$$h_{O_i''}\left(T\right) = \left(\delta h_{O_i''}\left(0\right) - h_O^0\left(0\right) - 2h_e^0\left(0\right)\right) + \left[\delta h_{O_i''}\right]_0^T - \left[h_O^0\right]_0^T - 2\left[h_e^0\right]_0^T$$

The first three terms should be evaluated through *ab initio* calculations while the last two should be extracted from thermodynamic databases. The reference term for O is the standard thermodynamic convention, so that $\Delta\mu_O$, equal to $k\,T \ln\left(P_{O_2}/P^0\right)$, is a measurable quantity possibly fixed by the environment.

$\left[h_O^0\right]_0^T$ can be extracted from Table 1 or equivalently from the TAF-ID. For e there is no equivalent standard convention, but $h_e^0(T)$ is commonly chosen as the Valence Band Maximum (VBM). But since $\Delta\mu_e$ is not measured nor fixed nor influencing the final solution, there is no definitive reason to chose a particular reference for this quantity. However, fixing $g_h(T) = 0$ appears to be a clear and simple convention, which additionally corresponds to impose

$$\mu_e^0(T) = -\delta g_{h^\circ}(T) \tag{14}$$

according to Eq. (6b), for an evaluation of $\delta g_{h^\circ}(T)$ in a given reference system. As the actual value of $\mu_e^0(T)$ has no impact on the final results, no data are displayed for this quantity in Table 1.

2.1.4 Configuration entropies

The configuration numbers of the main defects are presented Table 2. They are evaluated as follows, considering the components of the composite defects are generally in first neighbor positions:

- There is only one uranium and one interstitial site per UO_2 pattern, yielding one configuration for h°, $e^{'}$, $V_U^{4'}$, $O_i^{2'}$.
- There are two oxygen sites, thus 2 configurations for $V_O^{2\circ}$.
- Supposing the vacancies comprising the oxygen di-vacancy cluster are neighbors on the oxygen cubic lattice, each O vacancy has thus 6 neighbors, yielding 3 configurations to avoid double counting for each site of the cell, the total number for the two sites being 6 for $V_{O_2}^{2\circ} = Z^{2\circ}$.
- Each di-interstitial cluster $W^{'} = O_{i_2}^{'}$ (which is actually a triangle of 3 oxygen atoms) has 8 configurations, corresponding to the 8 positions of the center of the triangle (see Figure 1 of [4]), each one corresponding to one orientation from the center to one corner of the large cube of the figure.
- The quad-interstitial $Q^{3'} = O_{i_4}^{3'}$ has 12 configurations, based on the analysis of Figure 4 of [4]. The first di-interstitial has 8 configurations. For each of them, the second one can be set on one of the 3 edges of the cube starting at the first one. The result should be divided by two because of double counting.
- The di-vacancy $V_{UO}^{2\circ}$ has 8 configurations corresponding to the positions of the oxygen vacancies at the corners of the cube whose center is the uranium atom.
- In the most stable bound Schottky defect the two oxygen vacancies are next neighbor on the same edge of a cube, the uranium vacancy staying at the center, thus yielding 12 configurations for V_{UO_2}.

2.1.5 Generic equations

With these conventions, eqs. (6a) to (6d) can be rewritten:

$$g_0 - (\Delta\mu_U + 2\Delta\mu_O) + k_B T \ln(C_0) = 0 \quad \text{with } g_0 = \Delta g^0_{UO_2} \text{(formation Gibbs energy of } UO_2) \tag{15a}$$

$$g_\nu - \boldsymbol{\nu.\Delta\mu} + k_B T \ln\left(\frac{C_\nu}{\phi_\nu C_0}\right) = 0 \tag{15b}$$

$$\sum_{\nu\in\mathbb{D}^*} \nu_U C_\nu = \Delta\lambda_U = C_U - 1 \tag{15c}$$

$$\sum_{\nu\in\mathbb{D}^*} \nu_O C_\nu = \Delta\lambda_O = C_O - 2 \tag{15d}$$

$$C_{dop} + \sum_{\nu\in\mathbb{D}^*} \nu_e C_\nu = 0 \tag{15e}$$

$$C_0 = 1 - \sum_{\nu\in\mathbb{D}^*} C_\nu \tag{15f}$$

$$\Delta\mu_O = \frac{1}{2} k_B T \ln(p) \text{ with } p = \frac{P_{O_2}}{P^0} \tag{15g}$$

In order to account for impurities (or dopant) in the material, we have added a term C_{dop} to the electroneutrality equation (15e), corresponding to the total electrons concentration born by impurities (e.g. the contribution to C_{dop} of pentavalent ions is the opposite of their concentration).

This set of equations can also be expressed when $(UO_2\downarrow, O_2\uparrow)$ are the thermodynamic references for O and U, instead of $(U\downarrow, O_2\uparrow)$. Considering that the chemical potential of UO_2 verifies

$$\mu_{UO_2} = \mu_U + 2\mu_O \text{ and } \Delta g^0_{UO_2} + \Delta\mu_{UO_2} = \Delta\mu_U + 2\Delta\mu_O,$$

we obtain the following set of equations that can formally be reinterpreted in the defect base ν^{UO_2} defined as follows:

$$g_{\nu^{UO_2}} - \boldsymbol{\nu^{UO_2}}.\boldsymbol{\Delta\mu^{UO_2}} + k_B T \ln\left(\frac{C_{\nu^{UO_2}}}{\phi_{\nu^{UO_2}} C_0}\right) = 0 \tag{16a}$$

$$\boldsymbol{\nu^{UO_2}} = (\nu_U, \nu_O - 2\nu_U, \nu_e) \tag{16b}$$

$$\boldsymbol{\Delta\mu^{UO_2}} = (\Delta\mu_{UO_2}, \Delta\mu_O, \Delta\mu_e) \tag{16c}$$

$$g_{\nu^{UO_2}} = g_\nu - \nu_U \Delta g^0_{UO_2} \tag{16d}$$

This is also the convention developed by Bruneval et al. [12], Soulié et al. [49]. If we additionally consider Eq. (15a), we obtain $\Delta\mu_{UO_2} = k_B T \ln(C_0)$, and Eq. (16a) is rewritten:

$$\left(g_\nu - \nu_U \Delta g^0_{UO_2}\right) - \left(\nu_O - 2\nu_U\right)\Delta\mu_O - \nu_e \Delta\mu_e + k_B T \ln\left(\frac{C_\nu}{\phi_\nu C_0^{1+\nu_U}}\right) = 0 \tag{17}$$

If the electron reference is VBM, the first term in bracket in both expressions

$$g_\nu^{UO_2,VBM} = g_\nu - \nu_U \Delta g^0_{UO_2}$$

is the formation Gibbs energy reported by these authors as calculated in the $(UO_2\downarrow, O_2\uparrow, VBM)$ reference (i.e. in [12, Eq. (8)] or [49, Eq. (1)]). This equation, slightly modified to account for the additional change in the electron chemical potential reference, is used here for the translation between the $(UO_2\downarrow, O_2\uparrow, VBM)$, $(UO_2\downarrow, O_2\uparrow, h)$ and $(U\downarrow, O_2\uparrow, h)$ references, corresponding to the Gibbs energies $g_\nu^{UO_2,VBM}$, $g_\nu^* = g_\nu^{UO_2,h}$ and g_ν=$g_\nu^{U,h}$ respectively:

$$\begin{aligned} g_\nu^* = g_\nu^{UO_2,h} &= g_\nu^{UO_2,VBM} + \nu_e g_h^{UO_2,VBM} \\ g_\nu = g_\nu^{U,h} &= g_\nu^{UO_2,h} + \nu_U \Delta g^0_{UO_2} \end{aligned}$$

For example, in the case of the uranium vacancy we have

$$g_{V_U^{4'}} = g_{V_U^{4'}}^{UO_2,VBM} - \Delta g^0_{UO_2} + 4 g_h^{UO_2,VBM} \tag{18}$$

The energy at 0 K given by Bruneval $e_{V_U^{4'}}^{UO_2,VBM} = 0.68\,\text{eV}$ corresponds to $e_{V_U^{4'}} = 11.50\,\text{eV}$ in the $(U\downarrow, O_2\uparrow, h)$ reference and Table 4, considering $\Delta e^f_{UO_2} = -11.206\,\text{eV}$ and $e_h^{UO_2,VBM} = -0.096\,\text{eV}$ (when the reference for the electron chemical potential is the Valence Band Maximum). Let us remark that applying Eq. (17) to the case of $V_U^{4'}$, considering $C_0 \sim 1$ yields an equation formally equivalent to that of an oxygen di-interstitial $(O_i)_2^{4'}$.

2.1.6 Model illustration

Let us now illustrate the model using a simplified case and considering the defect concentrations are low ($C_\nu \ll 1$ for $\nu \neq \mathbf{0}$, and C_0~1). At thermodynamic equilibrium, the concentrations verify the following equations (the charges are omitted unless necessary):

$$\Delta g^0_{UO_2}(T) - (\Delta\mu_U + 2\Delta\mu_O) - k_B T\left(C_{V_O} + C_Z + C_h + C_{O_i} + C_W + C_{V_U} + C_e\right) = 0 \tag{19a}$$

$$g_{V_O} + \Delta\mu_O + 2\Delta\mu_e + k_B T \ln\left(\frac{C_{V_O}}{2}\right) = 0 \tag{19b}$$

$$g_Z + 2\Delta\mu_O + 2\Delta\mu_e + k_B T \ln\left(\frac{C_Z}{6}\right) = 0 \tag{19c}$$

$$g_{O_i} - \Delta\mu_O - 2\Delta\mu_e + k_B T \ln(C_{O_i}) = 0 \tag{19d}$$

$$g_W - 2\Delta\mu_O - \Delta\mu_e + k_B T \ln\left(\frac{C_W}{8}\right) = 0 \tag{19e}$$

$$g_{V_U} + \Delta\mu_U - 4\Delta\mu_e + k_B T \ln(C_{V_U}) = 0 \tag{19f}$$

$$g_e - \Delta\mu_e + k_B T \ln(C_e) = 0 \tag{19g}$$

$$g_h + \Delta\mu_e + k_B T \ln(C_h) = 0 \tag{19h}$$

$$2C_{V_O} + 2C_Z + C_h - \left(2C_{O_i} + C_W + 4C_{V_U} + C_e + C_{dop}\right) = 0 \tag{19i}$$

$$\Delta\mu_O = \frac{1}{2} k_B T \ln(p) \tag{19j}$$

$\Delta g^0_{UO_2}(T)$ is the standard formation Gibbs energy of UO_2.

2.2 Formalism of equilibrium reactions

Another way to represent the thermodynamic equilibrium of defects can be obtained by eliminating the electron chemical potential (using (19h) for instance) in the various equations of type (6b). The result is a set of mass action law equations that can be solved if the remaining chemical potentials are known. For example, the set of equations (19a) to (19j) is transformed to the following reaction and balance equations:

$$2h^{\circ} \rightleftarrows V_O^{2\circ}(\text{2 configurations}) + \frac{1}{2}O_2 \qquad \frac{C_{V_O}\sqrt{p}}{2C_h^2} = \exp\left(-\frac{g_{V_O} - 2g_h}{k_B T}\right) \tag{20a}$$

$$2h^{\circ} \rightleftarrows Z^{2\circ}(\text{6 configurations}) + O_2 \qquad \frac{C_Z p}{6c_h} = \exp\left(-\frac{g_Z - 2g_h}{k_B T}\right) \tag{20b}$$

$$\frac{1}{2}O_2 \rightleftarrows O_i^{2'} + 2h^{\circ} \qquad \frac{C_{O_i}C_h^2}{\sqrt{p}} = \exp\left(-\frac{g_{O_i} + 2g_h}{k_B T}\right) \tag{20c}$$

$$O_2 \rightleftarrows W^{'}(\text{8 configurations}) + h^{\circ} \qquad \frac{C_W C_h}{8p} = \exp\left(-\frac{g_W + g_h}{k_B T}\right) \tag{20d}$$

$$O_2 \rightleftarrows V_U^{4'} + 4h^{\circ} + UO_2 \qquad \frac{C_{V_U}C_h^4}{p} = \exp\left(-\frac{g_{V_U} + \Delta g^0_{UO_2} + 4g_h}{k_B T}\right) \tag{20e}$$

$$\varnothing \rightleftarrows e^{'} + h^{\circ} \qquad C_h C_e = \exp\left(-\frac{g_e + g_h}{k_B T}\right) \tag{20f}$$

$$0 = 2C_{V_O} + 2C_Z + C_h - \left(2C_{O_i} + C_W + 4C_{V_U} + C_e + C_{dop}\right) \tag{20g}$$

This presentation is generally adopted in experimental approaches such as those of [37, 38, 41, 42, 21]. Atomistic parameters of [18, 3] are also reported this way. This presentation is clearly equivalent to that used in the previous paragraph. It should nevertheless be noticed that several approaches of the configuration entropies exist. In [37], there are no combinatory numbers in the Mass Action Law expressions, which leads to modify the reaction entropy of the corresponding quantity to remain coherent with our approach; for instance the experimental formation entropy of $V_O^{2\circ}$ needs to be increased by an amount of $\ln(1/2)\,k_B$. In other publications [42, 21], the Mass Actions Law explicitly include the sites of the perfect lattice that contribute to the defect reaction, for example the formation reaction for $V_{O_2}^{2\circ}$ would be written

$$2U_U^{\circ} + 2O_O^{\times} \rightleftarrows 2U_U^{\times} + V_{O_2}^{2\circ} + O_2$$

and the corresponding Mass Action Law:

$$\frac{\left|U_U^{\times}\right|^2 \left|V_{O_2}^{2\circ}\right| p}{\left|U_U^{\circ}\right|^2 \left|O_O^{\times}\right|^2} = \exp\left(-\frac{g_\nu^{eq}}{k_B T}\right)$$

In this case, as $\left|O_O^{\times}\right| = 2$, the experimental formation entropy is increased by an amount of $\ln\left(\frac{2^2}{6}\right)k_B$. The values of Table 4 take these corrections into account.

Equations (19b) to (19j) have shown that on the one hand, the formation Gibbs energies g_ν have a unique physical meaning once the standard state is chosen for electrons, uranium and oxygen. On the other hand, we always observe (Eqs. (20a) to (20f)) the quantity

$$g_\nu + \nu_e g_h = \delta g_\nu + \nu_e \delta g_h - \nu_U \mu_U^0 - \nu_O \mu_O^0$$

in the formula for the reaction Gibbs energy, which furthermore is independent of the electron reference (as stated in Section 2.1.3, g_ν and g_h change in a way that their combination does not change when the reference for e changes). This confirms that the relevant quantity is actually $g_\nu + \nu_e g_h$ (identically zero for $\nu = h$), which justifies the convention $g_h = 0$ for describing the thermodynamic reference for the electrons. Let us notice that this convention is close to the more usual convention of taking the electrons at the VBM, as shown by atomistic calculations of the hole formation energy at 0 K, which is around 0.096 eV according to [12], and the hole entropy, which is small compared to other defects. Finally, as exemplified by Eq. (20e),

the equilibria described by Eqs. (20a) to (20f) are related to the reference $(UO_2\downarrow, O_2\uparrow, h)$; in such a case, the defect formation Gibbs energies ($g^*_\nu = g_\nu - \nu_U \Delta g^0_{UO_2} + \nu_e g_h$) are strictly equal to the reaction Gibbs energy defined in these equilibria. More generally equations such as (15b) for a defect $\nu = (\nu_U, \nu_O, \nu_e)$ correspond to an equilibrium of the following type with its Mass Action Law:

$$\begin{cases} \frac{\nu_O - 2\nu_U}{2} O_2\uparrow & \rightleftarrows (\nu_U, \nu_O, \nu_e) + \nu_e h^\circ - \nu_U UO_2\downarrow \\ \frac{C_{\nu_U,\nu_O,\nu_e} \times C_h^{\nu_e}}{\gamma_{\nu_U,\nu_O,\nu_e} \times p^{\frac{\nu_O-2\nu_U}{2}}} & = \exp\left(-\frac{g_{\nu_U,\nu_O,\nu_e} - \nu_U \Delta g^0_{UO_2} + \nu_e g_h}{k_B T}\right) = \exp\left(-\frac{g^*_{\nu_U,\nu_O,\nu_e}}{k_B T}\right) \end{cases} \tag{21}$$

2.3 Calphad method

In this section we show the Calphad modeling of UO_2 [24, 25] can be interpreted in the framework developed in Section 2.1. In the Calphad formalism, the Gibbs energy of the system is generally written $G = G_{ref} + G_{conf} + G_{exc}$ (Eqs. (4) and (5) of [24]):

$$G_{ref} = \sum_{i,j,k} y^1_i y^2_j y^3_k G_{i,j,k} \tag{22}$$

$$\begin{aligned} G^{exc} =& y^1_{U^{3+}} \times y^1_{U^{4+}} \times y^2_{O^{2-}} \times y^3_{Va} \left[L^a_{(U^{3+},U^{4+})(O^{2-})(Va)} + L^b_{(U^{3+},U^{4+})(O^{2-})(Va)} \left(y^1_{U^{3+}} - y^1_{U^{4+}} \right) \right] \\ &+ y^1_{U^{4+}} \times y^1_{U^{5+}} \times y^2_{O^{2-}} \times y^3_{O^{2-}} L_{(U^{4+},U^{5+})(O^{2-})(O^{2-})} \end{aligned} \tag{23}$$

$$G_{conf} = k_B T \left(\sum_i y^1_i \ln\left(y^1_i\right) + 2 \sum_j y^2_j \ln\left(y^2_j\right) + \sum_k y^3_k \ln\left(y^3_k\right) \right) \tag{24}$$

where y^s_m is the site fraction of the component m in the sub-lattice s so that $\sum_m y^s_m = 1$, $G_{i,j,k}$ is the Gibbs energy of the i,j,k end-member the composition of which is $\left(y^1_i, y^2_j, y^3_k\right) = (1,1,1)$, and G^{exc} is the excess Gibbs energy [50]. The sub-lattices 1, 2, 3 correspond to U atoms, O atoms and interstitial sites respectively. Using the same notations as in [25], we detail the variables: for the U sub-lattice, the variables y^1_i correspond to the fractions of the different oxidation states of the U atom ($i = U^{3+}, U^{4+}, U^{5+}$): $y^1_{U^{4+}} = \left|U^{4+}\right| = \left|U^\times_U\right|$, $y^1_{U^{5+}} = \left|U^{5+}\right| = \left|U^\circ_U\right| = C_{h^\circ}$ and $y^1_{U^{3+}} = \left|U^{3+}\right| = \left|U^{'}_U\right| = C_{e'}$. For the second and third sub-lattice variables, we have ($j = O^{2-}, Va$) $y^2_{O^{2-}} = \left|O^\times_O\right|$, $y^2_{Va} = \left|V^{\circ\circ}_O\right| = \frac{1}{2} C_{V^{\circ\circ}_O}$ and ($k = O^{2-}, Va$) $y^3_{Va} = \left|V^\times_i\right|$, $y^3_{O^{2-}} = \left|O^{''}_i\right| = C_{O^{''}_i}$. By expressing G as a function of the defect concentrations C_ν and deriving the differential of this function, we can identify δg_ν and μ_i based on the thermodynamic functions of Appendix A of [25]:

$$\begin{aligned} G &= g_{UO_2} + C_{O_i} \delta g_{O_i} + C_{V_O} \delta g_{V_O} + C_e \delta g_e + C_h \delta g_h \\ g_{UO_2} &= G^{MOX}_{(U^{4+})(O^{2-})(Va)} \\ \delta g_{O_i} &= G^{MOX}_{(U^{4+})(O^{2-})(O^{2-})} - G^{MOX}_{(U^{4+})(O^{2-})(Va)} \\ \delta g_{V_O} &= \frac{1}{2}\left(G^{MOX}_{(U^{4+})(Va)(Va)} - G^{MOX}_{(U^{4+})(O^{2-})(Va)} \right) \\ \delta g_h &= G^{MOX}_{(U^{5+})(O^{2-})(Va)} - G^{MOX}_{(U^{4+})(O^{2-})(Va)} \\ \delta g_e &= L^a_{(U^{3+},U^{4+})(O^{2-})(Va)} - L^b_{(U^{3+},U^{4+})(O^{2-})(Va)} + G^{MOX}_{(U^{3+})(O^{2-})(Va)} - G^{MOX}_{(U^{4+})(O^{2-})(Va)} \end{aligned}$$

$$\begin{aligned} \mu^0_U &= G_{U\alpha,metal} \\ \mu^0_O &= G_{O,gas} \\ \mu^0_e &= -\left(G^{MOX}_{(U^{5+})(O^{2-})(Va)} - G^{MOX}_{(U^{4+})(O^{2-})(Va)} \right) \end{aligned}$$

The last three equations determine the uranium, oxygen and electron standard chemical potentials. $G_{O,gas}$ and $G_{U\alpha,metal}$ are the Gibbs energy for half a molecule of gaseous O_2 and one atom of U in the metallic α phase as described in the TAF-ID thermodynamic database. The electron value was arbitrarily chosen so that the hole formation Gibbs energy $g_h = \delta g_h + \mu^0_e$ is zero, in line with our previous explanations. The results are summarized in Eq. (25) below, while the thermodynamic details are given in the set of equations in Table 5 (in the appendix).

$$
\begin{aligned}
g_{O_i} &= 2\Delta G^{MOX}_{(U^{5+})(O^{2-})(Va)} \\
g_{V_O} &= \frac{1}{2}\Delta G^{MOX}_{(U^{4+})(Va)(Va)} - 2\Delta G^{MOX}_{(U^{5+})(O^{2-})(Va)} \\
g_e &= L^a_{(U^{3+},U^{4+})(O^{2-})(Va)} - L^b_{(U^{3+},U^{4+})(O^{2-})(Va)} + \Delta G^{MOX}_{(U^{3+})(Va)(Va)} - \Delta G^{MOX}_{(U^{4+})(Va)(Va)} + \Delta G^{MOX}_{(U^{5+})(O^{2-})(Va)} \\
g_h &= 0
\end{aligned}
\tag{25}
$$

This linearized version of the Calphad model of UO_2 will be named the "Guéneau model".

3 Synthesis of thermodynamic information

3.1 Comments on the atomistic-based models

Uranium reference

As noticed in Section (2.2), many of the defect thermodynamic data involving uranium defects are given in the $(UO_2\downarrow, O_2\uparrow, h$ or $VBM)$ references, whether it is defined as equilibrium reactions (21) (Andersson, Perriot) or in relation to the components chemical potential (16a) (Soulié). In these cases, the Gibbs energies are converted to the chosen reference $(U\downarrow, O_2\uparrow, h)$, using the TAF-ID for $\Delta g^0_{UO_2}$, whatever the model, since no data is provided for this function by the corresponding models. This choice for $\Delta g^0_{UO_2}$, apparently inconsistent, has no impact on the applications since the terms in $\Delta g^0_{UO_2}$ cancel out during the equation resolution because of Eq. (15a). Table (3) summarizes this information.

Oxygen reference

Most of the publications concerning the *ab initio* evaluation of the formation energies quoted here report a discrepancy of some tenths of eV between the calculated and measured formation energy at 0 K for UO_2, corresponding to the chemical reaction $U\downarrow + O_2\uparrow \rightleftarrows UO_2\downarrow$ [18, 3, 14, 40], although the use of VdW [52] gives very good results. More generally, oxide formation energies are not well reproduced by the *ab initio* DFT techniques used in the quoted papers, but other ab initio techniques (not reported here) give good results. Among the generally mentioned reasons is that such techniques devoted to solids are irrelevant for small molecules. Other problems may occur from the difficulty to produce a set of "unequivocal" "ab initio" constants (such as de DFT U and J parameters), that would be identical for metal and oxide uranium, this issue is addressed in more details in section 5. For these reasons, the O_2 molecule energy is corrected, and in some cases [14, 49], uranium oxide is chosen instead of metal as the uranium reference. This means the oxygen reference correction actually bears all the errors concerning the ab initio evaluation of the energies of O_2, U and UO_2. Three types of correction are reported, all based on replacing the oxygen energy by a value making it possible to reproduce the energy of a particular reaction (or a set of such reactions) while the other reactants/products of the reaction are calculated *ab initio*:

1. Reproduce the O_2 atomization reaction energy $O_2 \rightleftarrows 2O$, which means adding 0.9 eV to the O_2 molecule energy at 0 K in [40]. However, the authors underline that miscalculation of small molecules is not necessarily the only reason for this discrepancy, at least in the case of MnO_2. The same feature, calculated by other authors and/or other methods yields quite different correction values (e.g. 2.4 eV in LDA, 1.6 eV in GGA [5]).
2. Reproduce a particular oxidation reaction involving solid uranium phases, [20, 14]:

$$U\downarrow + O_2\uparrow \rightleftarrows UO_2\downarrow \tag{26}$$

or [3]:

$$4UO_2\downarrow + \frac{1}{2}O_2\uparrow \rightleftarrows U_4O_9\downarrow \tag{27}$$

Let us notice that other ab initio techniques, such as VdW-DF exchange-correlation functional, allow a much better evaluation of the UO_2 formation energy (see for instance Table 2 of [52]) and do not require an energy correction for oxygen.

3. Wang et al. [54] plotted the calculated formation energies against the measured formation energies for a series of oxides. The trend shows an average shift of 1.36 eV between the quantities, which is used as the basis to correct the calculated values.
4. We will also propose, Table 3, a correction based on the best fit between calculated and measured stoichiometry deviation as a function of oxygen potential.

The following examples give more detail on the corrections used for each model, among 1 to 3 above.

3.1.1 Andersson et al. [3] [2014]

Referring to [2], the authors obtain a better value of the oxygen reference energy using the fitting technique number 2 above based on the equilibrium UO_2/U_4O_9, Eq. (27). The calculated enthalpy is -1.36 eV while the experimental value is reported to be -1.8 eV, yielding a correction of 0.44 eV for the O_2 energy. According to this method, the O_2 correction captures indistinctly the errors concerning the gas molecule but also that concerning the oxide).

Entropy reaction values are calculated using the Basak potential [10] for U and O atoms. As polarons are not available in this kind of model, the electron-hole formation entropy, $0.73k_B$, is reported as the calculated value coming from other authors [28]; there seems to be an error, since $0.73k_B$ is actually the experimental value of [27], with the veritable calculated value of [28] being $1.1k_B$.

3.1.2 Vathonne et al. [53] [2014]

The formation thermodynamic parameters were not directly available in that publication. They were extracted from the graphs (Figure 3) showing $e_\nu - \boldsymbol{\nu}.\boldsymbol{\Delta\mu}$ as functions of $\Delta\mu_e$ for various values of $\Delta\mu_U$ and $\Delta\mu_O$. No correction is reported in the publication for the oxygen reference energy. The Madelung constant used in the article for energy correction was that of a fcc lattice (2.519), instead of that of a cubic lattice (2.8373); this point has been corrected in the values reported in Table 4. None of the defect formation entropies were calculated nor were the formation energy for the electronic defects (h° and e'). To provide an elementary assessment of the *ab initio* energies of this model, we define the lacking information as follows:

- energies for electronic defects are taken from [12] reported to use the same calculation methods
- entropies are from [49].

Since the data set is quite large and cannot be wholly presented in Table 4, the complete data set is gathered in Table 7.

3.1.3 Vathonne et al. [52] [2017]

This work is closely related to the previous study [53] by the same team; the improvement is essentially based on the use of the vdW-DF functional in the DFT calculation. The energies are somehow different from one model to the other, the discrepancies becoming rather large generally when uranium vacancies are involved (around 1 eV par V_U). As for the data of 2014, only energies at 0 K are provided (no entropies), but the data set is much larger and the electronic defects h° and e' are addressed additionally. For the comparison to the experiments we also used the entropies of [49] (in particular $s_{e'} = 0$). The complete data set is compared to that of 2014 in Table 7.

3.1.4 Cooper et al. [14] [2018]

In that article, what is called "defect energy" or "entropy" (ΔE, ΔS) results from the difference of two simulation boxes and corresponds to (δh_ν, δs_ν) according to our convention. At a given temperature T, the physically meaningful information, ($h_\nu = \delta h_\nu - \boldsymbol{\nu}.\boldsymbol{h^0}$, $s_\nu = \delta s_\nu - \boldsymbol{\nu}.\boldsymbol{s^0}$) requires a reference set of values $\boldsymbol{h^0}$, $\boldsymbol{s^0}$ (for the components U, O, e). Table 1 of the original article provides the energetic parameters δh_ν, δs_ν at 0 K but unfortunately does not give the reference information h^0 (while the corresponding entropies at 0 K are known to be zero). The best way we were able to use this defect model despite this flaw was to extract the formation Gibbs energies from the graph of Fig. 4 a showing the defect concentrations as functions of the oxygen pressure at 650 K and to deduce the corresponding entropies and enthalpies (for the CRG model). For this purpose, the δs_ν's of the article and s^0's of the TAF-ID were fitted as linear functions on the temperature in the ranges [650 K, 2000 K] and [650 K, 2700 K] respectively, yielding δc_ν, c_ν and s_ν according to Eq. 12b (both for CRG [15] and Busker [47] potentials). Eq. 10a was also used to roughly

evaluate the defect formation enthalpy of each defect at 0 K. For this rough estimation, the defect thermal capacities δc_ν were supposed to vary linearly between 0 K and an effective Debye temperature of 400 K and to remain constant above this temperature; the fairly arbitrary value of this model temperature has a slight influence on the defect enthalpy and provides anyway a better result than no correction. As noticed in Section 2.1.2 above, we use the oxygen standard chemical potential from CODATA at 0 K and from the TAF-ID for temperatures above 298 K; the latter slightly differs from that of the original article (Eqs. (9) and (10)) even if the misprints are disregarded (factor $\frac{1}{2}$ missing in (10) and undue in (9)). As reported in the article, the oxygen *ab initio* value for the reference energy has been corrected according to the fitting technique number 2 (using the oxidation reaction (26)); however, as the genuine *ab initio* reference energies for *U* and *O* are lacking, there is no way of knowing the real value of this oxygen energy correction. The Gibbs formation energy of UO_2, $\Delta g^0_{UO_2}$, necessary to calculate the uranium vacancy concentration according to Eq. (17), is from the experiments (TAF-ID), since the paper does unfortunately not give this information, it can be calculated from Table 1. The calculated values of the concentrations for the uranium bearing defects should be slightly different of what would be obtained on the basis of the atomistic evaluation of $\Delta g^0_{UO_2}$.

This fitting procedure ensures that, for the CRG model, the Gibbs energies are very close to that of Fig. 4 a for 650 K and are close to the theoretical values above this temperature, which is satisfying for the purpose of this paper. However, since the values at 0 K on which the Busker enthalpies exclusively relies, may be erroneous, the higher temperature values that we calculate for the Busker model are less reliable than for the CRG model.

3.1.5 Soulié et al. [49] [2018]

Similarly to Cooper et al. this article calculates the free energy differences δf_ν (that we suppose identical to δg_ν) from which $s_\nu\,(T_r)$ and c_ν were calculated; the fitting range for δf_ν is $[400\,\mathrm{K}, 1900\,\mathrm{K}]$. The formation enthalpies at 0 K, $h_\nu\,(0\,\mathrm{K})$, used in the calculations are from [12]; there is no correction for the oxygen molecule energy. Unlike other models, the reference for uranium is the chemical potential of *U* in stoichiometric UO_2, so that the reported value of the Gibbs formation energy of $V_U^{4'}$ is actually $g^*_{V_U^{4'}}$ in Eq. 18. The Gibbs formation energy of UO_2, $\Delta g^0_{UO_2}$, used to evaluate $g_{V_U^{4'}}$ from $g^*_{V_U^{4'}}$ is the experimental value, as was done for the CRG model above. Contrary to the case of Soulié, this choice for $\Delta g^0_{UO_2}$ has no impact on the defect concentrations, since the same quantity is removed in Eq. (17) for the concentration calculation. The effect on entropies of electronic defects are considered negligible, in particular for electrons and holes. Many complex defects were calculated (up to $(O_i)_5$) in [12] and [49], most of them were included in the present evaluation. To accelerate the calculations the following negligible defects were omitted: $(O_i)_4^{6'}$, $(O_i)_4^{7'}$, $(O_i)_4^{8'}$ and all the species of $(O_i)_5$.

3.1.6 Perriot et al. [43] [2019]

The relevant thermodynamic data are from Table 1 of [43] and are reported to be based on that of [3], but recalculated with larger super-cells to be consistent with the other results of the article. The Schottky defect (S) in [43] appears to be unbound, while the values proposed here in Table 4 are for the bound Schottky defect. For this reason no Schottky defect is reported for this model here. The Gibbs energy for $V_U^{4'}$, equivalent to that of the equilibrium $. \rightleftarrows V_U^{4'} + 4h^\circ + U\downarrow$, is deduced from the reaction data of Table 1 as $g_{V_U^{4'}} = \Delta g^0_S - 2\Delta g^0_{FP_O} + 2\Delta g^0_{O_I} - \Delta g^0_{UO_2}$. The Gibbs energy for $V_O^{2^\circ}$, equivalent to that of the equilibrium $2h^\circ \rightleftarrows V_O^{2^\circ} + 1/2O_2$, is deduced from the reaction data of Table 1 as $g_{V_O^{2^\circ}} = \Delta g^0_{FP_O} - \Delta g^0_{O_I}$.

3.2 Defect thermodynamic parameters

When available, Table 4 provides the formation energies and entropies at 900 K, and the heat capacities in the appropriate range for each model. As noticed above, according to the thermodynamic convention, what is actually written for each defect, ν, corresponds to the transformed Gibbs energy $g_\nu + \nu_e g_h$ of the genuine data g_ν and g_h of the publications. For the purpose of comparison, the parameters for a set of defects (FP_O, $e-h$, $V_O^{2^\circ}$, $V_U^{4'}$) are also plotted, see Figures 1 to 3; the models obtained by experimental fitting are also presented. In order to eliminate the influence of the *O* and *e* reference energies, appropriate combinations of defects were plotted such as the oxygen Frenkel pair "FP_O" and the electron-hole pair "$e-h$".

3.2.1 Energies at 0 K and Gibbs energies at 900 K

Figure 1 displays the defect energies at 0 K. Since the fitted models were calibrated at high temperature, the comparison of the parameters at 0 K is mostly valid for atomistic-based models. For the reactions involving no exchange with the environment (FP_O, $e-h$), the *ab initio* parameters are rather close to each other. For example, four of the five *ab initio* values for the O Frenkel pair are very close, but there is a large difference of 1.57 eV between Vathonne's models and the other ones. The *ab initio* values for the electron-hole pair energy of formation at 0 K somehow split in two groups: Andersson, Vathonne, Soulié one the one hand and Cooper, Busker, Perriot on the other hand. The presence of Perriot in the latter is surprising since its values are derived from those of Andersson. For the reactions involving the exchange of atoms with the environment ($V_O^{2^\circ}$, $V_U^{4'}$) the scatter is much higher, in line with the differences in the energy of the oxygen molecule.

Figure 2 displays the Gibbs energies at 900 K. The tendencies are very similar to that at 0 K.

3.2.2 Entropies at 900 K

The entropies are displayed in Figure 3. The atomistic entropies for the $e-h$ pair are rather close to each other; on the contrary, the fitted entropies are very scattered. The uranium vacancy entropies of CRG (or Busker) and Soulié are very different at 900 K. We can propose some hints to explain this large discrepancy. Soulié's model uses UO_2 as uranium reference (hence the * in above the data) so that according to Eqs. (18) and (14) the entropy is written:

$$s_{V_U^{4'}} = \delta s^*_{V_U^{4'}} - s^0_{UO_2} + 4\delta s_{h^\circ} + s^0_U$$

while CRG and Busker directly use the defect $V_U^{4'}$:

$$s_{V_U^{4'}} = \delta s_{V_U^{4'}} + 4\delta s_{h^\circ} + s^0_U$$

First, $s^0_{UO_2}$ should be calculated with Soulié's potential. As the data was lacking in the publication, we used its experimental value to compute $s_{V_U^{4'}}$ on the basis of the article value of $\delta s^*_{V_U^{4'}}$. The calculated values for $s^0_{UO_2}$ of CRG or Busker are roughly 2.5 to $4k_B$ lower than the experimental value respectively. Second, δs_{h° is zero in Soulié's model which is about $1k_B$ lower than for the other models. Third, there is no contribution to the scatter due to uranium entropy which is the same experimental value for both equations. Altogether, the scatter of parameter values combine to give an value in the range $[6.5k_B, 8k_B]$ which reduces the large scatter of $s_{V_U^{4'}}$ (10.5 to $13.3k_B$, see Table 4) to a more limited one for $\delta s_{V_U^{4'}}$ ($4k_B$).

h°	e'	V_O	V_{O_2}	O_i	O_{i_2}	O_{i_4}	V_U	V_{UO}	V_{UO_2}
1	1	2	6	1	8	12	1	8	12

Table 2: Configuration numbers for the various defects (regardless to the charge)

Model	Ref. U	$\mathrm{d}\mu^0_O$ (eV)
Nakamura 86	UO_2	0.121
Park 92	UO_2	-0.102
Gueneau 11	UO_2	-0.241
Garcia 17	UO_2	0.095
Andersson 14	UO_2	-0.195
Vathonne 14	U	1.043
Vathonne 17	U	0.868
CRG 18	U	0.468
Busker 18	U	0.566
Soulié 18	UO_2	1.307
Perriot 19	UO_2	-0.114

Table 3: Reference for U and shifts in μ^0_O according to a least squares fitting with the experimental data

Model	**Energy (0 K) (eV)**					**Energy (900 K) (eV)**					**Entropy (900 K) (k_B)**					**Thermal capacity (k_B)**				
	h°	$e^{'}$	$V_O^{2\circ}$	$O_i^{2'}$	$O_i^{'}$	h°	$e^{'}$	$V_O^{2\circ}$	$O_i^{2'}$	$O_i^{'}$	h°	$e^{'}$	$V_O^{2\circ}$	$O_i^{2'}$	$O_i^{'}$	h°	$e^{'}$	$V_O^{2\circ}$	$O_i^{2'}$	$O_i^{'}$
Nakamura 86	0	2.00	5.79	-0.50		0	2.00	5.79	-0.50		0	5.01	21.02	-6.50		0	0	0	0	
Park 92	0	1.57	5.52	-2.17		0	1.57	5.52	-2.17		0	-3.05	20.67	-22.14		0	0	0	0	
Gueneau lin 11	0	1.89	4.03	-1.21		0	1.89	4.03	-1.21		0	1.86	10.93	-10.93		0	0	0	0	
Garcia 17	0	2.24	3.03	-0.83		0	2.24	3.03	-0.83		0	1.16	14.62	-16.69		0	0	0	0	
Andersson 14	0	1.75	4.84	-0.50		0	1.75	4.84	-0.50		0	0.73	15.74	-5.20		0	0	0	0	
Vathonne 14	0	1.71	2.60	0.09	-0.09	0	1.71	2.50	0.19	0.02	0	0	11.77	-4.63	-4.63	0	0	-0.72	0.74	0.74
Vathonne 17	0	2.04	2.55	0.21	-0.07	0	2.04	2.44	0.31	0.03	0	2.00	11.77	-4.63	-4.63	0	0	-0.72	0.74	0.74
CRG 18	0	1.45	4.55	-0.38		0	1.46	4.49	-0.24		0	2.42	14.04	-3.87		0	0.08	-1.29	2.42	
Busker 18	0	1.45	4.55	-0.38		0	1.44	4.45	-0.23		0	3.07	13.69	-5.39		0	-0.14	-1.96	2.63	
Soulié 18	0	1.71	2.74	1.57	1.11	0	1.71	2.63	1.67	1.21	0	0	11.77	-4.63	-4.63	0	0	-0.72	0.74	0.74
Perriot 19	0	1.36	4.78	-0.95		0	1.36	4.78	-0.95		0	0.73	13.25	-7.55		0	0	0	0	
	$V_{O_2}^{2\circ}$	$O_{i_2}^{'}$	$O_{i_4}^{3'}$	$V_{UO}^{2'}$	$V_{UO_2}^{\times}$	$V_{O_2}^{2\circ}$	$O_{i_2}^{'}$	$O_{i_4}^{3'}$	$V_{UO}^{2'}$	$V_{UO_2}^{\times}$	$V_{O_2}^{2\circ}$	$O_{i_2}^{'}$	$O_{i_4}^{3'}$	$V_{UO}^{2'}$	$V_{UO_2}^{\times}$	$V_{O_2}^{2\circ}$	$O_{i_2}^{'}$	$O_{i_4}^{3'}$	$V_{UO}^{2'}$	$V_{UO_2}^{\times}$
Nakamura 86		-2.55					-2.55					-8.45					0			
Park 92	10.60	-3.21				10.60	-3.21				30.58	-17.36				0	0			
Gueneau lin 11																				
Garcia 17		-2.32					-2.32					-8.68					0			
Andersson 14		-1.66	-4.72	12.81	16.26		-1.66	-4.72	12.81	16.26		-4.36	-10.40	14.78	28.62		0	0	0	0
Vathonne 14																				
Vathonne 17																				
CRG 18																				
Busker 18																				
Soulié 18		1.31	1.66				1.50	2.04				-8.76	-17.88				1.43	2.84		
Perriot 19																				0
	$V_U^{4'}$	$V_U^{3'}$	$V_U^{2'}$	$V_U^{'}$	$V_U^{\times}$	$V_U^{4'}$	$V_U^{3'}$	$V_U^{2'}$	$V_U^{'}$	$V_U^{\times}$	$V_U^{4'}$	$V_U^{3'}$	$V_U^{2'}$	$V_U^{'}$	$V_U^{\times}$	$V_U^{4'}$	$V_U^{3'}$	$V_U^{2'}$	$V_U^{'}$	$V_U^{\times}$
Nakamura 86																				
Park 92																				
Gueneau lin 11																				
Garcia 17																				
Andersson 14	9.43	9.00	8.92	8.82	8.64	9.43	9.00	8.92	8.82	8.64	3.24	3.24	3.24	3.24	3.24	0	0	0	0	0
Vathonne 14	10.65	10.18		10.10		10.08	9.62		9.53		-4.57	-4.57		-4.57		-8.31	-8.31		-8.31	
Vathonne 17	11.52	11.41		11.29		10.95	10.85		10.73		-4.57	-4.57		-4.57		-8.31	-8.31		-8.31	
CRG 18	9.03					9.11					8.31					2.37				
Busker 18	9.03					9.17					5.91					3.25				
Soulié 18	11.50	11.24	11.10	10.69		10.98	10.72	10.58	10.17		-4.57	-4.57	-4.57	-4.57		-8.31	-8.31	-8.31	-8.31	
Perriot 19	8.07					8.07					1.93					0				
	$O_{i_2}^{\circ}$	$O_{i_2}^{2'}$	$O_{i_2}^{4'}$			$O_{i_2}^{\circ}$	$O_{i_2}^{2'}$	$O_{i_2}^{4'}$			$O_{i_2}^{\circ}$	$O_{i_2}^{2'}$	$O_{i_2}^{4'}$			$O_{i_2}^{\circ}$	$O_{i_2}^{2'}$	$O_{i_2}^{4'}$		
Nakamura 86																				
Park 92																				
Gueneau lin 11																				
Garcia 17																				
Andersson 14																				
Vathonne 14	0.75	0.60	1.11			0.94	0.79	1.30			-8.76	-8.76	-8.76			1.43	1.43	1.43		
Vathonne 17	0.41	0.42	1.09			0.60	0.61	1.27			-8.76	-8.76	-8.76			1.43	1.43	1.43		
CRG 18																				
Busker 18																				
Soulié 18		2.02	3.29				2.20	3.47				-8.76	-8.76				1.43	1.43		
Perriot 19																				

Table 4: Thermodynamic parameters of the various defect models (the complete data sets for Soulié and Vathonne 14 and 17 are given Table 6).
When relevant, the Gibbs formation energy for UO_2 used to convert g_v^* to g_v is from the TAF-ID (Table 1).

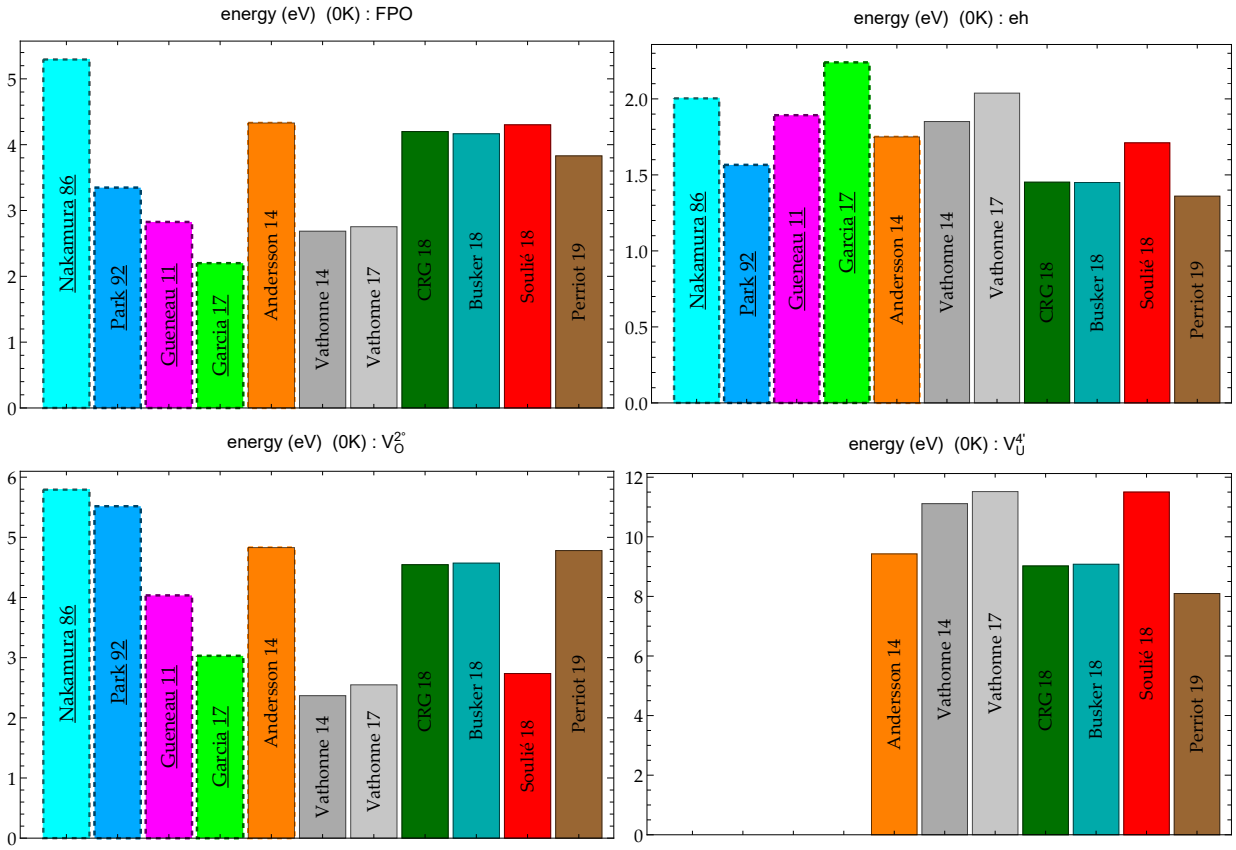

Figure 1: Comparison of the models: formation energy at 0 K
The fitted models correspond to dotted edges

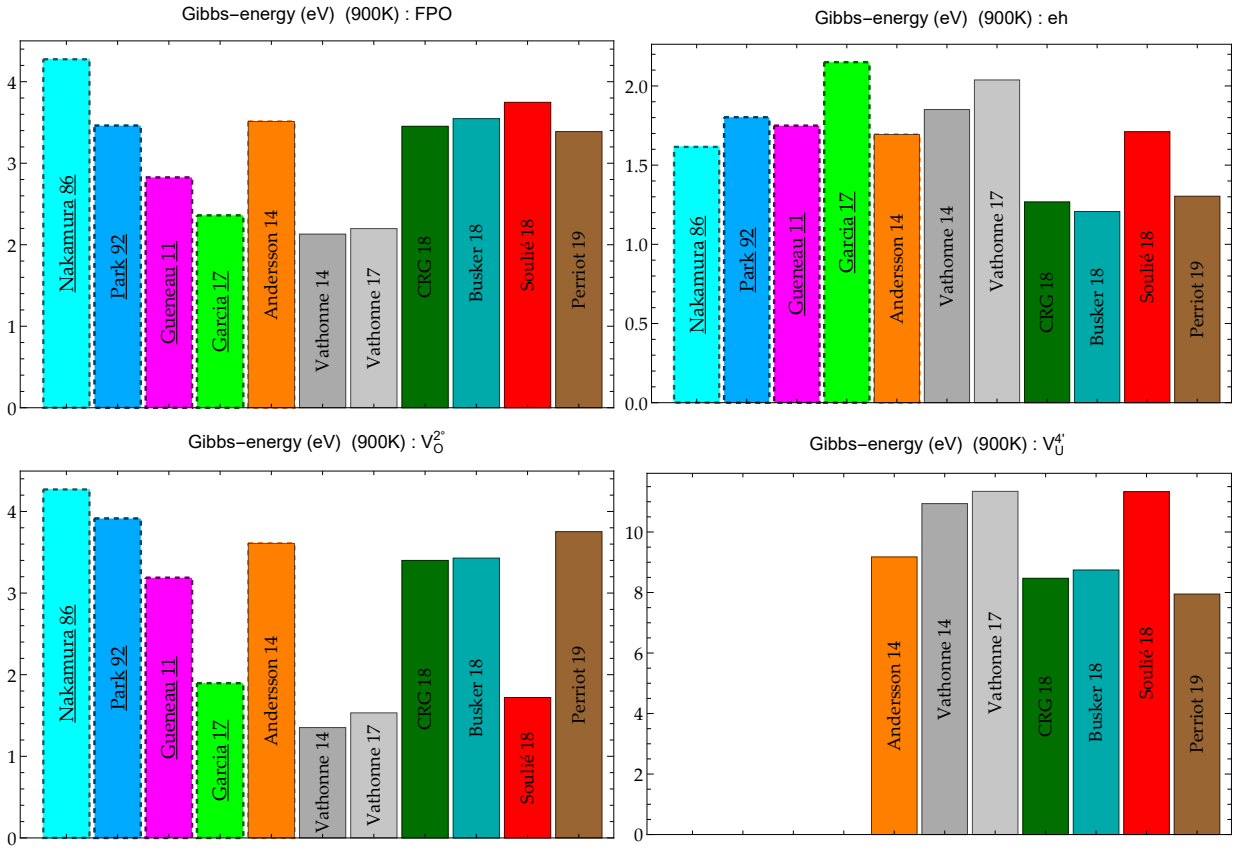

Figure 2: Comparison of the models: Gibbs formation energy at 900 K
The fitted models correspond to dotted edges

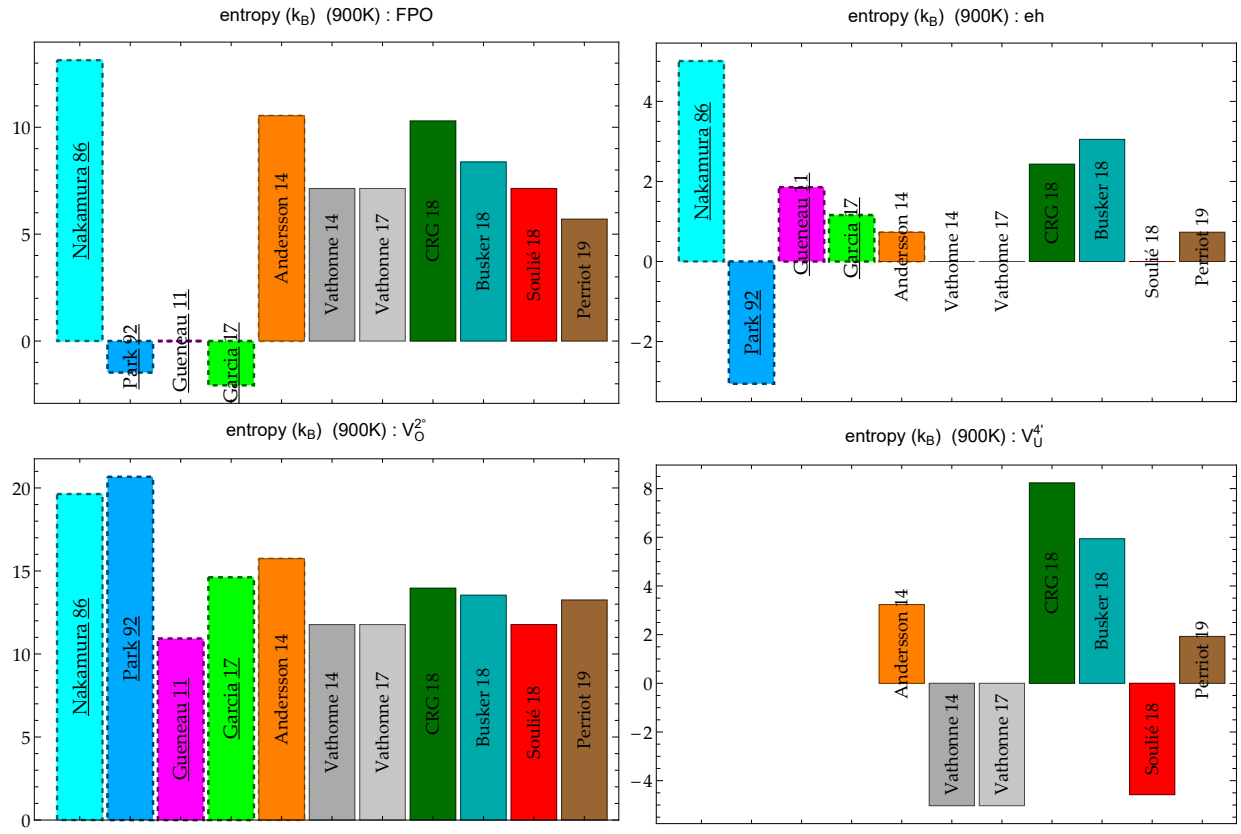

Figure 3: Comparison of the models: formation entropy at 900 K
The fitted models correspond to dotted edges

3.2.3 First application: calculating the defect concentrations

The direct application of the thermodynamic parameters described above is the calculation of the equilibrium defect concentrations as functions of the oxygen chemical potential and temperature (solving Eq. (6a)-(6g)). For instance, Figure 16 in the appendix allows for a comparison of the models at an intermediate temperature of 1600 K.

Although the quantitative results are very different among the models, the general trends are in general qualitatively rather similar in many respects. Except for Vathonne's models, electronic defects (e' and h°) are dominant around stoichiometric UO_2 at all temperatures; oxygen single defects ($V_O^{2\circ}$ or $O_i^{2'}$) are generally dominant further from the stoichiometry (respectively in the hypo and hyper–stoichiometric regions).

Besides this relative uniformity, differences still occur. In the models of Cooper (CRG and Busker), Soulié and Perriot, the uranium vacancy formation Gibbs energy is low enough to allow this defect to explain x at high oxygen potential. In the same line, large values of x are accounted for by the oxygen interstitial clusters in the models of Nakamura, Park, Garcia and Andersson. Moreover, the electronic defect concentrations are particularly low for the model of Garcia, in line with the high value for the formation energy of the electron-hole.

As noticed above, Vathonne's model provides a special case: at high temperature, the concentration of the oxygen defects is much higher than that of the electronic defects, unlike the other models, because of the very low value of the Frenkel pair formation energy compared to that of the electron-hole. This trend is enhanced at higher temperature (see Figure 17 in appendix). Moreover the presence of negatively charged oxygen vacancies ($V_O^{'}, V_O^{2'}$) is very original and has a strong impact on the defect behavior. In fact, in most models, the electroneutrality is controlled by both oxygen and electronic defect and the corresponding equation reduces to $e' = 2V_O^{2\circ}$ and $h^\circ = 2O_i^{2'}$ in the near hypo/hyper stoichiometric regions respectively; here the electroneutrality is under control of the oxygen defects on the whole oxygen potential range, according to the equations $2V_O^{2\circ} + V_O^{\circ} = 2V_O^{2'}$ or $2V_O^{2\circ} = 2O_i^{2'}$. The $O_i^{2'}$ concentration is still rather high in the hypo-stoichiometric region.

The general trends emphasized here usually appear at all temperatures, but this may suffer exceptions, for instance (Figures 15 and 17):

- the uranium vacancies do not control x at lower temperature in the models of Cooper, Soulié and Perriot;
- at 900 K and high oxygen potential, x is controlled by the oxygen tetra-interstitial in Vathonne 14 and by the uranium vacancies in Vathonne 17.

4 Comparison with experiments

We tried to derive observable quantities from the various defect models studied here and compare them to available experimental data, such as basic bulk thermodynamic properties, electron-hole Gibbs formation energy, phase diagram in the vicinity of UO_{2+0}, and deviation from stoichiometry or electric conductivity as functions of the temperature and of the oxygen potential.

4.1 UO_2 thermodynamic properties

The general ability of the simulation techniques can also be evaluated through the thermodynamic functions of the bulk material, which should be better reproduced than defect quantities since they are more easily calculated, notably by *ab initio* techniques.

Some of the atomistic models give useful and precise information on UO_2 thermodynamics. As already mentioned, the formation enthalpy of [51] and [52] are -10.54 eV and -11.3 eV respectively, the second being very close to the experimental value of -11.3 eV (according to the TAF-ID database and the CODATA database for 0 K values). Unfortunately, the other articles addressed here do not give enough information for calculating the UO_2 formation enthalpy.

However, experimental and simulated entropies and heat capacities for bulk UO_2 obtained from the CRG and Busker models [14] are compared in Figure 4. The heat capacity at constant volume and pressure, $c^V_{UO_2}$ and $c^P_{UO_2}$, have been evaluated following the publication indications and according to the thermodynamic

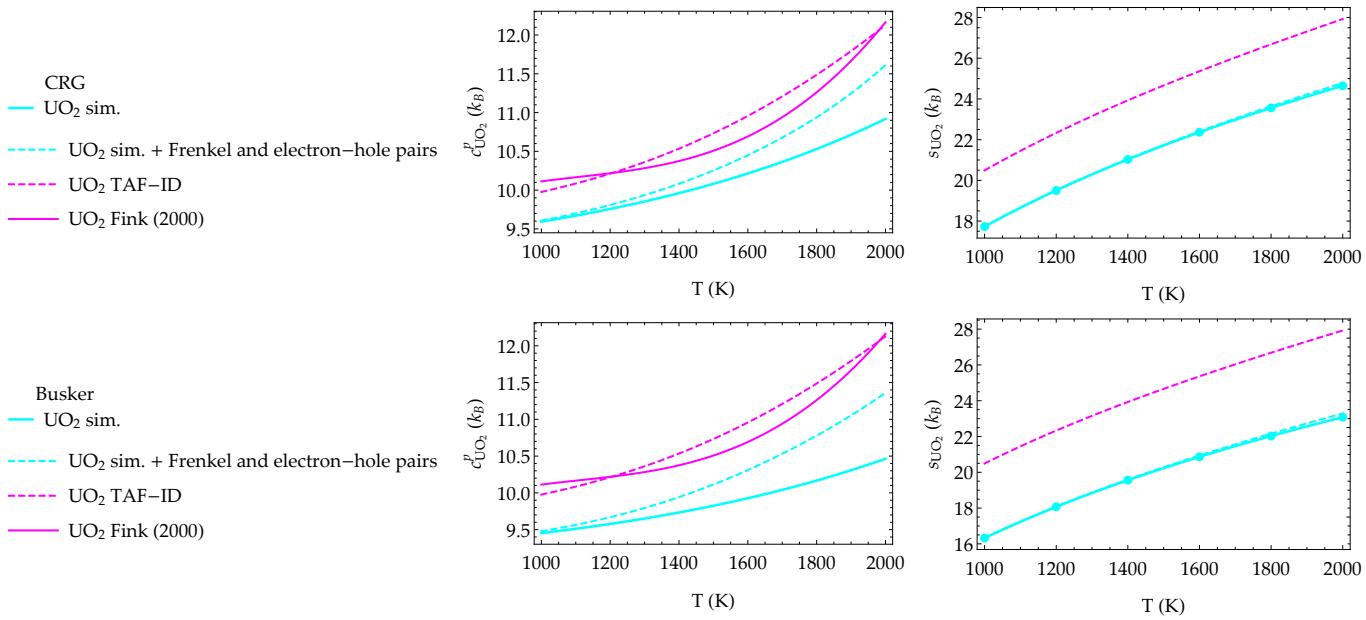

Figure 4: Comparison of calculated and measured (TAF-ID) entropies and heat capacities for UO_2

relation:

$$\left.\frac{\partial S}{\partial T}\right|_P = \left.\frac{\partial S}{\partial T}\right|_V + \left.\frac{\partial V}{\partial T}\right|_P \left.\frac{\partial S}{\partial V}\right|_T \tag{28}$$

or equivalently:

$$\begin{aligned} c^P_{UO_2} &= c^V_{UO_2} + T \left.\frac{\partial \Omega}{\partial T}\right|_P \left.\frac{\partial S}{\partial V}\right|_T \\ c^V_{UO_2} &= 9k_B \end{aligned} \tag{29}$$

where the basic data come from [14], where $\Omega(T)$ is the measured UO_2 unit cell volume given in [19] and shifted so that it gives 5.47 Å at 0 K. We suppose that S at zero pressure is given in Tables 2 and 3, $\left.\frac{\partial S}{\partial V}\right|_T$ in Table 4 (0.341 $k_B/Å^3$ and 0.447 $k_B/Å^3$ for Busker and CRG resp.), and that the Dulong Petit relation for $c^V_{UO_2}$ is valid (as stated Eq. 3 of [14]). An additional contribution to the entropy (s_{def}) is tested (dashed cyan lines) corresponding to the formation of the oxygen Frenkel and electron-hole pairs during temperature increase of a pure and perfectly stoichiometric UO_2:

$$s_{def} = \left(s_{O_i^{2\prime}} + s_{V_O^{2\circ}}\right)\sqrt{2}\exp\left(\frac{g_{O_i^{2\prime}} + g_{V_O^{2\circ}}}{2k_BT}\right) + \left(s_{e^\prime} + s_{h^\circ}\right)\exp\left(\frac{g_{e^\prime} + g_{h^\circ}}{2k_BT}\right).$$

This defect contribution to the entropy (s_{def}) is negligible (max $0.14k_B$), although it is not to the thermal capacity ($T\partial_T s_{def}$, i.e. $0.7k_B$ at 2000 K) (Figure 4).

The simulated variations with the temperature are quite close to that of the experimental data, as shown particularly by the $c^P_{UO_2}$ graph including the defect correction ($\partial_T s_{def}/T$).

4.2 UO_2 electron-hole Gibbs formation energy as a function of the temperature

Figure 5 presents the various models for the electron-hole Gibbs energy of formation as a function of temperature. As noticed in Section 3.2.1, the models gather in two groups: CRG, Busker and Perriot on one side and Andersson and Vathonne on the other side. The band gap values deduced from UV-VIS-NIR optical absorption measurements of [45, 44] are also plotted for comparison. They are very far from all model values, except Nakamura 86. However we could not undoubtedly assume that the physical quantity measured in Ruello's publications was actually the defect Gibbs energy as evaluated in the present work.

4.3 Deviation from stoichiometry versus oxygen chemical potential

Many measurements of the deviation from the stoichiometry, x, as a function of the oxygen potential μ_O and the temperature T are available. Since the data in the literature is very scattered, considerable

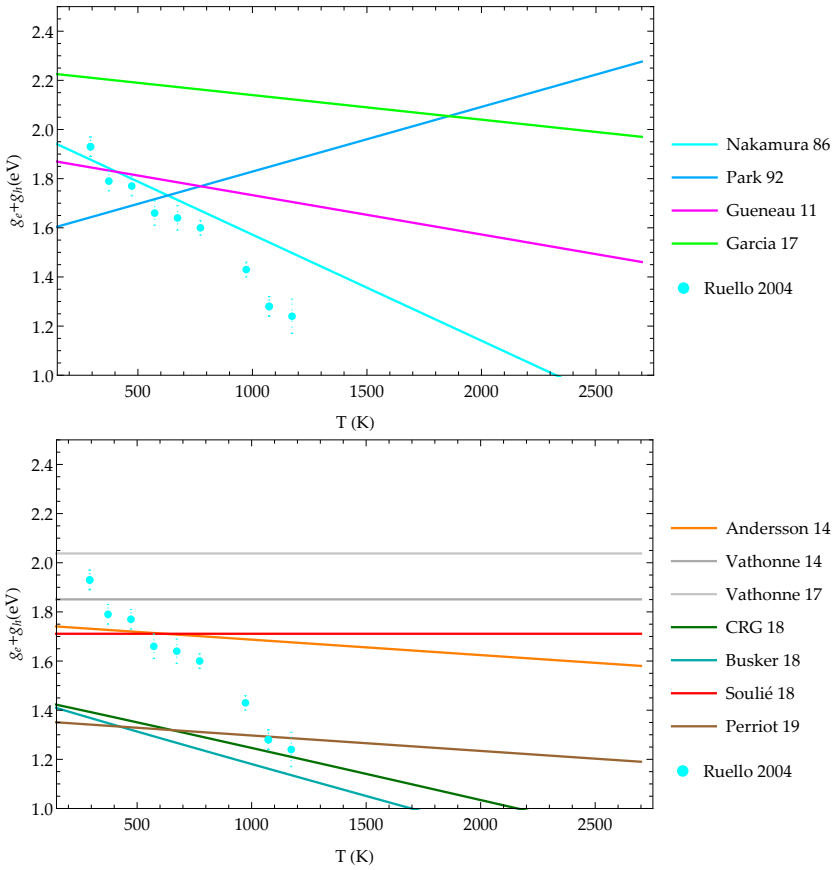

Figure 5: Comparison of the models with experiments [45]: electron-hole Gibbs formation energy vs temperature

efforts have been made to rationalize them: [7, 8] for the hypo-stoichiometric region, [32, 33] for the hyper-stoichiometric region. The Calphad [24, 25] and Guéneau models, corresponding to the TAF-ID, are grounded on the resulting selected data. Because of this careful selection and the important applications enabled by the TAF-ID in the nuclear materials field, we also chose this experimental set of data as reference for our validation. The simulated and measured variations of x as a function of $\Delta\mu_O$ for a large range of temperatures (900-2700 K) are shown in Figures 6-7 (for the fitted models) and 8-9 (for the atomistic-based ones).

To summarize, Figure 10 presents the temperature variation of the stoichiometric oxygen potential for the different models, including the shifted ones. For all the models, this chemical potential is approximately given by the following equation, except for Garcia's model, as noticed in Section 4.3.2:

$$\Delta\mu_O^{sto} = \frac{1}{2}\left(g_{O_i} - g_{V_O} + k_B T \ln(2)\right) - \left(g_e - g_h\right). \tag{30}$$

4.3.1 The atomistic-based models

Scatter is also very large for the atomistic-based models (Figure 8).

A comprehensive overview concludes Andersson's model to be the only one showing a correct agreement with the experiments across the whole temperature range. Indeed, in Figures 8 and 10c, the position of the UO_2 stoichiometric oxygen potential appears to be more or less shifted for all the models, suggesting that the oxygen references of the models might be erroneous. The relative success of Andersson's model in this issue suggests that we can use the same procedure for the O energy fitting, i.e. reproducing the oxidation energy of UO_2 into U_4O_9, see Eq. (27). This is actually not possible with the thermodynamic parameters made available in the publications considered here. As a backup, for each atomistic-based defect model, we propose to shift the oxygen standard potential, μ_O^0, by a quantity $\mathtt{d}\mu_O^0$. The Gibbs energy of a defect g_ν is then transformed to $g_\nu - \nu_O \mathtt{d}\mu_O^0$. The same is done for the equation of C_0 (15a): an error of $\mathtt{d}\mu_O^0$ on μ_O^0 yields a shift of $-2\mathtt{d}\mu_O^0$ on $g_0 = \Delta g^0_{UO_2}$. For this reason, to obtain the graph $x = f(\Delta\mu_O)$ of a set of parameter with μ_O^0 shifted of $\mathtt{d}\mu_O^0$ we just have to shift the abscissa of the initial graph by an amount of $-\mathtt{d}\mu_O^0$. It is then possible to give a best estimate of $\mathtt{d}\mu_O^0$ for a given model by a least squares fitting of $\Delta\mu_O$ to the experimental data of Figure 8, which yields $\mathtt{d}\mu_O^0 = \left\langle \Delta\mu_O^{sim} - \Delta\mu_O^{exp} \right\rangle$.

To improve the fitting procedure we excluded the irrelevant experimental data. The slope, $^{d\log(|x|)}/_{d\Delta\mu_O}$, in the graph is under control of the charge and oxygen composition of the main defects, namely, in our case,the larger slopes are related to oxygen interstitial clusters ($O_{i_{n,n>1}}$). According to this, a better fitting can be obtained for models devoid of such clusters if the data points corresponding to the larger slopes are removed from the experimental set. The models Vathonne 17, CRG, Busker and Perriot (as well as Guéneau among the fitted models) were processed this way (this mostly induced to remove the data for $T \leq 1600\,\mathrm{K}$ and $\Delta\mu_O > -1.4\,\mathrm{eV}$, cf. Figure 18 in the appendix). Table 3 gathers the resulting shifts. Figure 9 presents the new variations of x after the corresponding shifts. In a view of being comprehensive, we also calculated the shifts for the "fitted" models, although the shifts are rather small, in line with the fact that these models have already be fitted.

Various features of the graphs deserve comments (shifted models only are addressed, unless specifically mentioned).

- Andersson's model behaves much better than the genuine one at low temperature and high oxygen potential, where di-interstitials dominate, while the agreement with experiments at higher temperature is fairly unchanged.
- Both Vathonne's models appear quite far from the experimental data, except at low temperature (up to 1200 K), in the hyper-stoichiometric zone. The behavior in the hypo-stoichiometric domain at high temperature is quite puzzling, since although the shifted curves cross the point cloud, their slopes remain very different from it. This very likely comes from the presence of negatively charged oxygen defects masking the electronic ones in the hypo-stoichiometric region (as noticed in Section 3.2.3), which changes the slope $^{d\log(|x|)}/_{d\Delta\mu_O}$.
- CRG and Busker models behave correctly in the hypo-stoichiometric (high temperature) region, and poorly in the hyper-stoichiometric (low temperature) region.
- Soulié's model behaves quite well in the hypo-stoichiometric domain (at high temperature). In the hyper-stoichiometric one, at lower temperature, the behavior is fairly correct close enough to the perfect stoichiometry, where x is controlled by the concentration of V_U or O_i; for larger values, x is controlled by the clusters of oxygen interstitial atoms (see Figures 15, 16, 17) and hardly reproduces the experimental slope, this seems to be connected to the characteristics of the main interstitial clusters of the model (O_{i_4} of various charges) which do not account for a slope of 1, as does the standard di-interstitial $W = O'_{i_2}$ for other models. Although there are no experimental data in the low hyper-stoichiometry and low temperature region to say whether a model behaves well or not, we should consider that Andersson's model is better because at that temperatures it works for a larger range of x.
- Perriot's model (whose shift, -0.114 eV is very small) behaves well in the hypo-stoichiometric regime, and quite poorly in the hyper-stoichiometric. Equations (5) and (6) of [43] suggest the oxygen vacancy formation entropy might have been fitted on experimental results at 1973 K; this may be an explanation for this very good performance. Let us notice that this fitting procedure interferes with our fitting (-0.114 eV) of the oxygen potential at 0 K in some complicated way.

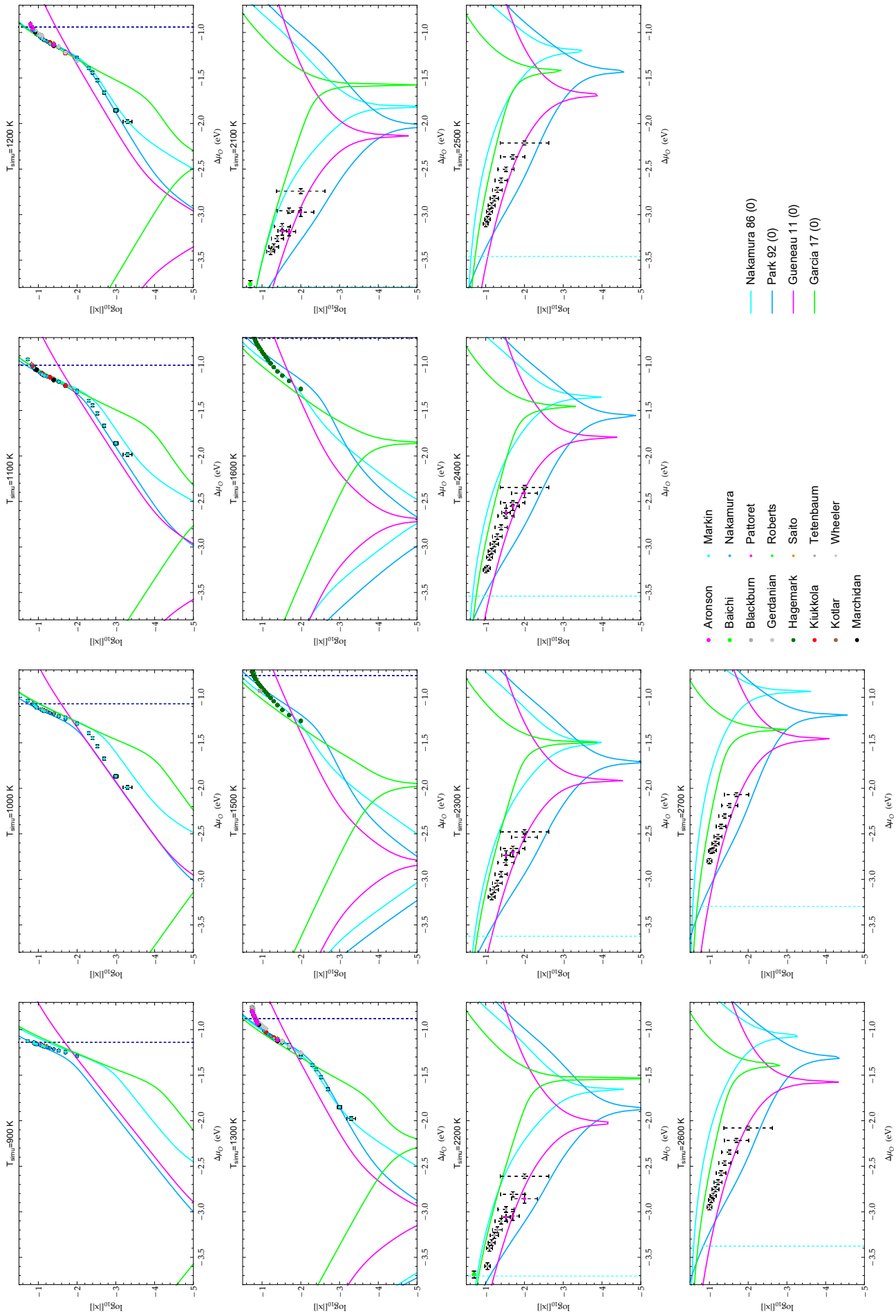

Figure 6: Comparison of the fitted models with experiments [32, 7, 8]: deviation from stoichiometry
The light and dark vertical blue lines show the oxygen potential for the equilibrium U/UO_2 and UO_2/U_4O_9 respectively, as calculated from the TAF-ID

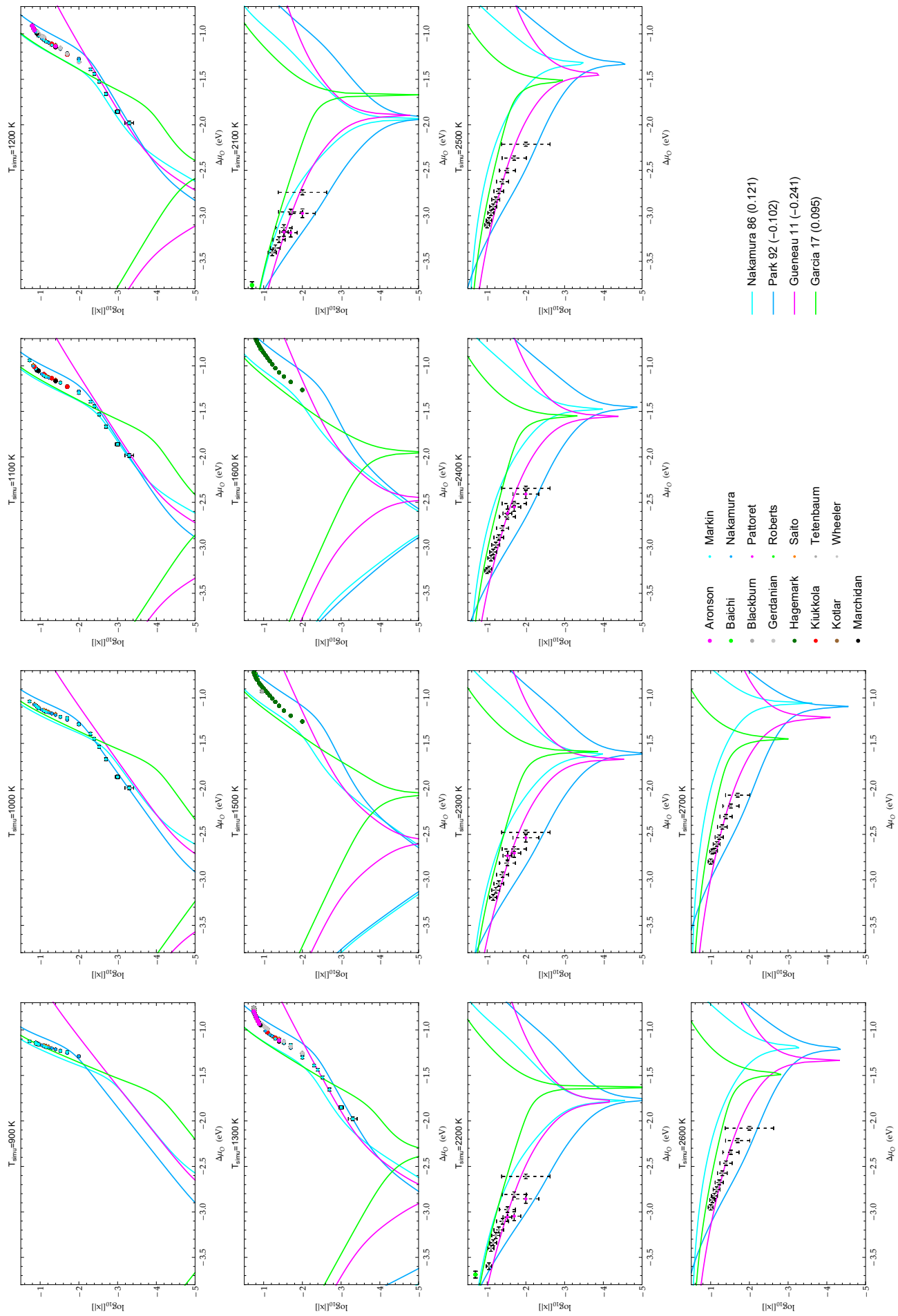

Figure 7: Comparison of the shifted fitted models with experiments [32, 7, 8]: deviation from stoichiometry

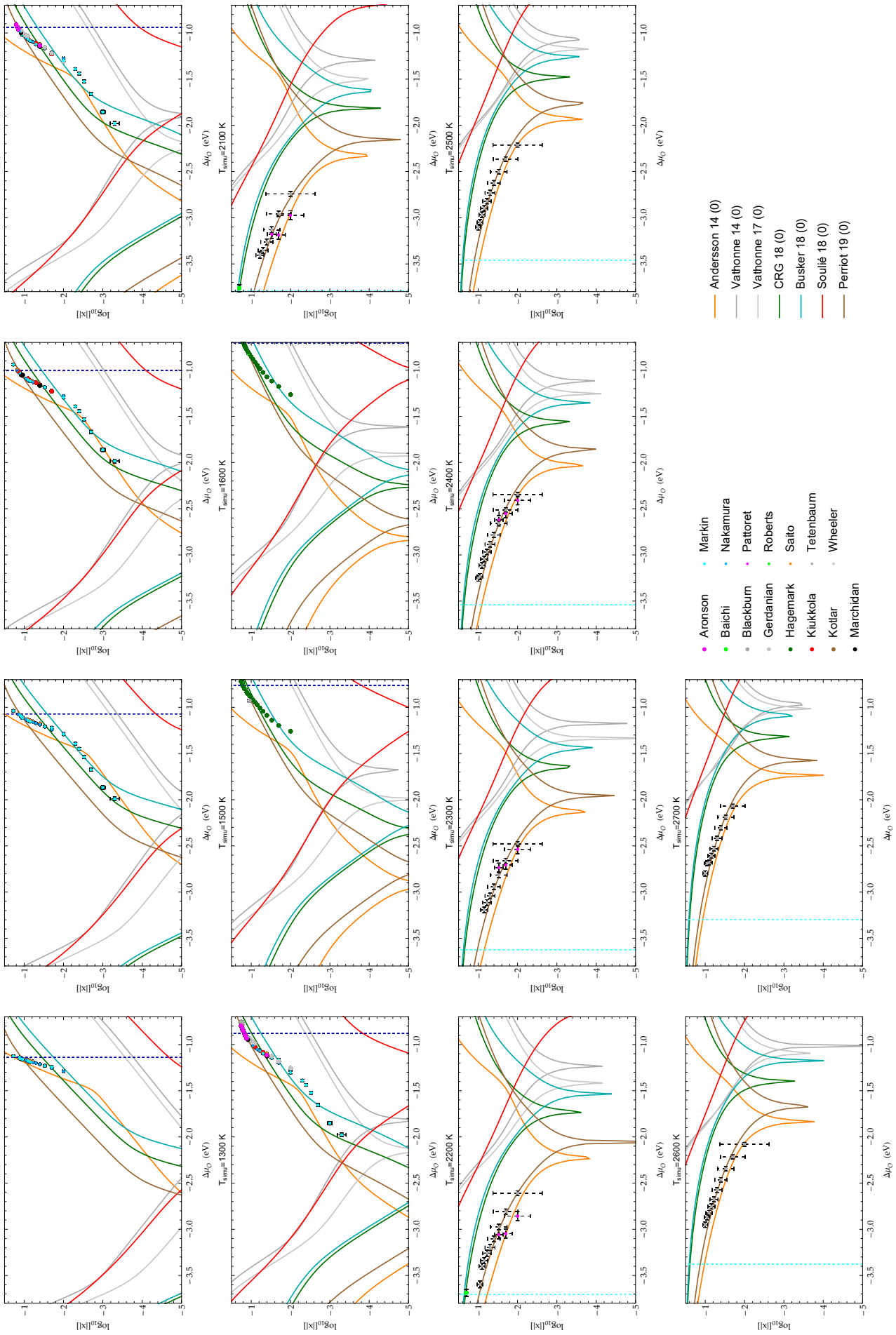

Figure 8: Comparison of the atomistic models with experiments [32, 7]: deviation from stoichiometry
The light and dark vertical blue lines show the oxygen potential for the equilibrium U/UO_2 and UO_2/U_4O_9 respectively, as calculated from the TAF-ID

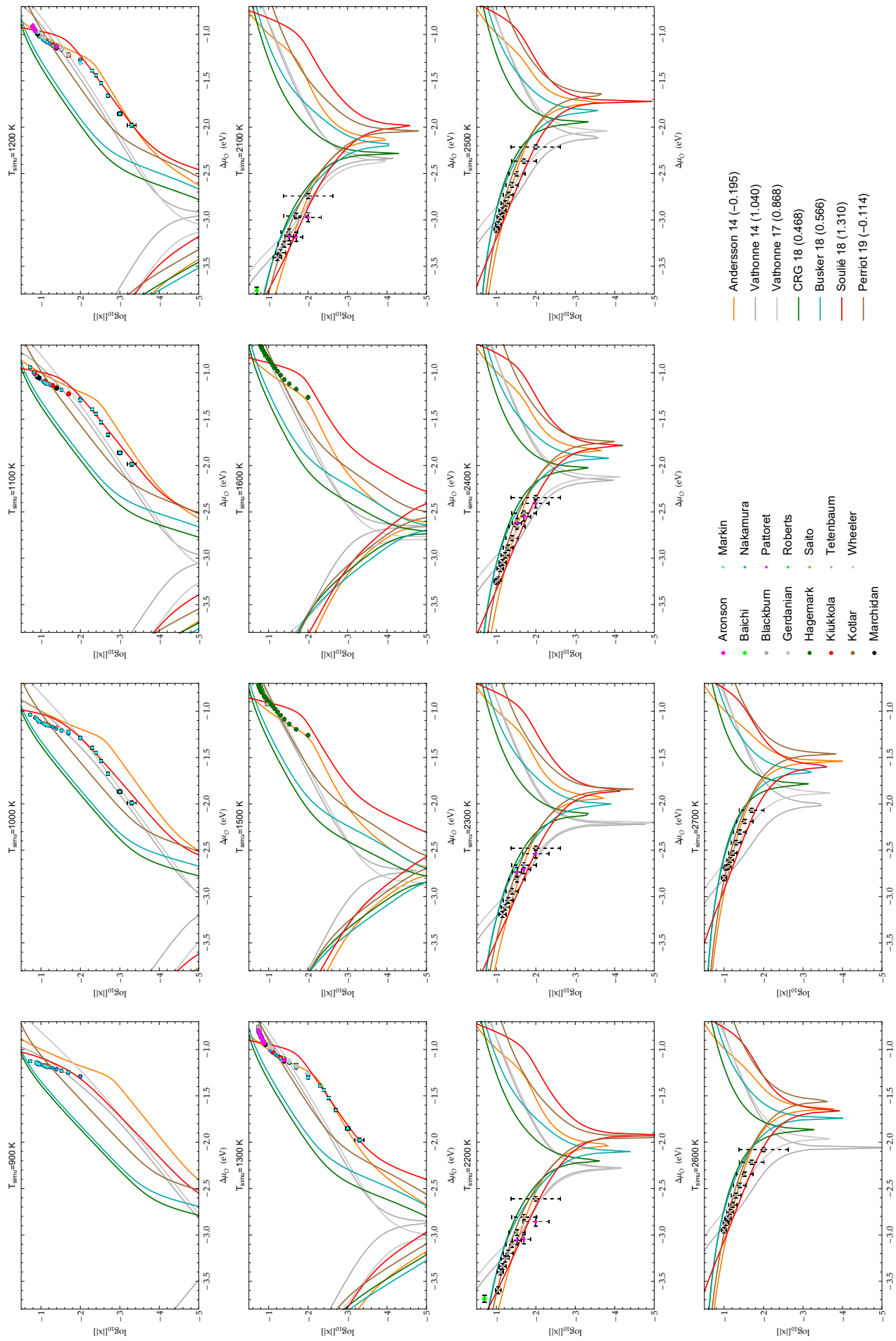

Figure 9: Comparison with experiments of the atomistic models shifted (least squares fitting with the experimental data [32, 7, 8]): deviation from stoichiometry

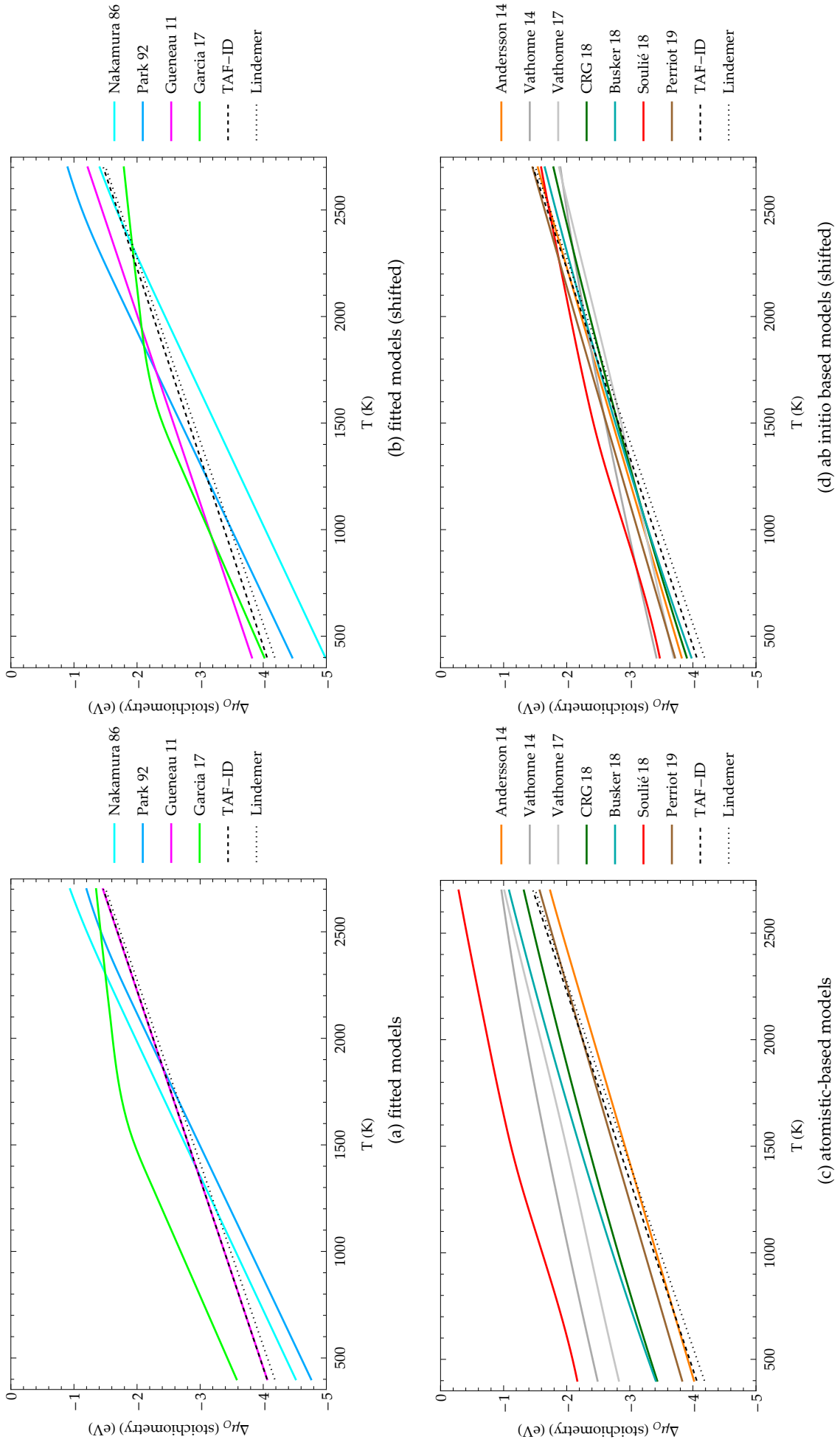

Figure 10: Comparison of the models: oxygen potential at stoichiometry versus temperature

4.3.2 The fitted models

As a preliminary remark, we may say that as expected, the shifts $\mathrm{d}\mu_O$ appear fairly small considering these models have already been fitted according to similar data sets. Additionally, we can see that no two models overlap for the whole oxygen potential range, which can be partially understood.

- Nakamura's model [37] is grounded on data in the $0 < x \leq 0.05$ range, which explains why it behaves correctly mainly in the hyper-stoichiometric region, as can be seen by comparison with the experimental data for temperatures below and above 2000 K, which addresses the hyper- and hypo-stoichiometric regions respectively.
- The data used by Park [41] and Guéneau [25] comprises various subsets gathered in [34]. Surprisingly, the models do not perform the same way at all. Park's results are particularly close to the experimental data in the hyper-stoichiometric range, and also rather close to the results of Nakamura. Guéneau does not fit them very well, especially in regions far from $x = 0$, where the Willis cluster is predominant, in line with the absence of this defect in the model. In this region, the linearized model is oversimplified and cannot behave so well as the genuine one; in particular, the region with a higher slope (i.e. for $x > 0.01$) is generally accounted for by the di-interstitial oxygen atoms in other models, and are here probably accounted for by the excess term of the Gibbs energy (Eq. (23)), which has been partly removed in the linearized model. In the hypo-stoichiometric range, Guéneau is closer than Park to the measurements, probably because x is controlled by the oxygen single vacancy which is part of the linearized model. Nakamura remains far from both models, but rather close to Garcia's results.
- Garcia's model performs quite well in the region where the Willis cluster W is dominant, which corresponds to the case where the conductivity (proportional to the hole concentration) is controlled by the predominant oxygen defect concentration which is always W in this region (Figure 11). This means that for high oxygen potential, the conductivity is a measure of W concentration and the model fits well both for conductivity and stoichiometry deviation measurements. This is in line with the peculiar behavior of the stoichiometric oxygen chemical potential of this model (Fig. 10, green curve) which corresponds, only at high temperature, to the equation $C_W = C_{V_O}$, giving rise to a different slope in the graph, instead of the usual situation where the equality $C_{O_i} = C_{V_O}$ and Eq. (30) stand at all temperatures. In the plateau regions of the curve, $e + h$ corresponds to the electroneutrality equation $C_h \sim C_{dop}$ since various defect concentrations are negligible compared to the impurity's. According to Figure 11 based on the model results, there is practically no experimental data where $O_i^{2'}$ or $V_O^{2\circ}$ impact the conductivity: we should not expect a good precision on the corresponding thermodynamic parameters, thus explaining the poor agreement, Figure 6, between calculated and measured deviation from the stoichiometry where W is not predominant.

4.4 Electric conductivity versus oxygen chemical potential

While Nakamura, Park and Guéneau developed their models based on measurements of the deviation from stoichiometry, Garcia [21] developed his on the basis of electric conductivity measurements by Ruello [46]. Figures 12a, 12c and 12d compare the modeling and experimental results. The conductivity (σ) measurements were transformed into total electronic defect concentrations according to the relation:

$$\sigma = q \frac{m_e}{T} e^{-\frac{H_e^m}{k_B T}} n_{UO_2} \left(C_e + C_h\right)$$

in which $q = 1.602 \times 10^{-19}\,\mathrm{C}$, $n_{UO_2} = 2.5 \times 10^{28}\,\mathrm{m}^{-3}$, $m_e = 0.26\,\mathrm{m^2KV^{-1}s^{-1}}$, $H_e^m = 0.26\,\mathrm{eV}$ respectively stand for the electron charge, the site UO_2 pattern concentration per unit volume, the electron and hole mobility (supposed to be equal), and the corresponding common migration enthalpy. For the reported graphs, the equivalent concentration of "electrons" coming from the impurities is $C_{dop} = 2.1 \times 10^{-4}$; the positive value indicates this is equivalent to a doping with the same amount of trivalent ions.

As noticed for the analysis of the deviation from stoichiometry, a model fitted on one type of measurement does not correctly reproduce another type: Garcia's model is the only fitted model to behave correctly in Figure 12a.

Neither the unshifted atomistic-based models (Figure 12c) nor the shifted ones (Figure 12d) behave correctly. In general, in the extrinsic region (i.e. in the plateau, supposed to mark the impurity concentration C_{dop}), the electron+hole concentration at high temperatures is much higher than measurements. This falls in line with the much higher value for the electron-hole formation energy found by Garcia (Figure 5).

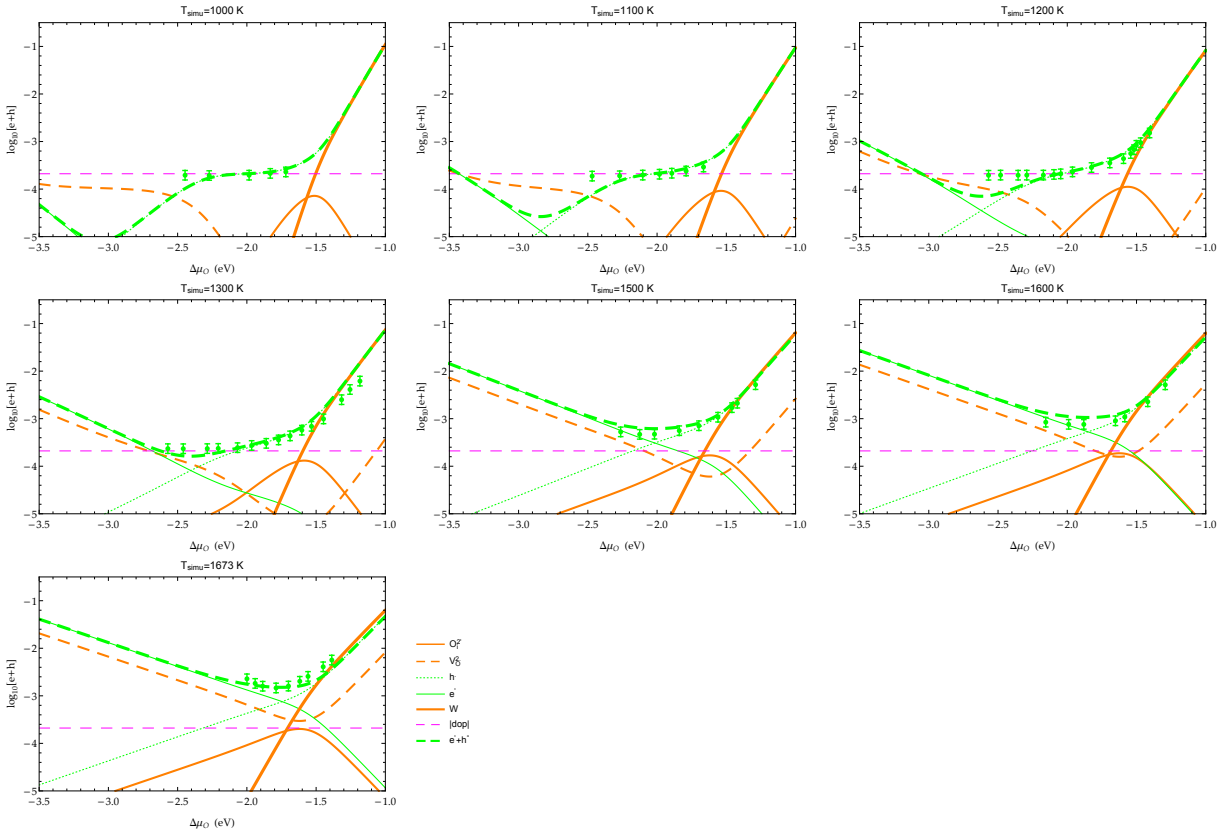

Figure 11: Defect concentrations in Garcia's model, experimental concentration of the electronic defects [46]

Both Vathonne's models behave however differently since their electron-hole formation energy are significantly higher than the other ones: the scatter with the experimental data is quite small at high temperature but increases below 1200 K. Finally, the shift in oxygen potential performed above on the basis of the stoichiometry deviation measurements tends to degrade the model quality concerning conductivity and unfortunately does not seem to be adapted to this physical quantity.

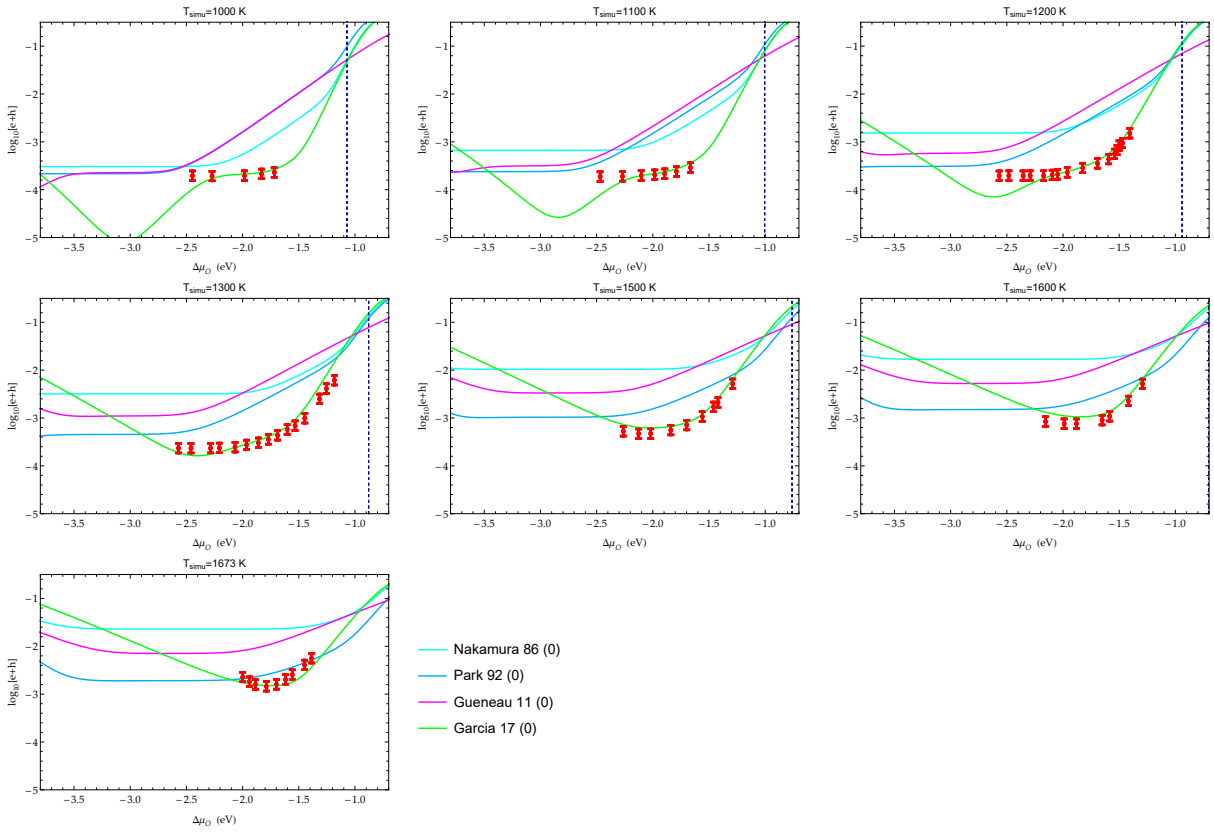

(a) fitted models

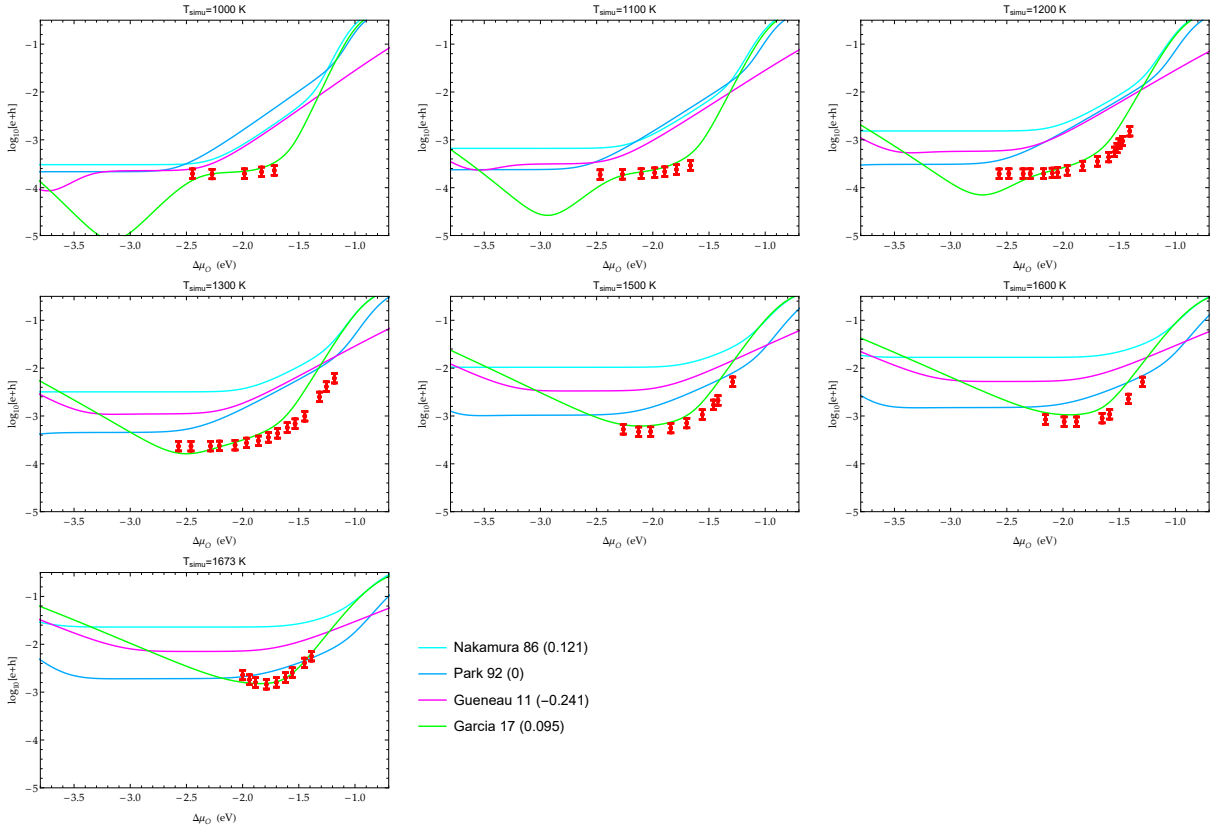

(b) shifted fitted models

Figure 12: Comparison of the models with experiments [46]: electronic defects concentration

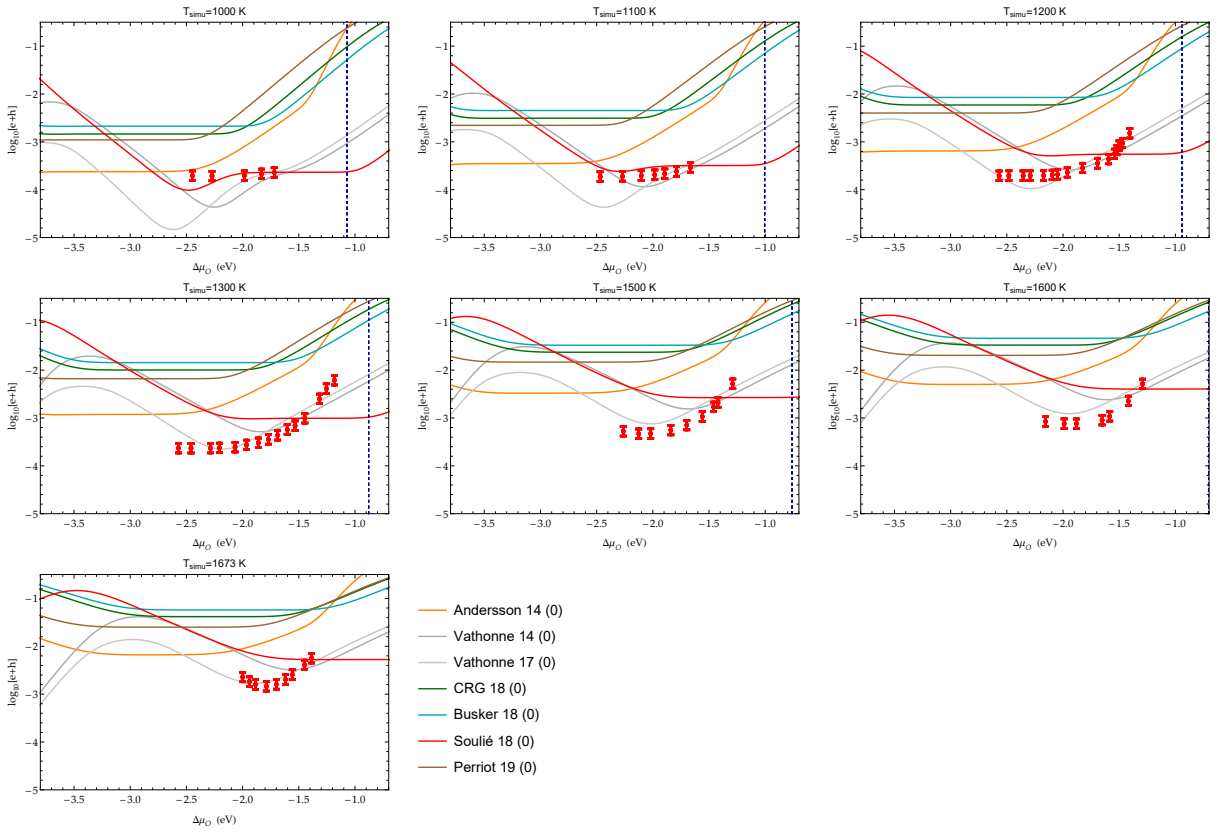

(c) atomistic-based models

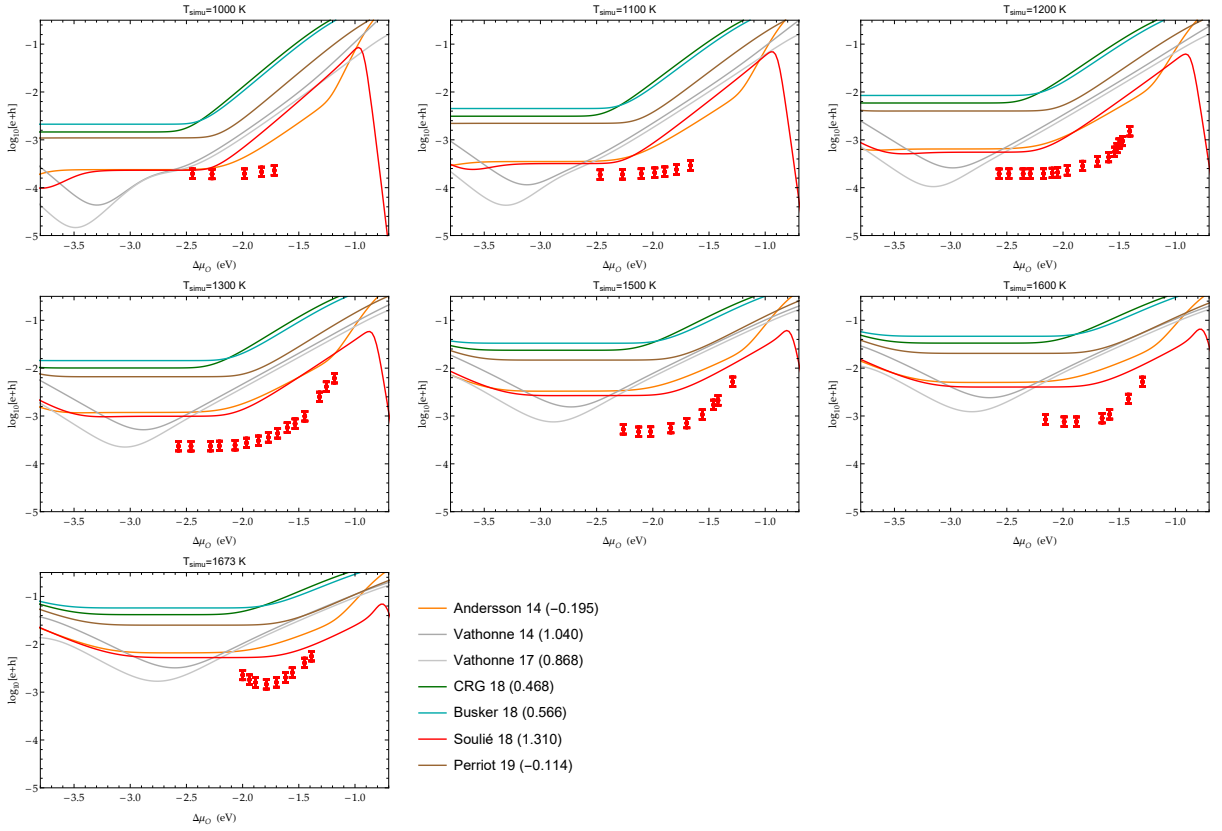

(d) shifted atomistic-based models

Figure 12: Continued...

4.5 Phase diagram

Eq. (15a), in conjunction with relevant phase-equilibrium equations, allow us to determine the phase limits between UO_{2+x}, and U or U_4O_9 respectively. For simplicity, oxygen solubility and defects in the two latter phases were neglected so that they were described as compounds.

The existence of the metal uranium phase imposes the U chemical potential. According to the thermodynamic reference for uranium, the equation set corresponding to U and UO_2 coexistence is written:

$$\begin{cases} \Delta\mu_U & = 0 \\ \Delta\mu_U + 2\Delta\mu_O & = \Delta g_{UO_2} + k_B T \ln(C_0) \end{cases} \tag{31}$$

In the same way, the formation equilibrium of U_4O_9 as a perfect compound is described in conjunction with UO_2:

$$\begin{cases} \Delta\mu_U + \frac{9}{4}\Delta\mu_O & = \Delta g_{UO_{9/4}} \\ \Delta\mu_U + 2\Delta\mu_O & = \Delta g_{UO_2} + k_B T \ln(C_0) \end{cases} \tag{32}$$

Since few if any models give evaluation of the formation enthalpy of U_4O_9 based on atomistic techniques, we chose for all the models to use the same experimental function of temperature $\Delta g_{UO_{9/4}}$, and took it from the TAF-ID and CODATA (at 0 K). To simplify, we also chose the TAF-ID/CODATA value for Δg_{UO_2} since it seems that few model calculate this data; additionally, the two calculated values at 0 K (Vathonne 14 and 17) are close to the experimental one. This means that, for a given temperature, the values of the oxygen relative chemical potential $\Delta\mu_O$ do not differ very much from one model to another, since they differ of the sum $k_B T \ln(1 - \sum_\nu C_\nu)$ which is generally small compared to other terms in Eqs. 32 and 31. For this reason, solving these equations devoid of this term yields a good approximation of the phase limits, this is why the corresponding lines are drawn in blue in the graphs $x(\Delta\mu_O, T)$, Figures 6-8, from which it is possible to determine the corresponding points in the phase diagram.

Solving Eqs. (15b) to (15g) with either (31) or (32) provides a complete description of the phase limits U/UO_{2+x} or UO_{2+x}/U_4O_9 as shown in the phase diagrams, T_{limit} vs O/M or x, Figures 13 and 14. The shifted models should not be addressed here, since the phase limits rely on the solid formation Gibbs energies Δg_{UO_2} and $\Delta g_{UO_{9/4}}$ which are to be shifted the same way as the defect Gibbs energies, which results in no change in the phase diagrams. However, we tested the shifted models using the somehow *ad hoc* assumption that Δg_{UO_2} and $\Delta g_{UO_{9/4}}$ alone are not affected by he shift.

It should be emphasized that for the phase diagrams, experimental data in the quasi-stoichiometric region is even scarcer and scattered than already noticed for the $x(\Delta\mu_O, T)$ graphs (Section 4.3) so that limited confidence can be granted to a comparison of simulations and measurements.

- There is only one measurement in the region $-0.02 < x < 0$, at $x = 0.01$.
- In the region $0 < x < 0.01$, the only data we found is from [23] (for which we chose an arbitrary uncertainty on x of 0.005). For $x > 0.01$, we could not find the uncertainties for the data supporting the TAF-ID and took them from [9] whose values (although not selected) are close to those selected for the TAF-ID.
- As shown Figure 14 the scarcity and uncertainty of data in the region $-0.01 < x < 0.01$ do not allow any conclusion on the quality of any model.

Specific comments can be made for the various models. As shows a comparison between the second and third graphs of Figure 14, the shift does significantly improve the phase limits calculations by most of the atomistic models. For this reason, we mostly comment on fitted and atomistic unshifted models.

- The very low (negative) values of the interstitial and di-interstitial formation energy of Park's model yield unrealistically high values of x at low temperatures in the hyper–stoichiometric region, preventing the phase limit to reach the $x = 0$ point above 300 K. This extreme behavior is enhanced at low temperature because of the (very) negative formation entropies of these defects.
- Our version of Guéneau's model yields a curve (Figure 14) practically superimposed to the TAF-ID curve for $-0.01 \leq x \leq 0.005$. For higher deviations from stoichiometry, the non-linear terms of the Gibbs TAF-ID energy, neglected in our model due to linearization, are no longer negligible, which probably induces the discrepancy in the graph between the corresponding curves. Close to the stoichiometry and for $x < 0$, Guéneau and the TAF-ID underestimate the experimental values of x. This seems to be also the case for $x > 0.01$. In the region $0 < x < 0.01$, the experimental data is too uncertain to allow a conclusion, as noticed above.

- In Garcia's model, $V_O^{2^\circ}$ has a low energy and a high entropy of formation, yielding a very low (negative) value of x in Figure 13a, in line with Figure 6 at 2100 K for instance.
- Andersson's model behaves quite satisfactory both in hypo- and hyper- stoichiometric regions, although the correct hyper-stoichiometric region seems to be much larger. Surprisingly, for $0.667 < {}^O/_M < 0.68$, the result is closer to the measurements than the TAF-ID.
- CRG behaves quite correctly for $0 < x < 0.03$.
- Similar comments stand for Perriot's model as for Park's, but in this case, it comes from the low formation energy of the uranium vacancy. The shifted version of this model behaves quite correctly on a large x range.

As a conclusion, let us remind that the linear approximation on which the models rely is theoretically valid in the narrow stoichiometric region (i.e. $|x| \lessapprox 0.01$). Despite this limitation, two models show a satisfying behavior both for the U_4O_9 and U limits: unshifted Andersson's model and shifted Perriot's, although to a lesser extent. For the lower temperatures of the phase diagram, close to the stoichiometry, the phase limits measurements are very scarce and difficult to obtain, so that the phase limits are not precisely characterized, nor the model validated; this calls for renewed experimental efforts both to confirm the existing data and to unambiguously characterize this region of high interest in the practical use of the material.

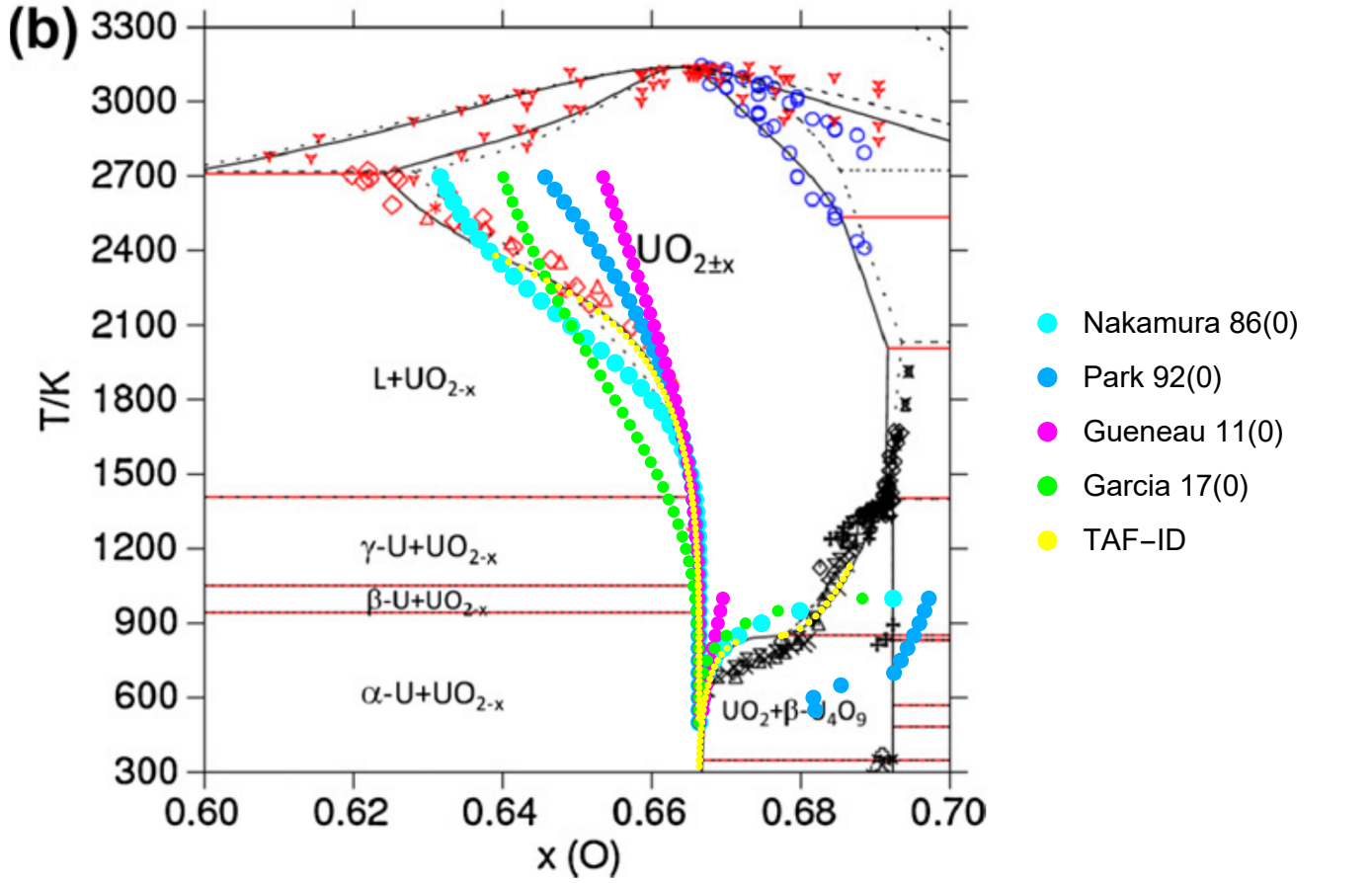

(a) fitted models

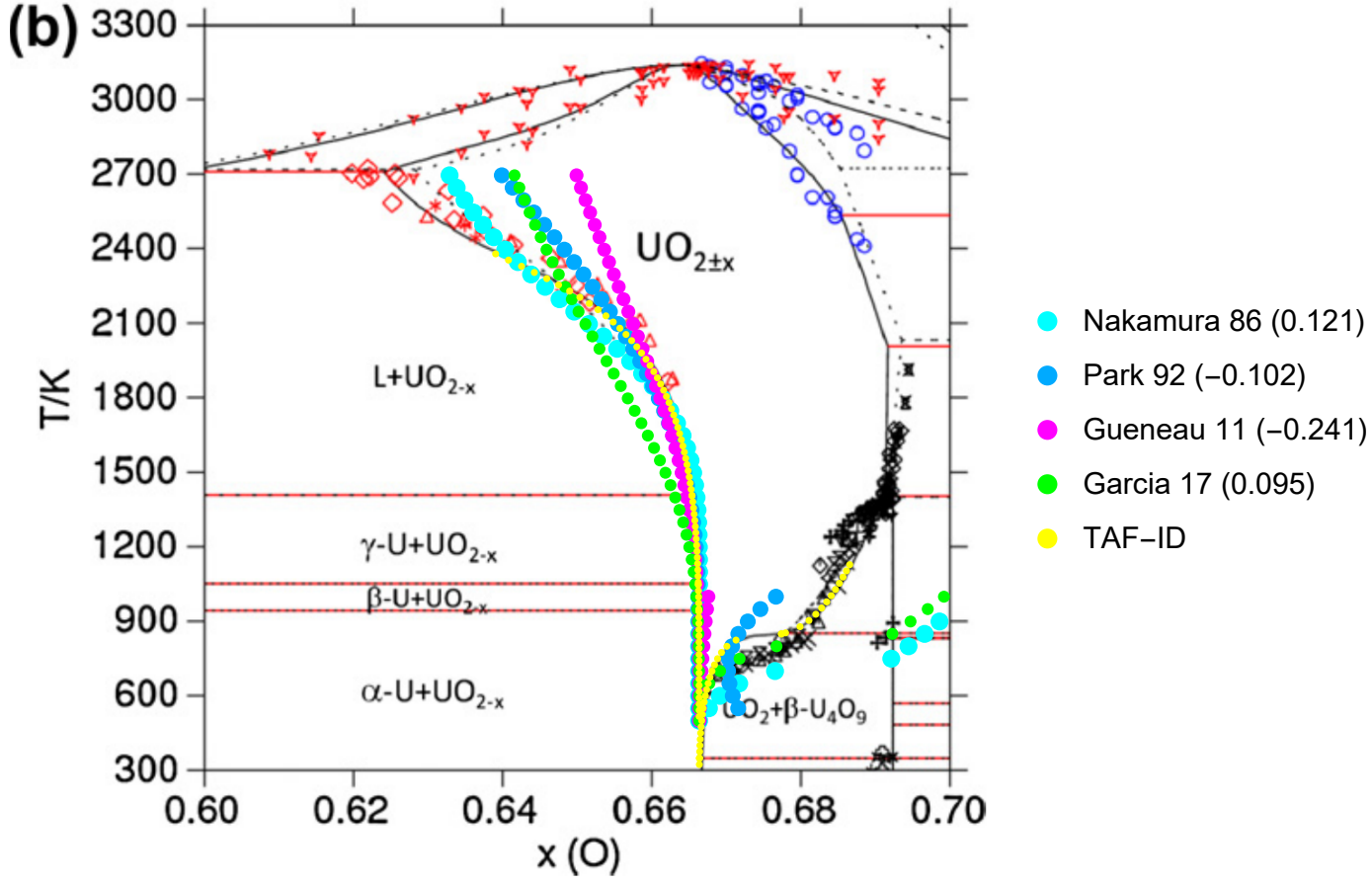

(b) shifted fitted models

Figure 13: Comparison of the fitted models with experiments [24, 25]: phase diagram ($T_{transition}$ vs $^{O}/_{M}$)

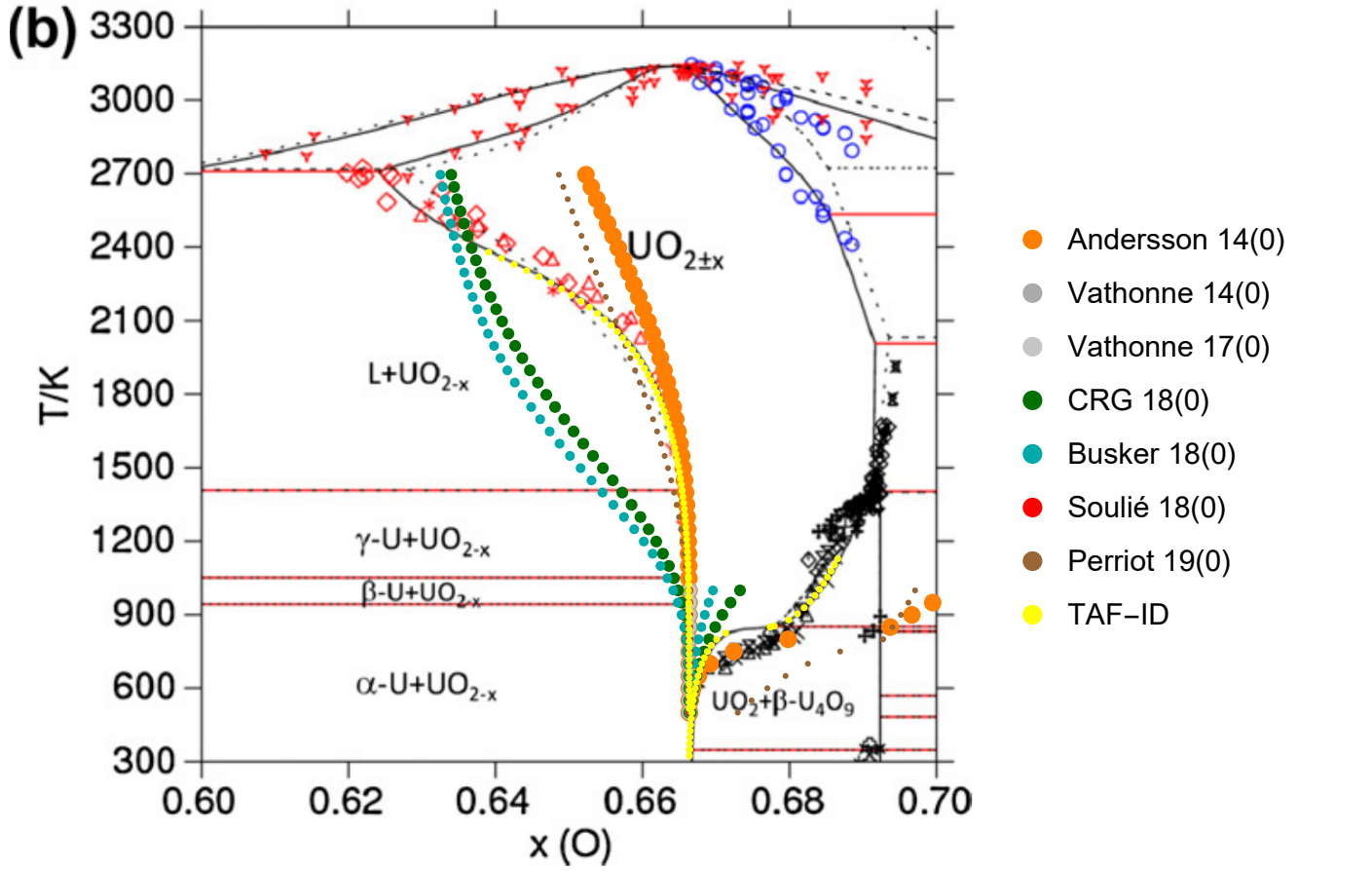

(c) atomistic-based models

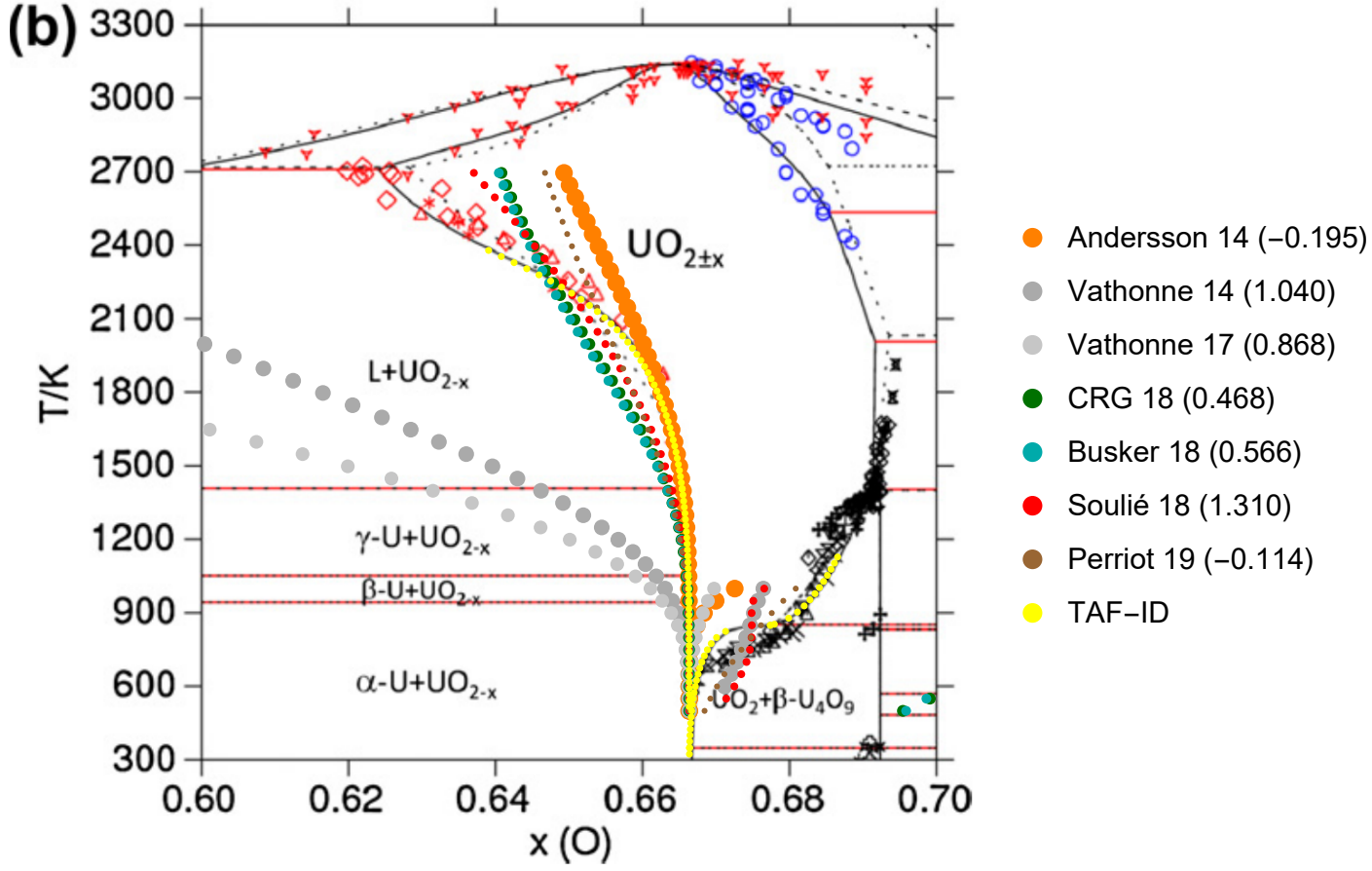

(d) shifted atomistic-based models

Figure 13: Continued...

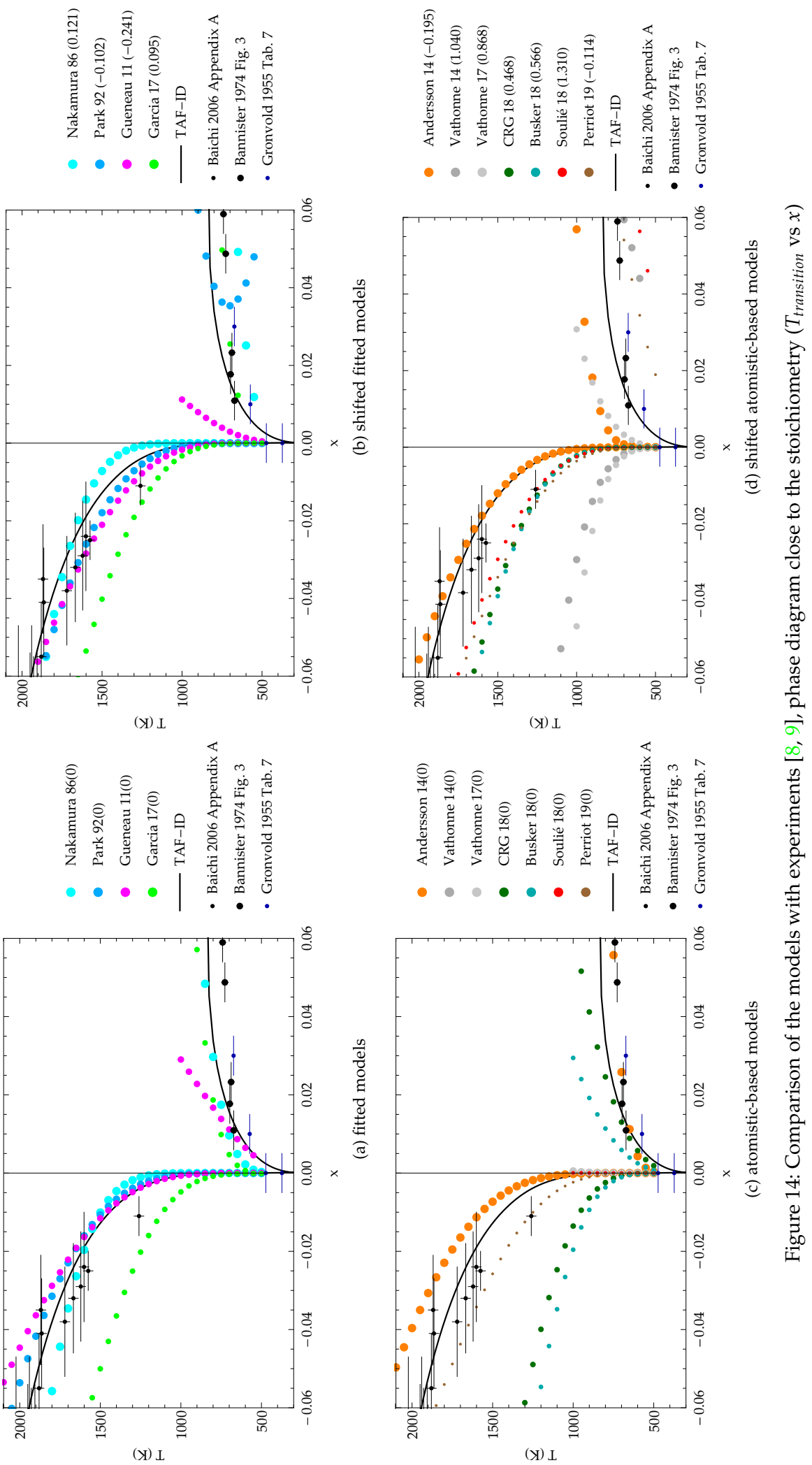

Figure 14: Comparison of the models with experiments [8, 9], phase diagram close to the stoichiometry ($T_{transition}$ vs x)

5 Discussion about DFT perspectives

In this paper, different sets of calculated data for the thermodynamic properties of UO_{2+x} have been presented and analyzed, with one of the observations being that, even though the sets represent similar trends, in many cases the absolute values for the predicted thermodynamic properties are quite different and those in closest agreement with experiments tend to rely on applying a correction scheme. Although the origins of the discrepancies between different atomistic methods and between methods and experiments have been discussed and at least partially rationalized, we would like to briefly reflect on a few of the outstanding issues and potential paths forward from a DFT perspective.

The oxidation and reduction energies of UO_2 vary significantly between, for example, LDA+U and GGA+U, where both deviate from known experimental data. Some of this discrepancy has already been correctly ascribed to the reference energy of an O_2 molecule, which is known to be overestimated by both GGA and LDA based on the measured binding energy, with an error of up to 1.2 eV per atom for LDA [31]. Applying a correction that accounts for the known error is straight-forward and makes oxidation more favorable in agreement with experiments, however there are still quantitative deviations that must originate from the description of the oxygen defects in the UO_2 lattice.

The present paper discusses how that may be addressed by adding further corrections based on known oxidation thermodynamics and even though a practical and useful approach, it undermines the goal of making first principles predictions. One assumption underlying essentially all GGA+U and LDA+U calculations for UO_{2+x} to date is that the U parameter does not change from that established for the stoichiometric compound. This is probably a pretty good approximation, nevertheless as we move from qualitative to quantitative requirements on the thermodynamic predictions even small changes could play a role. The oxidation/reduction energies are also influenced by assumptions regarding the crystal symmetry in the DFT calculations, i.e. whether the lattice is allowed to develop Jahn-Teller distortions or not, with the predictions based on a lattice with Jahn-Teller distortions being less favorable from an oxidation/reduction point of view, because the perfectly stoichiometric UO_2 benefits the most from this distortion [6]. Questions remain regarding the behavior of these distortions at finite temperature in the paramagnetic phase and the role they may play in quantitative predictions of thermodynamic properties. One additional cause of discrepancies versus experiments might be the way the magnetism of UO_2 itself is modeled, presenting important simplifications relatively to the experiments. Three issues can be distinguished.

- At 0 K the Jahn-Teller structure of UO_2 is a 3k antiferromagnet but it is often simplified as a collinear 1k antiferromagnetic model.
- At higher temperature, UO_2 has the fluorite structure and is paramagnetic. The energy calculations by DFT are done at 0 K but imposing the symmetries of the fluorite structure (which is known not to be true at this temperature).
- Additionally, in this fluorite imposed structure in temperature, the paramagnetic state is mimicked as a collinear antiferromagnetic state which is a strong approximation.

These approximations should at least be assessed in terms of impact on the material energy/entropy, and improved if necessary.

Other contributions to uncertainties of the predicted defect Gibbs energies come from the entropy evaluation. For the moment there seem to be no possibility to routinely evaluate the defect entropies with the same techniques (ab initio) as the energies, since this would require extensive phonon calculations that have so far been outside reach of DFT calculations. The current strategy is to use empirical potentials, even if they are known not to be particularly fitted to this physical quantity. For the same reasons anharmonicity and changes in the defect formation energies with temperature are not calculated yet in completely satisfactory way. Clearly, it would be desirable to improve the overall phonon ab initio calculation techniques, in order to correctly address the temperature effects on defect buildup.

The model heat of formation of UO_2 also exhibits deviation among each other, and also from experiments probably depending on how the reference states are treated [52]. In addition to the O_2 molecule discussed above, the neglect or inclusion of a Hubbard parameter for pure uranium metal and the approach taken to compare the energy of compounds using different U parameters has been debated in the literature and significantly impacts the predicted heat of formation. This originates from the fact that the thermophysical properties of uranium metal do not require a Hubbard U parameter for accurate modeling, while UO_2 does [11, 17]. In fact, some reports claim that uranium metal is better described without it. It is possible to choose a combination of U parameters for U metal and UO_2 that reproduces the experimental formation energy, but there is not yet a consensus whether comparing compounds with different U values is an accurate way

of obtaining heats of formation and other thermodynamic properties. The way to resolve this conundrum would be to use a methodology that does not rely on variable parameters like the Hubbard U or calculates the Hubbard U value self-consistently based on the local environment and bonding. The latter approach is available [30, 13, 1], but it has not been exercised on UO_{2+x} and it still suffers from questions regarding the validity of comparing energies for structures with different Hubbard U parameters. On the other hand, hybrid density functional theory methods are popular, because they fulfill this requirement and, as an added benefit, this methodology does an excellent job at describing the energy of an O_2 molecule [31], thus reducing the error to a few hundredths of an eV. Even though hybrid functionals have been used to study UO_2, the heat of formation has not yet been reported to the best of our knowledge. As has already been discussed, defect properties have been studied and, somewhat surprisingly, the calculated Frenkel and Schottky energies are predicted to be high compared to the LDA+U and GGA+U methods as well as compared to experimental estimates. Among the reasons for that, we should emphasize that metastable states also exist using hybrid functionals [29] and that no method exist to avoid convergence toward metastable states. Moreover, the computational time seems still too important for a use with the large supercells required for defects. Further studies are needed to fully assess the accuracy of the hybrid approach to model the UO_{2+x} thermodynamics.

The band gap or the electron-hole formation energy is a third thermodynamic quantity with observed uncertainty with respect to experiments. The reason for introducing advanced DFT methods capable of capturing the strongly correlated nature of the uranium 5f electrons was that the standard LDA and GGA schemes failed to capture the band gap and semi-conducting nature of UO_2, rather it was predicted to be a metal. The LDA+U and GGA+U approaches improve on this discrepancy and predict a band gap that is in decent agreement with experiments for the commonly used value of the Hubbard U parameter, as previously discussed in this paper. The lower values reported in [19, 23] is at least partially a consequence of studying the electron-hole pair explicitly in a supercell, which allows for the formation of polarons with lower energies than obtained from the pure band gap. Hybrid methods predict higher band gaps, but they are not obviously better than the LDA+U or GGA+U predictions compared to experiments. The magnitude of the band gap and the position of the occupied 5f states with respect to the O-2p dominated band just below the isolated 5f peak are very important quantities, not only because the electron-hole energies impact the thermodynamics, but also because their relative positions determine the change in energy upon oxidation and reduction as well as the balance between hyper-stoichiometry due to oxygen interstitials or uranium vacancies. We recommend future studies to pay close attention to this behavior as they try to resolve the remaining thermodynamic issues of the UO_{2+x} system from a first-principles perspective.

6 Conclusions

This paper develops a unified presentation of the thermodynamic parameters of eleven point-defect models in UO_2 (defect formation energies and entropies); four of them are fitted on experimental data, while the remaining seven are obtained through atomistic simulations. This allows us to compare all the models on the same basis both among themselves and with a large set of experimental data of various physical quantities. In particular, combining the defect thermodynamics and the TAF-ID functions for U and U_4O_9 phases makes it possible to compute the $U-O$ phase diagram in the vicinity of stoichiometric UO_2. As far as we know, this is a new application of such kind of data.

Several results are worth highlighting.

1. The formation energies and entropies are very scattered from one model to another, even among the *ab initio* values (energies at 0 K from Andersson, Vathonne, Cooper, Soulié and Perriot). As the techniques are similar in general, if not identical, one might *a priori* expect very similar results, which is not the case. Internal degrees of freedom of these computational techniques exist that might explain the observed scatter: for instance the occurrenced of nonphysical and undetected metastable states, the use of different energy functionals or crystallographic structures (accounting or not of the Jahn-Teller effect), the convergence criteria and the occupation matrix control procedure. The publications do not necessarily describe all these features in details, which complicates the analysis and comparisons of the results. Providing files of the DFT programs both for the input data and for the raw results would be highly helpful for a precise understanding of what calculations have actually been performed in a given publication, and to what extent they can be compared to other calculations.
2. The comparison of model results with experiments offers quite contrasted results. The VdW-DF exchange correlation functional allows a good estimation of the UO_2 formation energy at 0 K (Vathonne 17), while when available (CRG and Busker models), the bulk UO_2 heat capacities of the different models are rather close to the experimental values, when taking account for intrinsic defects formation (eletron-hole and oxygen Frenkel pairs). Conversely, the different values for the electron-hole Gibbs formation energy are very scattered. Moreover, they are far from the available gap measurements, especially at high temperatures, which triggers for a clarification concerning either what is actually measured or how the calculations can be improved. This discrepancy might explain the poor ability of some models to reproduce also other observations.
3. In general, and as expected, the fitted models behave favorably in interpolation conditions, i.e. when compared with the data sets according to which they were fitted. In this respect, Garcia's model, which was fitted to the conductivity measurements, correctly predicts this quantity while the other fitted models built on the stoichiometry deviation measurements do not, and vice versa.
4. For the atomistic-based models, the comparison of the deviation from stoichiometry as a function of the oxygen potential and the temperature with experimental data is quite good for Andersson's model, although a small systematic deviation occurs at low temperature and high hyper-stoichiometry. The other atomistic models do not compare favorably in this way unless the oxygen molecule energy at 0 K is shifted, sometimes of more than one eV, to minimize the variance of the difference between measured and simulated oxygen potentials. After this energy shift, Andersson's model behaves well or very well on the whole temperature/stoichiometry range; Soulié's model behaves well at high temperature and in acceptable way otherwise.
5. Based on the atomistic defect Gibbs formation energy and on the experimental formation energies of the perfect oxides (UO_2 and U_4O_9), "semi atomistic" phase diagrams could be drawn. The better atomistic-based model is Andersson's for this issue as well, but surprisingly not the shifted version. However, one should not draw too many conclusions concerning the phase diagrams, since unless at very low temperature (where few if any validation data is available), the deviation from the stoichiometry is quite high and presumably out of the normal scope of the models that rely upon the dilution limit.
6. Large shifts in the energy of the O_2 molecule are necessary to improve the agreement of the simulations with the measurements of x and μ_O; in the same way, a similar shift is usually necessary for a good agreement with the formation energy of various oxides. Unfortunately, for any given model, both procedures do not lead to the same shift in energy. This points out that the poor evaluation of O_2 energy in ab initio explains probably only a part of the errors in the defect energy computation. This urges for a strong action at least circumventing the role of this parameter among the other ones in the defect formation energies.

From these results, we can suggest a few additional prospects and requirements for the further development of atomistic-based defect models.

1. In this application, the thermodynamic references of the atomistic models, when clarified, appeared different from one model to another, and some basic information was lacking in such a way that it had to be extracted from the publications through *ad hoc* procedures. It thus appears advisable to choose a standard thermodynamic convention in which the thermodynamic parameters of all the models are expressed. The standard used in this paper is based on three figures for each defect that proved sufficient for our applications: energy and entropy at 900 K and a constant approximation of the heat capacity.
2. Additionally, large discrepancies exist among atomistic values given by different teams, although they should be equal. The fact that some of them were neither noticed nor explained in the publications might result from the absence of a standard method for presenting the thermodynamic parameters. At the least, using a standard presentation would probably facilitate both the future use of atomistic-based thermodynamic functions as well as their comparison with previous atomistic results and with experiments, which will contribute to establish the ability of the atomistic techniques for modeling the defect thermodynamics of actinide compounds.
3. The oxygen molecule energy calculation still raises questions, notably concerning the strategies, or absence thereof, adopted by the various authors to address the issue. As this energy is clearly of prime importance for characterizing the material's exchange with the environment, an exact *ab initio* evaluation of the oxygen molecule energy should be undertaken, possibly leading to use other *ab initio* techniques. This would in particular help delineate the effort to be devoted specifically for the solid modeling improvement. Failing that, should calculations keep being circumvented by fittings, it seems reasonable to expect a unique convention in calibrating the oxygen energy at 0 K, perhaps using the oxidation of UO_2 into U_4O_9 which proved quite efficient in Andersson's model. In such cases, the atomistic energies for the reactants/products of this reaction should be published as is the case for the defect thermodynamic parameters. Along the same lines, building a $U-O$ phase diagram completely relying upon atomistic calculations in the vicinity of UO_2 now appears within reach, provided that the thermodynamic functions for at least U^{solid}, UO_2^{liquid} and $U_4O_9^{solid}$ are calculated by atomistic techniques.
4. Using alternative ab initio techniques, for instance hybrid density functional theory, might be a way to solve various issues concerning the calculation of important thermodynamic defect quantities, such as oxygen molecule energy, band gap or oxide formation energy. Assessing and, if necessary, improving these methods would be very interesting.
5. The comparison of the model results with the experiments shows good agreement in too few situations. This flaw might originate either from inconsistency in the experimental data or from limits in the atomistic calculations. Progress on both sides would be very valuable.
   - On the experimental side, several aspects could be improved:
     a) Since no model could reproduce the experimental results of more than one type of measurement at a time, one may ask whether the problem occurs form the model design or from the consistency of the experimental techniques or samples. It would thus be very useful to perform all the available characterization techniques on each UO_2 sample *in the same test campaign* and perform the corresponding calculations in order to validate the models according to as many as possible consistent physical quantities. Similarly, obtaining measurements of x and μ_O *both* below and above the stoichiometry at given temperatures would be very helpful.
     b) The type of defect model presented here is expected to best behave close to stoichiometry. Moreover, this region contains the initial in-pile duty point of the fuel. Unfortunately, the experimental data in this region is scarce and inaccurate, and the TAF-ID model does not fit them sharply. Increasing the corresponding availability and precision of observations and reconsidering the Calphad model fitting would thus largely contribute to improving the fitted models and the validation process of the atomistic models. In this region, the impurities have the largest impact since the defect concentrations are the lowest and the deviation from stoichiometry is the most difficult to measure (especially at lower temperatures). Using samples of high purity and exploring higher temperatures would hopefully reduce the impurity influence and increase the precision of the measurements.
     c) There are few if any conductivity measurements for hypo-stoichiometric UO_2, which pre-

vents us from directly evaluating electron mobility (which is supposed to be equal to that of the hole). Producing such data would notably improve the efficiency of conductivity as a way to investigate defect thermodynamics.

d) The models CGR, Busker, Soulié and Perriot are predicting a deviation from the stoichiometry controlled by the uranium vacancies in the close hyper-stoichiometric region. This very unexpected result obtained from independent studies deserve special consideration and should be carefully assessed by dedicated experiments.

- On the modeling side, several issues could be addressed to improve the prediction skills of the models.

a) The energies and entropies of electrons and holes are sometimes unknown, in which case they need to be calculated.

b) Some models do not account for uranium vacancies, nor aggregates of oxygen vacancies or interstitials. Considering these defects should extend the ability of these models to cover larger deviations from stoichiometry at low temperature.

c) To date, the defect entropies cannot be calculated with the same tool as the energies because the required intensive *ab initio* calculation of faulted supercells are not yet possible. To our knowledge, it is not possible to fit the empirical potentials used for the entropies on the *ab initio* values at 0 K of the defect formation energies. This means the empirical values of the entropies may differ from what the *ab initio* calculation would yield if it were possible. Moreover, the discrepancies of calculated entropies with respect to the measurements are considerable. Therefore, it seems very important to make efforts in improving the consistency of the calculated defect entropies with the results of *ab initio* calculations. Similarly, in a longer-term perspective, *ab initio* techniques should be improved to calculate anharmonic effects occurring at high temperature.

d) No calculated Gibbs energy of formation for U_4O_9 was available, which did not allow a purely ab initio prediction of the phase diagram. Overcoming this limitation would be of great use.

6. *Ab initio* techniques are expected to provide a cost-effective way to study complex systems derived from UO_2, even comprising a proportion of other actinides such as *Pu* or *Am*. In our opinion, it will be difficult to build confidence in the results of such studies unless significant efforts are made to compare the different models both among themselves and with experimental results, first using the "simple" UO_2 system before using the complex systems.

Acknowledgments

This work was funded by CEA within the project "basic research for fuel materials" (RCOMB). The author is grateful to J. Léchelle and C. Riglet-Martial for fruitful discussions, data and insights concerning the Calphad method and to C. Guéneau and G. Jomard for their discussions of the results and appropriate suggestions.

Bibliography

[1] Amadon, B., Applencourt, T., and Bruneval, F. (2014). Screened Coulomb interaction calculations: cRPA implementation and applications to dynamical screening and self-consistency in uranium dioxide and cerium. *Physical Review B*, 89(12):125110.

[2] Andersson, D. A., Baldinozzi, G., Desgranges, L., Conradson, D. R., and Conradson, S. D. (2013). Density functional theory calculations of UO_2 oxidation: Evolution of UO_{2+x}, U_4O_{9-y}, U_3O_7, and U_3O_8. *Inorganic Chemistry*, 52(5):2769–2778.

[3] Andersson, D. A., Garcia, P., Liu, X. Y., Pastore, G., Tonks, M., Millett, P., Dorado, B., Gaston, D. R., Andrs, D., Williamson, R. L., Martineau, R. C., Uberuaga, B. P., and Stanek, C. R. (2014). Atomistic modeling of intrinsic and radiation-enhanced fission gas (Xe) diffusion in $UO_{2\pm x}$: Implications for nuclear fuel performance modeling. *Journal of Nuclear Materials*, 451(1-3):225–242.

[4] Andersson, D. A., Lezama, J., Uberuaga, B. P., Deo, C., and Conradson, S. D. (2009). Cooperativity among defect sites in AO_{2+x} and A_4O_9 ($A = \mathrm{U, Np, Pu}$): Density functional calculations. *Physical Review B*, 79(2):024110.

[5] Andersson, D. A., Simak, S. I., Johansson, B., Abrikosov, I. A., and Skorodumova, N. V. (2007). Modeling of CeO_2, Ce_2O_3, and CeO_{2-x} in the LDA + U formalism. *Physical Review B*, 75(3):035109.

[6] Andersson, D. A., Uberuaga, B. P., Nerikar, P. V., Unal, C., and Stanek, C. R. (2011). U and Xe transport in $UO_{2\pm x}$: Density functional theory calculations. *Physical Review B*, 84:054105.

[7] Baichi, M. (2001). *Contribution à l'étude du corium d'un réacteur nucléaire accidenté : aspects puissance résiduelle et thermodynamique des systèmes U-UO_2 et UO_2-ZrO_2*. PhD thesis, INP Grenoble.

[8] Baichi, M., Chatillon, C., Ducros, G., and Froment, K. (2006). Thermodynamics of the O-U system. IV - Critical assessment of chemical potentials in the U-$UO_{2.01}$ composition range. *Journal of Nuclear Materials*, 349(1-2):17–56.

[9] Bannister, M. J. and Buykx, W. J. (1975). A dilatometric study of the solubility of U_4O_9 in UO_2. *Journal of Nuclear Materials*, 55(3):345–351.

[10] Basak, C., Sengupta, A., and Kamath, H. (2003). Classical molecular dynamics simulation of UO_2 to predict thermophysical properties. *Journal of Alloys and Compounds*, 360(1-2):210–216.

[11] Bouchet, J. and Bottin, F. (2017). High-temperature and high-pressure phase transitions in uranium. *Physical Review B*, 95(5):054113.

[12] Bruneval, F., Freyss, M., and Crocombette, J.-P. (2018). Lattice constant in nonstoichiometric uranium dioxide from first principles. *Physical Review Materials*, 2(2):023801.

[13] Cococcioni, M. and de Gironcoli, S. (2005). Linear response approach to the calculation of the effective interaction parameters in the LDA+*U* method. *Physical Review B*, 71(3):035105.

[14] Cooper, M., Murphy, S., and Andersson, D. (2018). The defect chemistry of $UO_{2\pm x}$ from atomistic simulations. *Journal of Nuclear Materials*, 504:251–260.

[15] Cooper, M. W. D., Rushton, M. J. D., and Grimes, R. W. (2014). A many-body potential approach to modelling the thermomechanical properties of actinide oxides. *Journal of Physics: Condensed Matter*, 26(10):105401.

[16] Cox, J. D., Wagman, D. D., and Medvedev, V. A. (1989). *CODATA key values for thermodynamics*. Hemisphere Pub. Corp., New York. OCLC: 18559968.

[17] Dewaele, A., Bouchet, J., Occelli, F., Hanfland, M., and Garbarino, G. (2013). Refinement of the equation of state of α-uranium. *Physical Review B*, 88(13):134202.

[18] Dorado, B., Andersson, D. A., Stanek, C. R., Bertolus, M., Uberuaga, B. P., Martin, G., Freyss, M., and Garcia, P. (2012). First-principles calculations of uranium diffusion in uranium dioxide. *Physical Review B*, 86(3):035110.

[19] Fink, J. K. (2000). Thermophysical properties of uranium dioxide. *Journal of Nuclear Materials*, 279(1):1–18.

[20] Finnis, M. W., Lozovoi, A. Y., and Alavi, A. (2005). The oxidation of NiAl: What can we learn from ab initio calculations? In *Annual Review of Materials Research*, volume 35, pages 167–207.

[21] Garcia, P., Pizzi, E., Dorado, B., Andersson, D., Crocombette, J.-P., Martial, C., Baldinozzi, G., Siméone, D., Maillard, S., and Martin, G. (2017). A defect model for UO_{2+x} based on electrical conductivity and deviation from stoichiometry measurements. *Journal of Nuclear Materials*, 494(Supplement C):461–472.

[22] Griesmeyer, J. and Ghoniem, N. (1979). The response of fission gas bubbles to the dynamic behavior of point defects. *Journal of Nuclear Materials*, 80(1):88–101.

[23] Grønvold, F. (1955). High-temperature X-ray study of uranium oxides in the UO_2-U_3O_8 region. *Journal of Inorganic and Nuclear Chemistry*, 1(6):357–370.

[24] Guéneau, C., Baichi, M., Labroche, D., Chatillon, C., and Sundman, B. (2002). Thermodynamic assessment of the uranium-oxygen system. *Journal of Nuclear Materials*, 304(2-3):161–175.

[25] Guéneau, C., Dupin, N., Sundman, B., Martial, C., Dumas, J.-C., Gossé, S., Chatain, S., De Bruycker, F., Manara, D., and Konings, R. (2011). Thermodynamic modelling of advanced oxide and carbide nuclear fuels: Description of the U–Pu–O–C systems. *Journal of Nuclear Materials*, 419(1–3):145–167.

[26] Howard and Lidiard (1964). Matter transport in solids. *Report on progress in physics*, 27:161.

[27] Hyland, G. J. and Ralph, J. (1983). Electronic contributions to the high-temperature thermophysical properties of $UO_2 + x$: a critical analysis Gerard J Hyland, Jeffrey Ralph. *High temperature high pressure*, 15:179–190.

[28] Jackson, R. A., Murray, A. D., Harding, J. H., and Catlow, C. R. A. (1986). The calculation of defect parameters in UO_2. *Philosophical Magazine A*, 53(1):27–50.

[29] Jollet, F., Jomard, G., Amadon, B., Crocombette, J. P., and Torumba, D. (2009). Hybrid functional for correlated electrons in the projector augmented-wave formalism: Study of multiple minima for actinide oxides. *Physical Review B*, 80(23):235109.

[30] Kulik, H. J., Cococcioni, M., Scherlis, D. A., and Marzari, N. (2006). Density Functional Theory in Transition-Metal Chemistry: A Self-Consistent Hubbard U Approach. *Physical Review Letters*, 97(10):103001.

[31] Kurth, S., Perdew, J. P., and Blaha, P. (1999). Molecular and solid-state tests of density functional approximations: LSD, GGAs, and meta-GGAs. *International Journal of Quantum Chemistry*, 75(4-5):889–909.

[32] Labroche, D. (2000). *Contribution à l'étude thermodynamique du système U-Fe-O*. PhD thesis, INP Grenoble.

[33] Labroche, D., Dugne, O., and Chatillon, C. (2003). Thermodynamics of the O-U system. I - Oxygen chemical potential critical assessment in the UO_2-U_3O_8 composition range. *Journal of Nuclear Materials*, 312(1):21–49.

[34] Lindemer, T. and Besmann, T. (1985). Chemical thermodynamic representation of $UO_{2\pm x}$. *Journal of Nuclear Materials*, 130:473–488.

[35] Mayer, J., Elsässer, C., and Fähnle, M. (1995). Concentrations of Atomic Defects in $B_2Fe_xAl_{1-x}$. An Ab-Initio Study. *physica status solidi (b)*, 191(2):283–298.

[36] Mayer, J. and Fähnle, M. (1997). On the meaning of effective formation energies, entropies and volumes for atomic defects in ordered compounds. *Acta Materialia*, 45(5):2207–2211.

[37] Nakamura, A. and Fujino, T. (1986). Thermodynamic analysis on point defects of UO_{2+x} at relatively small deviation from stoichiometry between 600 and 1400°C. *Journal of Nuclear Materials*, 140(2):113–130.

[38] Nakamura, A. and Fujino, T. (1987). Thermodynamic study of UO_{2+x} by solid state emf technique. *Journal of Nuclear Materials*, 149(1):80–100.

[39] OECD. NEA Nuclear Science Committee - Thermodynamics of Advanced Fuels – International Database (TAF-ID).

[40] Oxford, G. A. E. and Chaka, A. M. (2011). First-Principles Calculations of Clean, Oxidized, and Reduced β-MnO_2 Surfaces. *The Journal of Physical Chemistry C*, 115(34):16992–17008.

[41] Park and Olander (1990). A defect model for the oxygen potential of urania. *High Temperature Science*, 29:203.

[42] Park, K. and Olander, D. (1992). Defect models for the oxygen potentials of gadolinium-and europium-doped urania. *Journal of Nuclear Materials*, 187(1):89–96.

[43] Perriot, R., Matthews, C., Cooper, M. W. D., Uberuaga, B. P., Stanek, C. R., and Andersson, D. A. (2019). Atomistic modeling of out-of-pile xenon diffusion by vacancy clusters in UO2. *Journal of Nuclear Materials*, 520:96–109.

[44] Ruello, P. (2001). *Etude du changement de comportement du dioxyde d'uranium au voisinage de 1300 K : Propriétés électriques, optiques et structurales*. PhD thesis, Ecole Centrale des Arts et Manufactures (Ecole Centrale Paris).

[45] Ruello, P., Becker, K. D., Ullrich, K., Desgranges, L., Petot, C., and Petot-Ervas, G. (2004). Thermal variation of the optical absorption of UO_2: determination of the small polaron self-energy. *Journal of Nuclear Materials*, 328(1):46–54.

[46] Ruello, P., Petot-Ervas, G., Petot, C., and Desgranges, L. (2005). Electrical Conductivity and Thermoelectric Power of Uranium Dioxide. *Journal of the American Ceramic Society*, 88(3):604–611.

[47] Rushton, M., Stanek, C. R., Cleave, A. R., Uberuaga, B. P., Sickafus, K. E., and Grimes, R. W. (2007). Simulation of defects and defect processes in fluorite and fluorite related oxides: Implications for radiation tolerance. *Nuclear Instruments and Methods in Physics Research Section B: Beam Interactions with Materials and Atoms*, 255(1):151–157.

[48] Skorek, R. (2013). *Étude par Dynamique d'Amas de l'influence des défauts d'irradiation sur la migration des gaz de fission dans le dioxyde d'uranium*. PhD Thesis, Univ. Aix-Marseille.

[49] Soulié, A., Bruneval, F., Marinica, M.-C., Murphy, S., and Crocombette, J.-P. (2018). Influence of vibrational entropy on the concentrations of oxygen interstitial clusters and uranium vacancies in nonstoichiometric UO_2. *Physical Review Materials*, 2(8):083607.

[50] Sundman, B. and Ågren, J. (1981). A regular solution model for phases with several components and sublattices, suitable for computer applications. *Journal of Physics and Chemistry of Solids*, 42(4):297–301.

[51] Vathonne, E. (2014). *Étude par calcul de structure électronique des dégâts d'irradiation dans le combustible nucléaire UO_2 : comportement des défauts ponctuels et gaz de fission*. PhD Thesis, Univ. Aix-Marseille.

[52] Vathonne, E., Andersson, D. A., Freyss, M., Perriot, R., Cooper, M. W. D., Stanek, C. R., and Bertolus, M. (2017). Determination of Krypton Diffusion Coefficients in Uranium Dioxide Using Atomic Scale Calculations. *Inorganic Chemistry*, 56(1):125–137.

[53] Vathonne, E., Wiktor, J., Freyss, M., Jomard, G., and Bertolus, M. (2014). DFT + U investigation of charged point defects and clusters in UO_2. *Journal of Physics: Condensed Matter*, 26(32):325501.

[54] Wang, L., Maxisch, T., and Ceder, G. (2006). Oxidation energies of transition metal oxides within the GGA+U framework. *Physical Review B*, 73(19):195107.

[55] Wiktor, J., Vathonne, E., Freyss, M., Jomard, G., and Bertolus, M. (2014). Calculation of defect formation energies in UO_2. In *Symposium EE/ZZ – Advanced Materials in Extreme Environments*, volume 1645 of *MRS Online Proceedings Library*.

Appendix

$$
\begin{aligned}
G^{MOX}_{(U^{5+})(O^{2-})(Va)} &= G^{MOX}_{(U^{4+})(O^{2-})(Va)} + \Delta G^{MOX}_{(U^{5+})(O^{2-})(Va)} \\
G^{MOX}_{(U^{4+})(Va)(Va)} &= G^{MOX}_{(U^{4+})(O^{2-})(Va)} - 2G_{O,\text{gas}} + \Delta G^{MOX}_{(U^{4+})(Va)(Va)} \\
G^{MOX}_{(U^{3+})(O^{2-})(Va)} &= G^{MOX}_{(U^{4+})(O^{2-})(Va)} + G^{MOX}_{(U^{3+})(Va)(Va)} - G^{MOX}_{(U^{4+})(Va)(Va)} \\
G^{MOX}_{(U^{3+})(Va)(Va)} &= G^{MOX}_{(U^{4+})(O^{2-})(Va)} - 2G_{O,\text{gas}} + \Delta G^{MOX}_{(U^{3+})(Va)(Va)} \\
G^{MOX}_{(U^{4+})(O^{2-})(O^{2-})} &= G^{MOX}_{(U^{4+})(O^{2-})(Va)} + G_{O,\text{gas}} \\
\Delta g^{0}_{UO_2} &= G^{MOX}_{(U^{4+})(O^{2-})(Va)} - 2G_{O,gas} - G_{U\alpha} \\
\Delta G^{MOX}_{(U^{5+})(O^{2-})(Va)} &= -0.604772 + 5.46509\, k_B T \\
\Delta G^{MOX}_{(U^{4+})(Va)(Va)} &= 5.65071 \\
\Delta G^{MOX}_{(U^{3+})(Va)(Va)} &= 7.74343 - 7.3216\, k_B T \\
L^{a}_{(U^{3+},U^{4+})(O^{2-})(Va)} &= 0.41596 \\
L^{b}_{(U^{3+},U^{4+})(O^{2-})(Va)} &= 0.01116
\end{aligned}
$$

$$
G_{O,gas} = \begin{cases}
-0.0449913 & T = 0 \\
-0.03608 - 0.00026432\,T - 5.2846\times10^{-8}\,T^2 + 6.8560\times10^{-12}\,T^3 - \frac{0.397625}{T} - 0.000115416\,T\ln(T) & 298 \le T \le 1000 \\
-0.06808 + 0.00013121\,T - 6.1750\times10^{-9}\,T^2 + 7.0280\times10^{-14}\,T^3 + \frac{2.72482}{T} - 0.00017426\,T\ln(T) & 1000 < T \le 3300 \\
-0.14500 + 0.000323983\,T - 4.4073\times10^{-9}\,T^2 + 1.1112\times10^{-13}\,T^3 + \frac{45.4287}{T} - 0.00019644\,T\ln(T) & 3300 < T
\end{cases}
$$

$$
G_{U\alpha} = \begin{cases}
-0.0659582 & T = 0 \\
-0.08714 - 4.5873\times10^{-11}\,T^3 + 1.2972\times10^{-8}\,T^2 + 0.00135725\,T + \frac{0.399729}{T} - 0.000278987\,T\ln(T) & 298 \le T \le 955 \\
-0.233422 + 0.00302762\,T - 0.000504325\,T\ln(T) & 955 < T \le 3000
\end{cases}
$$

$$
G_{U\gamma} = \begin{cases}
-0.0078019 + 1.003165\times10^{-11}\,T^3 - 8.6603\times10^{-8}\,T^2 + 0.0013633\,T + \frac{2.12064}{T} - 0.00028517\,T\ln(T) & 298 \le T \le 1049 \\
-0.04870 - 0.002101\,T - 0.0003968\,T\ln(T) & 1049 < T < 3000
\end{cases}
$$

$$
G_{UO_2} = \begin{cases}
-11.36214 & T = 0 \\
-11.597 - 2.10743\times10^{-11}T^3 + 1.05409\times10^{-7}T^2 + 0.00574186\,T + \frac{11.3082}{T} - 9.66655\times10^{-4}T\,\ln(T) & 298 \le T
\end{cases}
$$

$$
G_{UO_{9/4}} = \begin{cases}
-11.8278 & T = 0 \\
-11.9742 - 8.06602\times10^{-8}T^2 + 0.0046298\,T + \frac{4.51175}{T} - 0.000806364\,T\,\ln(T) & 298 \le T
\end{cases}
$$

Table 5: Thermodynamic functions used for the determination of the component chemical potentials and Calphad model for UO_2.

They were extracted from the TAF-ID [39] database and CODATA [16] database (for data at 0K). The temperatures are in K and the energies in eV.

	e (eV) (0K)	e (eV) (900K)	$\frac{s}{k_B}$ (900K)	$\frac{c}{k_B}$(T K)
h°	0	0	0	0
$e^{'}$	1.71	1.71	0	0
$O_i^{2'}$	1.57	1.67	-4.63	0.74
$O_i^{'}$	1.11	1.21	-4.63	0.74
O_i	0.80	0.90	-4.63	0.74
O_i°	0.68	0.78	-4.63	0.74
V_O	5.38	5.28	11.77	-0.72
V_O°	3.95	3.85	11.77	-0.72
$V_O^{2\circ}$	2.74	2.63	11.77	-0.72
$O_{i_2}^{4'}$	3.29	3.47	-8.76	1.43
$O_{i_2}^{3'}$	2.54	2.73	-8.76	1.43
$O_{i_2}^{2'}$	2.02	2.20	-8.76	1.43
$O_{i_2}^{'}$	1.31	1.50	-8.76	1.43
O_{i_2}	1.19	1.38	-8.76	1.43
$O_{i_4}^{\circ}$	-0.26	0.13	-17.88	2.84
O_{i_4}	-0.13	0.25	-17.88	2.84
$O_{i_4}^{'}$	0.26	0.64	-17.88	2.84
$O_{i_4}^{2'}$	1.02	1.40	-17.88	2.84
$O_{i_4}^{3'}$	1.66	2.04	-17.88	2.84
$O_{i_4}^{4'}$	3.10	3.48	-17.88	2.84
$O_{i_4}^{5'}$	4.44	4.82	-17.88	2.84
$V_U^{'}$	10.69	10.17	-4.57	-8.31
$V_U^{2'}$	11.10	10.58	-4.57	-8.31
$V_U^{3'}$	11.24	10.72	-4.57	-8.31
$V_U^{4'}$	11.50	10.98	-4.57	-8.31

Table 6: Complete thermodynamic dataset of Soulié's genuine model [12, 49].

Defect	Vathonne 14	Vathonne 17
$(V_{O_4}V_{U_2})^{2\circ}$		28.49
$(V_{O_4}V_{U_2})^{\circ}$		28.33
$(V_{O_4}V_{U_2})^{x}$	25.60	28.15
$(V_{O_4}V_{U_2})^{'}$	26.60	29.31
$(V_{O_4}V_{U_2})^{2'}$	27.74	30.56
$(V_{O_4}V_{U_2})^{3'}$		32.14
$(V_{O_4}V_{U_2})^{4'}$	30.71	33.71
$(V_{O_2}V_{U_2})^{2\circ}$		23.93
$(V_{O_2}V_{U_2})^{\circ}$		24.49
$(V_{O_2}V_{U_2})^{x}$		23.47
$(V_{O_2}V_{U_2})^{'}$		23.37
$(V_{O_2}V_{U_2})^{2'}$	21.24	23.65
$(V_{O_2}V_{U_2})^{3'}$		23.83
$(V_{O_2}V_{U_2})^{4'}$	21.91	24.26
$(V_{O}V_{U_2})^{2\circ}$		22.43
$(V_{O}V_{U_2})^{\circ}$		22.14
$(V_{O}V_{U_2})^{x}$		22.01
$(V_{O}V_{U_2})^{'}$		21.99
$(V_{O}V_{U_2})^{2'}$	19.88	21.92
$(V_{O}V_{U_2})^{3'}$	20.05	22.19
$(V_{O}V_{U_2})^{4'}$		22.66
$(V_{O}V_{U_2})^{5'}$	20.91	23.23
$(V_{O}V_{U_2})^{6'}$	21.63	23.96
$V_{U_2}^{2\circ}$		21.18
$V_{U_2}^{\circ}$		21.05
$V_{U_2}^{x}$		21.01
$V_{U_2}^{'}$		20.95
$V_{U_2}^{2'}$		20.99
$V_{U_2}^{3'}$		21.12
$V_{U_2}^{4'}$	19.35	21.38
$V_{U_2}^{5'}$		22.05
$V_{U_2}^{6'}$	20.40	22.49
$V_{U_2}^{7'}$	21.11	23.32
$V_{U_2}^{8'}$	22.14	24.33

(a)

Defect	Vathonne 14	Vathonne 17
$(V_{O_2}V_{U})^{2\circ}$		14.61
$(V_{O_2}V_{U})^{\circ}$		14.41
$(V_{O_2}V_{U})^{x}$		14.29
$(V_{O_2}V_{U})^{'}$		15.50
$(V_{O_2}V_{U})^{2'}$		17.09
$(V_{O}V_{U})^{2\circ}$		12.75
$(V_{O}V_{U})^{\circ}$	11.37	12.36
$(V_{O}V_{U})^{x}$		12.70
$(V_{O}V_{U})^{'}$		12.86
$(V_{O}V_{U})^{2'}$	11.26	12.54
$(V_{O}V_{U})^{4'}$	14.11	
$V_{U}^{2\circ}$		11.91
V_{U}°		11.34
V_{U}^{x}		10.96
$V_{U}^{'}$	10.10	11.29
$V_{U}^{2'}$		11.12
$V_{U}^{3'}$	10.18	11.41
$V_{U}^{4'}$	10.65	11.52
$V_{O}^{2\circ}$	2.60	2.55
V_{O}°		3.97
V_{O}^{x}		5.45
$V_{O}^{'}$		7.02
$V_{O}^{2'}$	7.85	8.29
h°	0.00	0.00
$e^{'}$	1.71	2.04
$O_{i}^{2\circ}$		0.03
O_{i}°		-0.13
O_{i}^{x}		0.03
$O_{i}^{'}$	-0.09	-0.07
$O_{i}^{2'}$	0.09	0.21
$O_{i_2}^{2\circ}$		0.53
$O_{i_2}^{\circ}$	0.75	0.41
$O_{i_2}^{x}$		0.61
$O_{i_2}^{'}$		0.40
$O_{i_2}^{2'}$	0.60	0.42
$O_{i_2}^{3'}$		0.72
$O_{i_2}^{4'}$	1.11	1.09
$U_{i}^{4\circ}$	0.51	-0.35
$U_{i}^{3\circ}$	1.39	0.71
$U_{i}^{2\circ}$	2.59	2.14
U_{i}°		4.01
U_{i}^{x}		6.08
$U_{i}^{'}$	7.22	6.96
$U_{i}^{2'}$	8.92	8.84

(b)

Table 7: Complete thermodynamic datasets for Vathonne's 14 and 17 models [53, 52]
Reference $g_h = 0$, the Bound Schottky defect is BSD2 of the original articles, in which the O vacancies lie in the 110 direction.

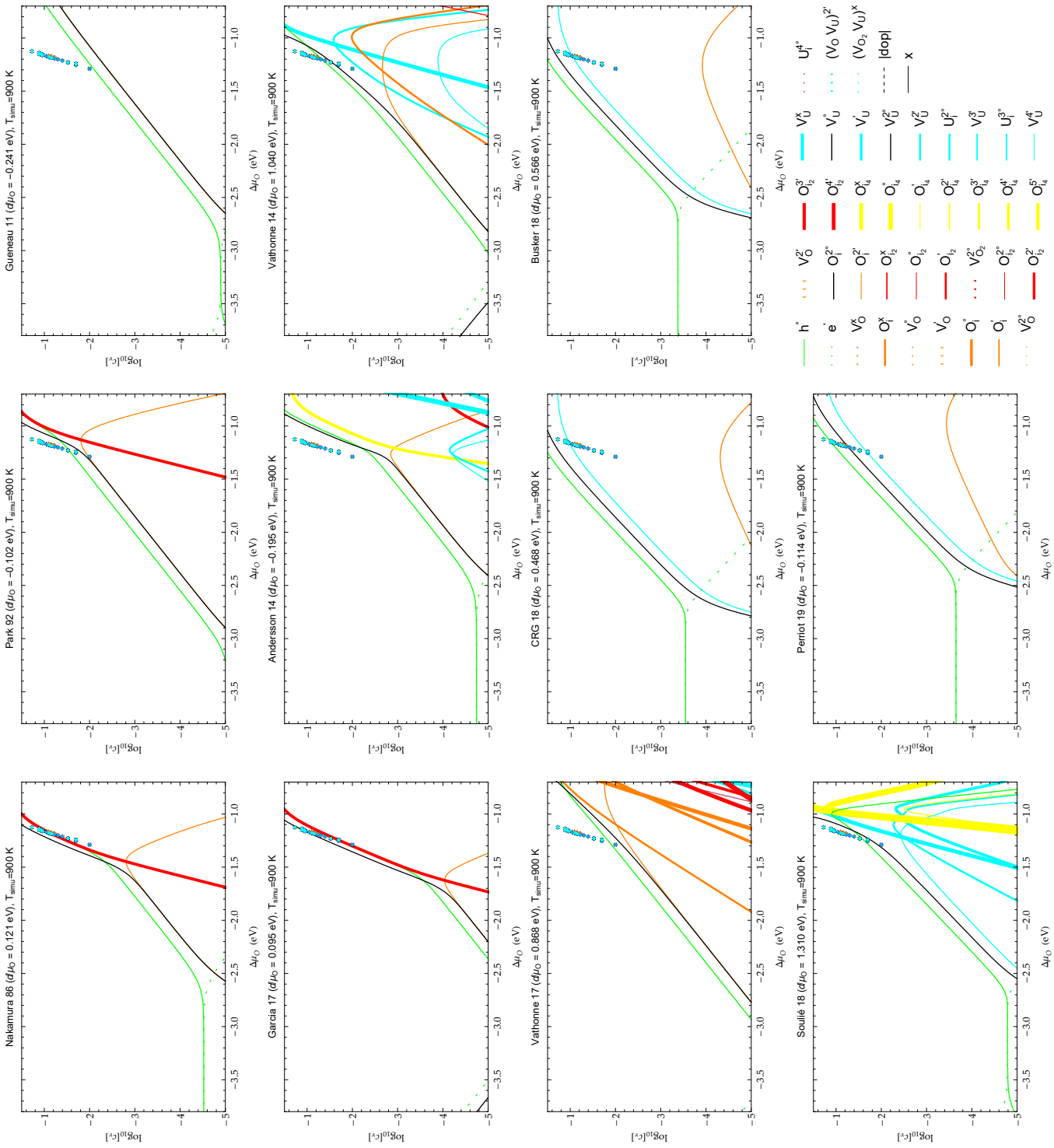

Figure 15: Comparison of the models: Defect concentrations as functions of the oxygen chemical potential at 900 K for the shifted models

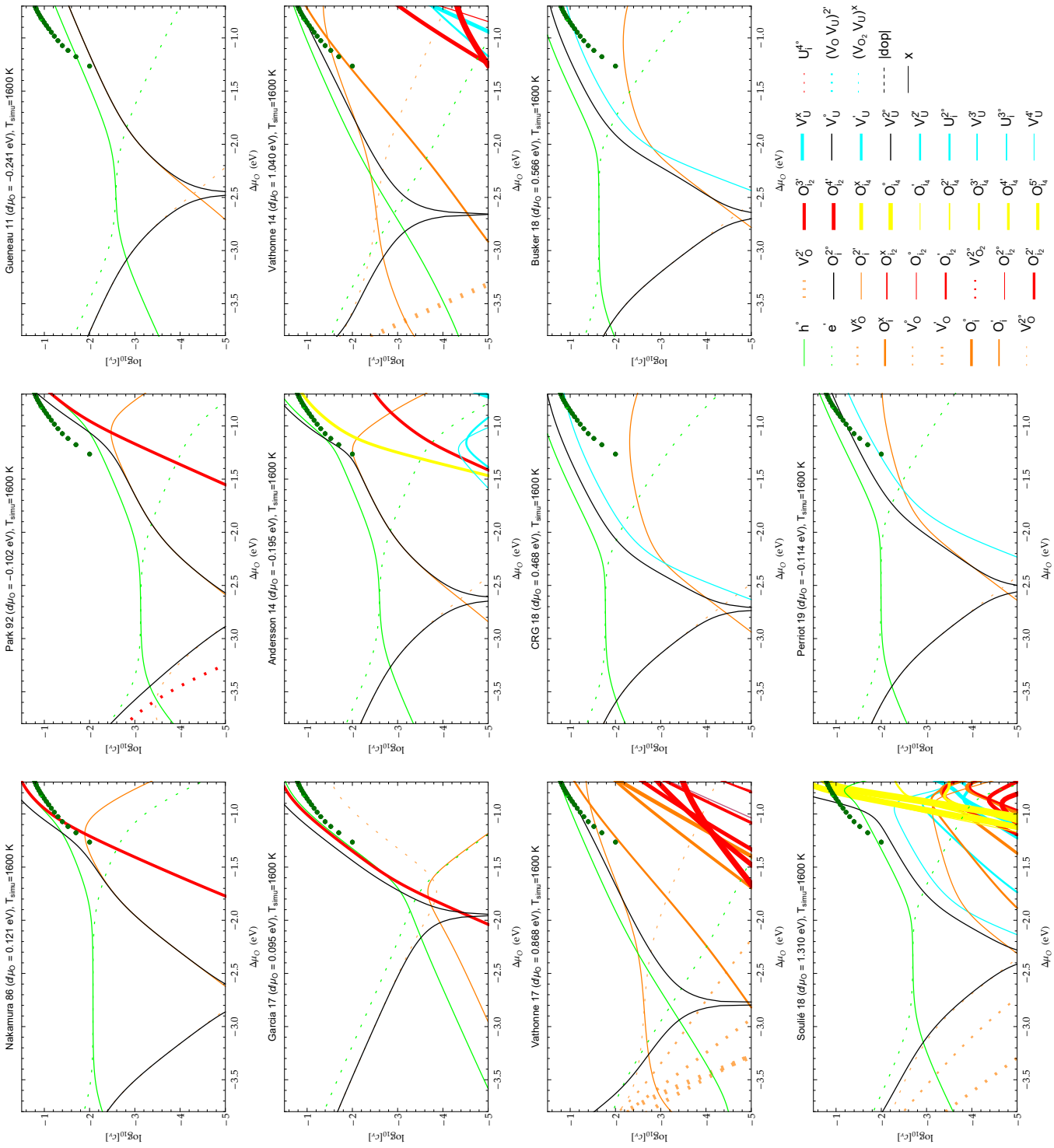

Figure 16: Comparison of the models: Defect concentrations as functions of the oxygen chemical potential at 1600 K for the shifted models

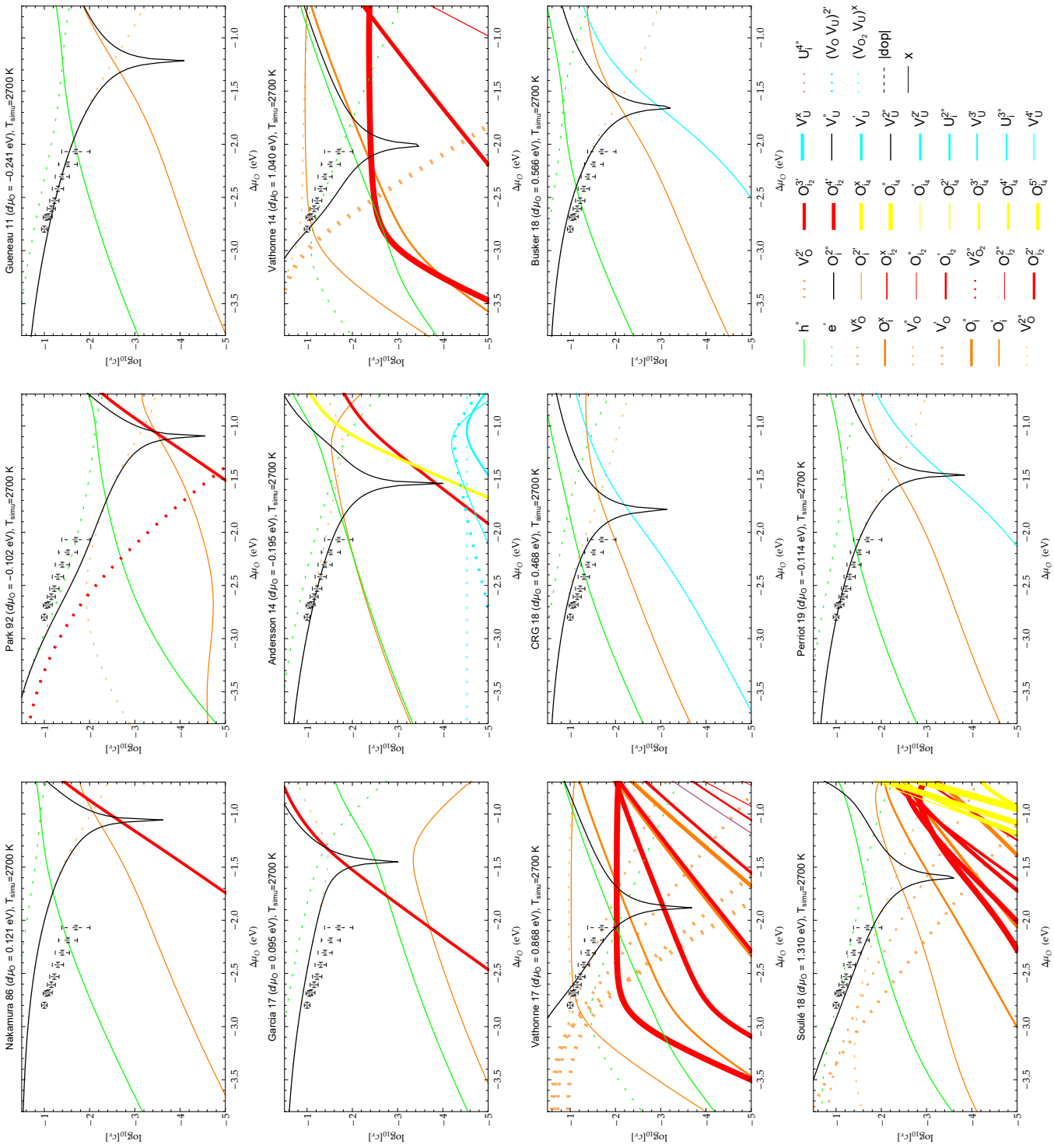

Figure 17: Comparison of the models: Defect concentrations as functions of the oxygen chemical potential at 2700 K for the shifted models

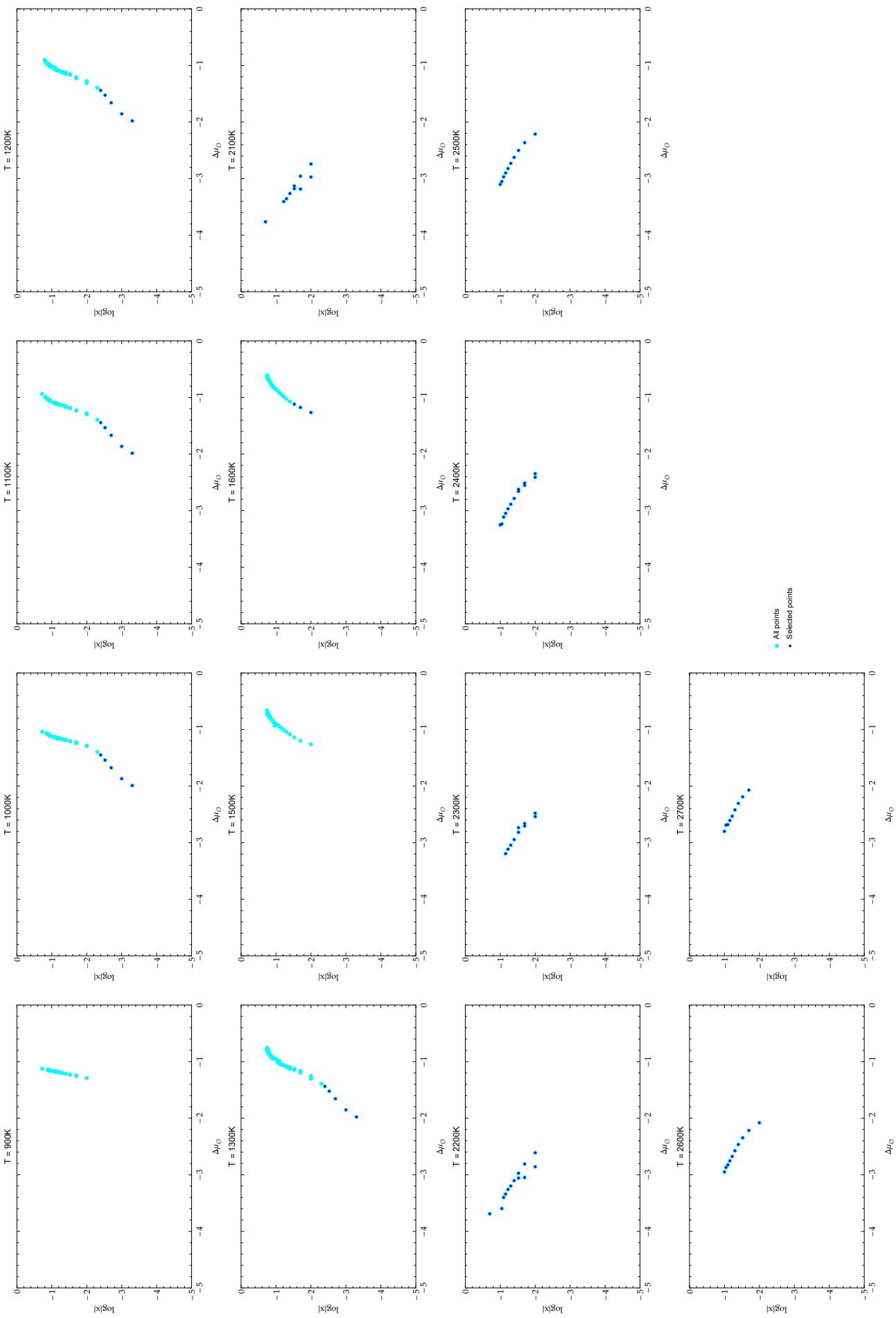

Figure 18: Selection of the experimental data used for fitting the models devoid of oxygen interstitial clusters $O_{i_{n,n\geq 2}}$
The dark blue points are selected for these models while the light blue ones stand for the models having oxygen interstitial clusters